

**MEASUREMENT AND ANALYSIS OF STRUCTURE AND  
FUNCTION OF MYOCARDIUM IN EMBRYONIC AND  
ADULT HEART**

Thesis by

Abbas Nasiraei Moghaddam

In Partial Fulfillment of the Requirements

for the Degree of

Doctor of Philosophy

California Institute of Technology

Pasadena, California

2007

(Defended September 28, 2006)

© 2007

Abbas Nasiraei Moghaddam

All rights Reserved

**IN HIS NAME, THE BENEFICENT, THE MERCIFUL.**  
**ALL PRAISE IS DUE TO HIM, THE LORD OF THE WORLDS.**  
MAY THE PEACE AND BLESSINGS OF HIM BE UPON HIS BEST  
SERVANTS EVER, MUHAMMAD AND HIS FAMILY.

To  
My Parents  
My wife, Mahya  
and  
My son, Mohammad Hossein.

## Acknowledgements

***My Lord! Grant me that I should be grateful for Thy favor which Thou hast bestowed on me and on my parents, and that I should do good such as Thou art pleased with, and make me enter, by Thy mercy, into Thy righteous servants. --Al-Naml 27:19***

Thanks to all who inspired me the passion for learning and provided support and encouragement for me in the way of knowledge. Thanks to all of my teachers and mentors, especially my parents, Monir Pahlavan and Asadollah Nasiraei Moghaddam.

I would like to express my gratitude to my advisor, Prof. Morteza Gharib, for his great support throughout the years I spent at Caltech. His visions and smart approaches have always inspired me to aim the highest objectives in the science world.

I also would like to acknowledge Prof Amir Amini, Dr. Han Wen, Prof Scott Fraser, Dr. Michael Tyszka, Prof Hamid Soltanian Zadeh, Prof Changhuei Yang and Prof Alan Barr for their supports and advice in the course of my study and research at Caltech.

Among many others who helped me towards Doctor of Philosophy degree I would like to thank all past and current members of Gharib research group especially Jashua Adams, Dr. Arian Forouhar, Anya Grosberg, Dr. David Jeon, Dr. Farid Khorrani, Elizabeth Lester, Dr. Nikoo Saber and Martha Salcedo. I also appreciate the helps and supports of all faculty, staff and colleagues at Caltech in general and Bioengineering option, GALCIT, Biological Imaging Center and International Student Program in particular.

I appreciate the support of all of my dear friends who helped me, and my family to overcome the difficulties of living far from our loved home country, IRAN. I wish them all a prosperous and meaningful life full of happiness.

And last but by no means the least, my exceptional thank to Mahya and Mohammad Hossein for always being with me in this challenging period of life.

## Abstract

Congestive Heart Failure is the most common and costly medical problem in the modern world. Current disease management procedures are mostly limited to treating the symptoms of this disease. The effective treatment, however, needs a deep understanding of the normal structure-function relationships of the myocardium.

The research of this study is concerned with the relationship between the structure and function of the myocardium in both embryonic and adult hearts. This relationship was investigated through an in-depth analysis of the spatial distribution of the local contractile function in the myocardium. The analysis is based on the heart kinematics captured through the tissue tracking of the myocardium.

Advanced imaging techniques, such as DENSE MRI and confocal microscopy, were used for tissue tracking in adult and embryonic myocardium, respectively. The acquired data, together with continuum mechanics concepts and computational methods, were exploited in a Lagrangian framework to measure appropriate characteristic parameters that describe local contribution of the myocardium in its global functionality.

This method resulted in novel understandings of the local and global functions in each of these hearts. In particular, it was observed in the adult heart that the left ventricle functionality is not uniformly distributed. Instead, the regions with higher effect on the pumping process form a helical band which wraps around the heart. This is the first time that such a myocardium macro-structure, which is supported by the established histological evidence, is revealed from its function in a beating heart. It can be considered as a landmark in connecting the structure and function of the heart through imaging. Furthermore, the compatibility of this model with microscopic observations about the fiber direction is investigated.

A similar approach was applied to embryonic zebrafish heart with GFP labeled myocytes. It identified distribution of regions that play an active role in functionality of the heart tube. This new understanding has provided better insights into the pumping mechanism of the embryonic heart.

**ACKNOWLEDGEMENT****MEMO****ABSTRACT****CHAPTER ONE: PROLOGUE**

- 1.1 Introduction
- 1.2 Goals
- 1.3 Organization
- 1.4 References

**CHAPTER TWO: APPLICATION OF LAGRANGIAN APPROACH TO INVESTIGATE THE ACTIVE AND PASSIVE REGIONS IN THE EMBRYONIC ZEBRAFISH HEART**

- 2.0 Chapter Abstract
- 2.1 Introduction
- 2.2 Methods
  - 2.2.1 Data Acquisition
  - 2.2.2 Methodology
  - 2.2.3 Mathematical Methods
    - a) Lagrangian semi-cylindrical framework
    - b) Directions
    - c) Spatio-Temporal smoothing
    - d) Strain and Torsion calculation
    - e) Principal curvature estimation
    - f) Wave Propagation Investigation
- 2.3 Results
  - 2.3.1 Calculation of the directions
  - 2.3.2 Slice Displacement
  - 2.3.3 Other parameters: Strain, Torsion, Curvature, and VSF

- 2.4 Discussion of results
  - Limitation of the study
- 2.5 Chapter Conclusion
- 2.6 Chapter References

## **CHAPTER THREE: METHODS TO MEASURE 3-D SYSTOLIC AND DIASTOLIC STRAIN PATTERNS IN THE LEFT VENTRICLE FROM DENSE MRI**

- 3.0 Chapter Abstract
- 3.1 Introduction
- 3.2 Methods
  - 3.2.1 DENSE MRI Data Acquisition
  - 3.2.2 DENSE Data Post-Processing
  - 3.2.3 Deformation Gradient Tensor
  - 3.2.4 Displacement smoothing
  - 3.2.5 Estimation of Deformation Gradient Tensor
  - 3.2.6 Anti-deformation gradient matrix  $G$ 
    - a) Estimation of  $F_{33}$
    - b) Estimation of  $F_{13}$  and  $F_{23}$
  - 3.2.7 Error Analysis
  - 3.2.8 E33 Correction
  - 3.2.9 Filtering of Strain
  - 3.2.10 RCL strains
- 3.3 Results
  - Comparative study
- 3.4 Discussion
- 3.5 Chapter Conclusion
- 3.6 Chapter References

## **CHAPTER FOUR: MACRO-STRUCTURE OF THE LEFT VENTRICLE**

- 4.0 Chapter Abstract
- 4.1 Introduction
- 4.2 Wall thickening
- 4.3 Importance of WT & SI
- 4.4 Experimental methods
- 4.5 Results
- 4.6 Discussion
- 4.7 Chapter Conclusion
- 4.8 Chapter References

## **CHAPTER FIVE: CONCLUSION**

- 5.1 Primary Contributions
- 5.2 Future works
- 5.3 Chapter References

## **APPENDIX**

### **A. The Embryonic Vertebrate Heart Tube Is a Dynamic Suction Pump**

Published in *Science*, 312 751-753 (5 May 2005)

### **B. Timing and strength of activities in the embryonic heart**

#### **C. 1) 3-D Measurement of Cardiac Deformation from DENSE MRI Data**

#### **C. 2) Combination of Short Axis and Long Axis Data**

## CHAPTER 1

### Prologue

#### 1.1 Introduction

Heart failure is the most common and costly medical problem in the modern world (Thom, Haase et al. 2006). Current disease management procedures are capable of prolonging life by treating the symptoms of this disease rather than derangement of the normal structure-function relationships responsible for symptoms and mortality (Rich 1997). Our limited knowledge of the heart's function from micro to macro continues to be an obstacle in designing strategies for effective treatment of heart failure (Buckberg, Weisfeldt et al. 2004). Since the heart is a biomechanical pump, its functionality depends on its structure and ability to deform. It is imperative, therefore, for any treatment of congestive heart failure (CHF) to appreciate and understand "normal" structure and associated functions of the myocardium.

In general, the abnormalities in myocardium structure relate to the ventricle shape, muscle fiber orientation, and excitation-contraction coupling. Understanding of heart's structure and function, therefore, is an important area of research and is approached in various ways by many leading investigators. Using the microstructure of the myocardium based on the fiber orientation is a difficult and computationally expensive approach to study the heart function (Hsu, Muzikant et al. 1998; Guccione, Moonly et al. 2001; Quarterman, Moonly et al. 2002). The alternative approach is to define a macro-structure for the heart which is much simpler and may be modeled with a few parameters. The macro-structure idea may be sought through an unconventional theory about heart's

structure, i.e., the “muscle-band concept,” which was proposed about 40 years ago by Torrent-Guasp (1966) (fig. 1.1). This novel approach has potential for opening a new avenue in heart modeling and treatment based on macroscopic movement of the tissue (Corno, Kocica et al. 2006) in contrast to the conventional microscopic models. Torrent-Guasp concept, however, has only been tested and somewhat verified through histological studies. To the best of our knowledge the existence of the muscle band has not been verified through its functional role.

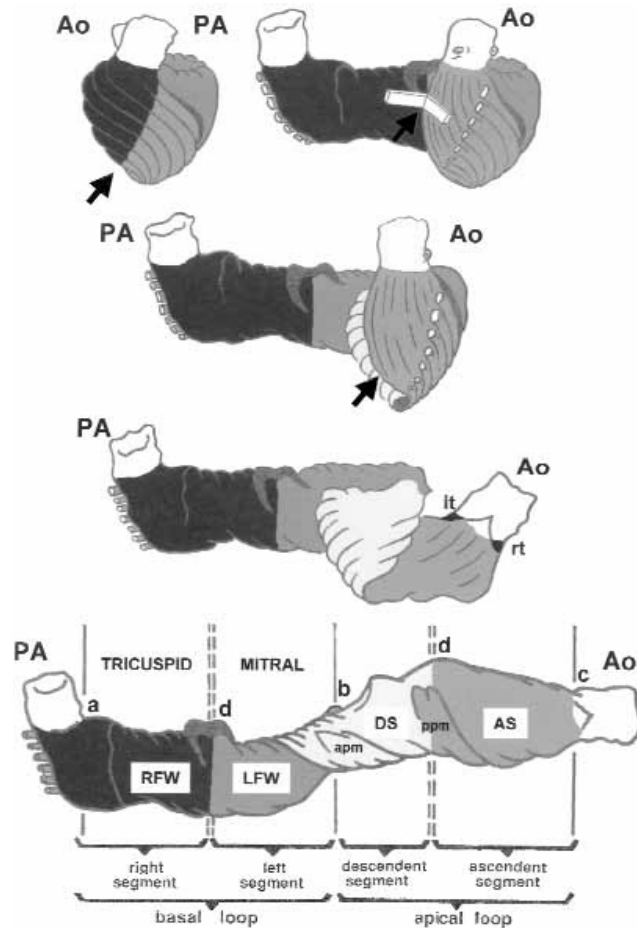


**Figure 2.1 schematic representation of the ventricular myocardial band by Torrent-Guasp. Fiber directions (microscopic structure) are not necessarily parallel to the muscle band (macroscopic form). published in *The Journal of Thoracic and Cardiovascular Surgery*, Volume 122, Francisco Torrent-Guasp et al., p 389-392, Copyright Elsevier (2001). (with written permission)**

A good approach for studying the myocardium structure and function is to investigate them during the heart development. Since the heart’s function starts in its early stages of development and never stops throughout the course of cardiogenesis, its structure-function relation can be tracked during its embryonic development. This approach is especially useful in investigations of congenital heart diseases. Both embryonic and

grown hearts are bio-mechanical pumps that operate through their myocardial deformation. Hence study of their functionality needs the deformation analysis.

The volume changes of the left ventricle, associated with the cardiac output, have long been known to be complex (Parmley and Talbot, 1979) and it is also known that there are significant local variations in the time course, magnitude, and pattern of deformations within the myocardial wall (Humphrey 2002). Also, in the embryonic heart, underlying mechanisms of the pumping and its morphogenesis are caused by the deformation of the heart wall (Nakamura, Kulikowski et al. 1980). Deformation of the continuum is usually analyzed by tissue tracking methods in which a group of material points are tracked in a reference frame. This framework, as well as acquired data, is commonly referred to as the Lagrangian.

Noninvasive tracking of the myocardial points is uniquely performed by advanced MRI techniques in an adult heart (Isbell and Kramer 2005). Among the different MRI techniques used to estimate motion, tagging (TMRI) and displacement encoding with stimulated echoes (DENSE) are known for particle tracking in cardiac MR imaging (Aletras, Ding et al. 1999; Ozturk, Derbyshire et al. 2003). In comparison to tagging, DENSE provides better resolution, works in a full three-dimensional Lagrangian coordinate system, and covers a larger segment of the cardiac cycle (see chapter 3). In examining the embryonic heart, the confocal microscopy images of the GFP-labeled myocytes, with their high spatio-temporal resolution, greatly facilitated the study of wall contraction and motion by tracking the myocytes on the myocardium.

These novel imaging techniques provide more accurate measurements of the

deformation. New effective computational methods are needed, however, to show the full potential of these techniques and compensate for their limitations.

## 1.2 Goals

This thesis is a compilation of experimental and computational methods in medical imaging, image processing, and bio-mechanics analysis which have been blended into a coherent research theme. The major goal of this research is to understand the relationship between structure and function of myocardium through analysis of heart muscle kinematics in both embryonic and adult hearts. In particular for the adult heart, we intend to investigate the bandlike macro-structure model of the myocardium (Fig. 1.1) through DENSE MRI. Furthermore, we use DENSE MRI data to determine patterns of true myocardial strain and Lagrangian motion, leading to a better understanding of the ventricle's mechanics and function.

For the embryonic heart, the goal is to determine the regions in the myocardium that induce deformation in the heart tube at its prelooping stages. Using the spatial distribution of these active regions, we investigate the mechanism of pumping at that period. We also investigate the possible similarities between the pumping mechanisms of the embryonic and adult hearts. They may help in the treatment of the congenital heart diseases. Moreover, these similarities and the aforementioned distribution may eventually result in clues about the formation of the muscle-band structure in the adult heart.

Intermediate goals of this interdisciplinary research are in fields of medical imaging, image processing, and biomechanics. They include

- (1) improvement and optimization of cardiac DENSE MRI protocols on 3T machine,
- (2) showing the potential of the four-dimensional confocal microscopy in providing, detailed information about the heart tube geometry and kinematics
- (3) expanding the methods of measurement and computation of the heart strain,
- (4) development and application of computational mechanics methods that are used in image-based modeling.

### **1.3 Organization**

The organization of the thesis is meant to reflect the interdisciplinary nature of this research and avoid the possible confusion of these disciplines. The following three chapters are independent manuscripts to peer-reviewed journals. Each one investigates the myocardial structure & function from a different point of view by addressing some of the issues introduced in the introduction (§1.1). The thesis author is the lead author of all three articles and wrote all or the large majority of them.

Chapter 2 presents an innovative kinematics-based approach to investigate the structure and function of the embryonic heart based on the spatial distribution of its active regions. The approach is based on a Lagrangian semi-cylindrical coordinate system and accompanying computational methods. These methods are applied to images of fluorescently labeled myocyte cells in zebrafish heart obtained by 4D confocal laser scanning microscopy at two developmental stages. In addition to information about the heart tube geometry and kinematics, this chapter also provides better insights to the pumping mechanism of the embryonic heart.

Chapter 3 provides a framework for the detailed analysis of cardiac deformation and contraction. Following a full introduction about the MR strain imaging, it demonstrates new methods that are able to calculate 3D systolic and diastolic strain patterns in the left ventricle with high spatio-temporal resolution from a single-slice DENSE MRI dataset. Furthermore this chapter gives a short review of the required solid mechanics concepts as well as the experimental part of this research, including details of DENSE cardiac MRI and its post processing. Also, in chapter 3 we show the feasibility of obtaining high spatio-temporal resolution for tissue tracking by DENSE MRI from human subjects.

In contrast to chapter 3, chapter 4 focuses on the relation of the myocardial structure and function rather than the computational methods. Through a logical approach, this chapter shows how the macro-structure of the LV may be derived from DENSE MRI images. It also discusses the compatibility of the macro-structure with micro-structural organization of the fibers in the LV.

In chapter 5, we summarize the primary contributions of this research and discuss future works.

The secondary works and byproducts of our research are added as appendices. Appendix A is our published paper in *Science* magazine in which the author of the thesis is a coauthor. Some other valuable results of this research which are not presented in main articles of the thesis are also added in appendices B and C.

## 1.4 References

- Aletras, A. H., S. Ding, et al. (1999). "DENSE: displacement encoding with stimulated echoes in cardiac functional MRI." J Magn Reson **137**(1): 247-52.
- Buckberg, G. D., M. L. Weisfeldt, et al. (2004). "Left ventricular form and function: scientific priorities and strategic planning for development of new views of disease." Circulation **110**(14): e333-6.
- Corno, A. F., M. J. Kocica, et al. (2006). "The helical ventricular myocardial band of Torrent-Guasp: potential implications in congenital heart defects." Eur J Cardiothorac Surg **29 Suppl 1**: S61-8.
- Guccione, J. M., S. M. Moonly, et al. (2001). "Mechanism underlying mechanical dysfunction in the border zone of left ventricular aneurysm: a finite element model study." Ann Thorac Surg **71**(2): 654-62.
- Hsu, E. W., A. L. Muzikant, et al. (1998). "Magnetic resonance myocardial fiber-orientation mapping with direct histological correlation." Am J Physiol **274**(5 Pt 2): H1627-34.
- Humphrey, J. D. (2002). Cardiovascular solid mechanics : cells, tissues, and organs. New York, Springer.
- Isbell, D. C. and C. M. Kramer (2005). "Cardiovascular magnetic resonance: structure, function, perfusion, and viability." J Nucl Cardiol **12**(3): 324-36.
- Ozturk, C., J. A. Derbyshire, et al. (2003). "Estimating Motion From MRI Data." Proc. Of the IEEE **91**(10): 1627-1648.
- Quarterman, R. L., S. Moonly, et al. (2002). "A finite element model of left ventricular cellular transplantation in dilated cardiomyopathy." Asaio J **48**(5): 508-13.
- Rich, M. W. (1997). "Epidemiology, pathophysiology, and etiology of congestive heart failure in older adults." J Am Geriatr Soc **45**(8): 968-74.
- Thom, T., N. Haase, et al. (2006). "Heart disease and stroke statistics--2006 update: a report from the American Heart Association Statistics Committee and Stroke Statistics Subcommittee." Circulation **113**(6): e85-151.
- Torrent Guasp, F. (1966). "[On cardiac morphology and functionalism. I.]" Rev Esp Cardiol **19**(1): 48-55.

**CHAPTER 2****Application of Lagrangian Approach to Investigate the Active and Passive Regions in the Embryonic Zebrafish Heart****2.0 Chapter Abstract**

Tracking the myocardial trajectories during contractions of the embryonic heart tube (HT) provides information about the morphology and biomechanics of the developing vertebrate heart. Here, the biomechanics of a zebrafish heart tube is analyzed by visualizing myocytes that are GFP labeled to show that the function of the heart tube is not uniformly distributed along the tube. The novel approach and methods that we have developed reveal regions of the heart tube that play an active role in its functionality (active sites). Starting from dynamic three-dimensional volumes acquired using a fast confocal microscope, we determined the positions of the sparsely distributed myocytes. Next, we developed computational methods involving a Lagrangian semi-cylindrical coordinate system to extract quantitative characteristics of the heart tube contraction, including the longitudinal, radial, and circumferential myocytes displacements, as well as heart tube curvature, local volumetric squeeze fraction (VSF), and time-resolved axial strain and torsion. Analysis of these factors identifies the mechanically active and passive regions along the contractile tube, shedding light on embryonic heart function. The proposed methods are effective, even in cases where positional data are available only for part of the heart tube's circumference, which is crucial in our study, since imaging accuracy decreases with depth, due to light scattering. To show the applicability of this

approach, we analyzed 26 and 34 hours post fertilization (hpf) fish, which show similar active regions (near the in-flow tract) and passive regions.

## **2.1 Introduction**

Heart failure is the most common and costly medical problem in the modern world (American Heart Association 2006). Studying the embryonic heart can help increase our limited knowledge about the form-function relationships in the adult heart and enhance our ability to design strategies for effective treatments of heart failure (Buckberg et al. 2004; Berne and Sperelakis 1979), especially in the context of congenital heart diseases. Since the embryonic heart is already functional while it develops from a simple to a more complicated structure throughout the course of cardiogenesis, study of structure-function relation is possible in a variety of conformations.

Even in the earliest stages of development, when the embryonic heart is a simple tube, the structure and function of the embryonic heart are not yet well understood. The action of the heart tube (HT) as a unidirectional pump has been taken to indicate that it is a peristaltic pump (Vogel 1994, Fishman and Chien 1997, Gilbert 2000). Careful quantitative measurements of the blood flow, however, show that HT behavior does not match a peristaltic mode of pumping, and rather resembles a resonant pumping mechanism distinct from peristalsis (Forouhar et al. 2006), notably because of the non-linear relationship between the flow rate and the beating frequency (Hickerson et al. 2005).

While it is clear that mechanical forces influence heart morphogenesis (Nakamura et al. 1980, Taber 1995, Hove, Koster, et al. 2003), the exact mechanics that shape the process

remains largely unknown (Nerurkar, Ramasubramanian et al. 2006). Regardless of the underlying mechanisms of the pumping or morphogenesis of the embryonic heart, these phenomena are caused by the deformation of the tube wall which is a consequence of the myofiber contractions. The key, therefore, to understanding the functionality of the embryonic heart as well as its topological changes during different stages, is to analyze the deformation of the heart tube.

The morphogenesis of the vertebrate embryonic heart has been studied using the strain calculation, mainly in post looping stages (Taber 1994, Tobita 2000a, Tobita 2000b). Access to the embryonic heart, particularly in early stages of development, poses additional complications (Alford 2003). Only minimal experimental data have been published on the strain and stress at the time of looping (Alford 2003, Zamir 2004), where the method of strain calculation is based on two-dimensional images of microbeads which are located around the looping area of an embryonic chicken heart. In each region, these authors track three beads, located 50 to 100  $\mu\text{m}$  apart, while the diameter of the heart tube is approximately 300  $\mu\text{m}$ . They assume that the strain is almost uniform inside the triangle determined by those three beads. They invasively calculated the longitudinal and circumferential strains with a high temporal resolution of 33 ms, but the spatial resolution is poor such that in each time interval, only one number represents the strain of the entire length of the tube at each of the three regions across the tube.

Confocal microscopy images of the green fluorescent protein (GFP)-expressing myocytes, with their high spatio-temporal resolution, enable us to study wall contraction and motion by tracking the myocytes, instead of microbeads, on the myocardium

(Forouhar et al. 2006). This approach has both a high spatial and temporal resolution and is noninvasive. Dynamic three-dimensional volumes can be reconstructed (Liebling et al. 2005) and motion of the myocytes analyzed in three-dimensional space, rather than two-dimensional, as performed in previous studies. We used an animal model (zebrafish) for microscopy whose embryonic heart is optically accessible (Forouhar et al. 2006). We may get clear images, therefore, of the myocytes from the portion of the HT wall that is located close to the body surface of the embryo.

The effective depth at which we may get these clear images is limited by light scattering. The acquired data, therefore, only consist of a sparse arrangement of the material points mainly from a small portion of the heart tube wall, but this method is still superior to other data-collection techniques used for HT deformation study. The collected images of myocytes could then be used to calculate accurate in-plane strain maps on the tube wall, using methods similar to the one proposed by Hashima et al. (1993). The current investigation, however, is concerned with the spatial distribution of the myocardium function along the HT, rather than the calculation of strain map.

We propose that the function of the embryonic heart in pumping the blood is non-uniformly distributed along the HT, and is focused in specific locations. These locations store energy in the heart structure by generating a deformation in the tube. This energy is then released to pump the blood when the deformed body relaxes. In this paradigm, functionality is translated to generating the deformation, and *active site* is defined as a location that initiates a deformation in its neighborhood of the heart tube. A more specific definition of active sites is given in the methodology section.

In this study, we propose some simple, but novel, approaches that help to investigate the activity or passiveness of regions along the heart tube regions, based solely on the kinematics of the myocytes. We also develop the computational tools to extract the required quantitative kinematical information from the acquired images. A Lagrangian semi-cylindrical coordinate system is defined along the main axis of the tube. The time-resolved longitudinal, radial, and circumferential displacements of the myocytes can then be estimated in this coordinate system, using the developed computational tools. These tools also help us estimate the kinematical quantities like torsion, curvature, and volumetric squeeze fraction (VSF) that are needed in our approach

It should be noted that the calculations performed in this study are only aimed to determine the active sites. For example, we do not intend to calculate surface longitudinal and circumferential strain maps, since the time-resolved, one-dimensional longitudinal strain is enough for the scope of this study. Analytical methods on the wave propagation, strain, and torsion, which provide quantitative evidences for speculations about the structure of the embryonic heart, are implemented and applied at the two developmental stages of 26 and 34 hours post fertilization (hpf). The onset of zebrafish circulation is at 24 hpf (Jin 2005) and at 26 hpf it is an almost straight tube. Looping starts around 30 hpf and peaks around 34 hpf (Trinh and Stainier, 2004).

The validity of the methods is shown by comparing the outcomes of different activity indications. The compatibility of the results for these two developmental stages also indicates the accuracy and robustness of the developed methods.

## 2.2 Methods

### 2.2.1 Data Acquisition

The zebrafish (*Danio rerio*) is a popular model for cardiogenetic studies because its transparent embryos provide optical access to the earliest stages of heart development. We used a transgenic Tg (*cmlc2:GFP*) fish with fluorescently labeled myocardial cells to study the early heart tube dynamics (Huang et al. 2003). A Zeiss LSM 5 LIVE high-speed confocal microscope was used to take optical sections at 3  $\mu\text{m}$  intervals and 151 frames per second. Enough images to record multiple periods of the cardiac cycle were acquired. Imaging was performed on 26 and 34 hours post fertilization (hpf) embryos, when the heart is still a valveless tube. These sections (about 40) were synchronized using a wavelet-based registration algorithm to give 4D (3D plus time) data (Liebling et al. 2005). These data were imported into Imaris Bitplane to collect automated three-dimensional position information for the cells (Fig. 2.1). Myocytes appear as white spots and we record the position of each spot's center of mass over time. We used 120 of these collected time frames, which comprise two periods of the cardiac cycle.

### 2.2.2 Methodology

An *active* element may primarily be defined as an element that causes (*initiates*) a deformation in itself from its position at rest. It generates an internal force to deform the body. If this element is isolated, it does a positive work during the deformation on itself, which is, of course, stored in the deformed body because of its elasticity. In contrast, a *passive* element does not initiate any force or deformation. It only reacts to the deformation because of its elastic resistance against the deformation. The reaction force

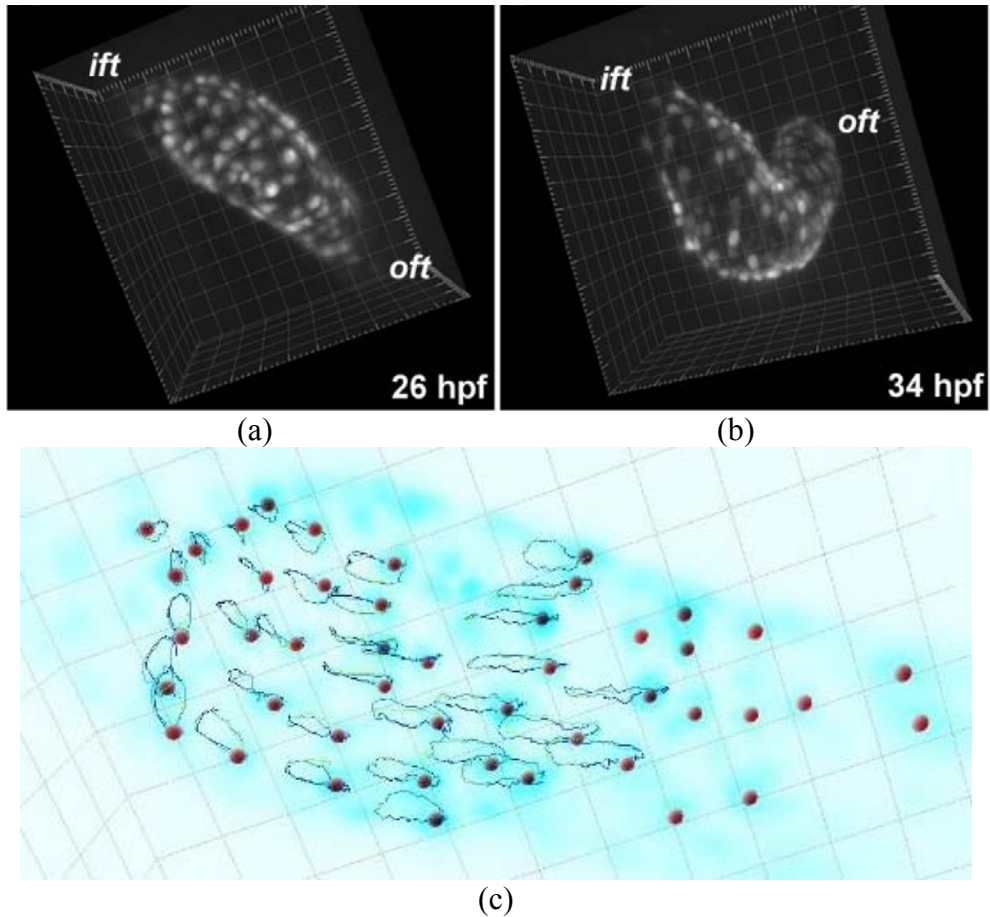


**Figure 2.1** Three-dimensional reconstruction of a transgenic Tg (*cmc2:GFP*) embryonic zebrafish heart at (a) 26 hpf and (b) 34 hpf. The myocardial cells are fluorescent and have been marked with spheres. The reconstruction was obtained by acquiring 40 optical sections (3  $\mu\text{m}$  intervals) at high speed (151 fps) with a confocal microscope (Zeiss LSM 5 LIVE). These sections were synchronized using a wavelet-based registration algorithm. The trajectories of myocytes are indicated at 26 hpf in (c).

only does negative work on its surrounding environment as the deformation increases. A passive region in this sense will not deform, if it is left isolated.

Here, we consider different definitions for active and passive elements. We consider the effect of the element on its surrounding body to determine the activity. We define an *active* element as an element that performs a positive work on the rest of the body for some times between rest and maximum deformation of its neighborhood. An element that is active according to the primary definition, therefore, maybe considered passive in

this new definition. That is, its contractility is dominated by other active regions such that it does negative work on the body during the deformation. This is a dominated contraction which does not energize the pumping process. For example, contraction of a non uniform muscle fiber, which is fixed at both sides, causes some parts of it to become shorter, while other parts stretch. According to the terminology of this study, stretched parts are considered passive, since they do negative work on the rest of the body, although they generate a contracting force. In fact, there are some studies that show contractility can be observed in all regions of the HT myocardium when they are isolated from the rest of the body (Romanoff 1960). This observation does not contradict finding passive regions in the myocardium, according to our proposed definitions.

With these definitions, when a region of the heart tube is determined as an active part, it means that at least for a period of time, it takes part in generating a deformation by doing a positive work on the rest of the tube body, as it is being deformed. Part of this energy is spent driving the fluid in the tube (pump the blood) when it is released. The active regions are investigated here through the kinematics of the heart tube in simple ways suggested and discussed below. It should be noted that these indications of activity are *sufficient conditions* for the defined activity, and not necessarily present in all active regions. These indications are extendable to be used in more complex geometries of the following stages.

### **First indication: Shortening versus displacement**

By averaging the displacement of the points on the tube wall over the axial slices, which are perpendicular to the main axis of the tube, we may reduce the problem to semi-1D (as

discussed in §2.2.3(a). The focus here is on the longitudinal displacement and the HT is treated as an elastic straight rod which is fixed at both ends and its regions move longitudinally because of their own contractions. Positions with shortening (negative strain) would be easily determined as the active sites, if all contractions happened simultaneously. Different timings, however, cause a wave propagation behavior that prevents such a simple solution.

As we are dealing with contractile elements, they may not do any positive work when they are lengthening. On the other hand, not all shortenings are performed actively. It is quite possible that reflection of a displacement wave, or sudden relaxation of an active region, compresses an element which is passively following other points. Hence, we only consider the shortenings that happen during the increase of the deformation at the same region, i.e., when it is getting far from its position at rest. In the early stages of the embryonic heart, the major deformation is a simple longitudinal displacement towards the in-flow. Each section, therefore, whose major shortening happens prior to, or very close to, its major longitudinal displacement, should be an active element.

### **Second indication: Squeeze**

This indication is more accurate than previous ones, as it takes both longitudinal and radial displacements of the wall into account. Squeeze is a simultaneous shortening and narrowing in a region. A passive shortening that is caused by external forces happens with widening of the tube. On the other hand, as the tube wall is not supported, the narrowing may only be originated by either a circumferential contraction in the wall or an internal negative pressure caused by wave propagation. In the latter, the wall will be

stretched (Jensen and Peddeley 1989). A simultaneous shortening and narrowing, therefore, (squeeze), which means a positive work on the fluid inside the tube as well as on the adjacent parts on the wall, may only be caused by an active contraction.

### **Third indication: Twist**

Considering the circumferential movements in the tube, yet another indication of activity can be found. When a bipolar twist is generated at some region along the tube and propagates in both directions, it is an obvious sufficient condition for activity. It shows there are some circumferential forces generated by contractile elements on the wall that cause this deformation. It is important to note that both sides of the tube are fixed and, therefore, the total angle of twist from the in-flow to outflow should be zero. Hence, the onset of a twist in the middle of the tube will be in the form of bipolar twist.

To determine the active regions of the embryonic heart using these indications, we need to extract quantitative characteristics of the heart tube contraction, including the longitudinal, radial and circumferential myocytes displacements, as well as the heart tube curvature, local volumetric squeeze fraction (VSF), and time resolved axial strain and torsion.

### **2.2.3 Mathematical Methods**

#### a) Lagrangian semi-cylindrical framework

In the early stages of development, the main axis of the heart tube is slightly curved, but remains almost stationary during the cardiac cycle. If the bend of tube axis is rectified to match a straight axis, we can best describe its deformation in a cylindrical coordinate system. All the imaged myocytes are divided into groups based on their positions at rest,

i.e., when the HT is not contracted. This sectioning is performed by layers with thickness of 4 to 5  $\mu\text{m}$  perpendicular to the overall direction of the tube. These groups include different numbers of data points (myocytes), which are non-uniformly distributed. To track the tissue, we use a Lagrangian coordinate system, which means members of each group do not change during the entire period.

For each individual myocyte, we define a longitudinal, radial, and circumferential direction. Since the tube is almost straight, these directions form a semi-cylindrical coordinate system. The position of the main axis of the tube is almost stationary; the longitudinal directions calculated for myocytes at rest, therefore, may be used for the entire cardiac cycle. Changes in the radial and circumferential directions, however, reflect the distortion and rotation of the tube wall, and were, therefore, computed at each time step, as described in the next subsection. Cell movements are decomposed into three mentioned directions, using the respective unit vectors. In the early stages, we assume the movement of the HT is symmetric around its main axis. To reduce the noise, therefore, each component of the movement is independently averaged over each axial section. This procedure results in the three-dimensional movement over a physical space that only resolved in the axial direction (one dimension). We call this a semi-1D problem.

#### b) Directions

Longitudinal, radial, and circumferential directions at each myocyte should first be defined for all time steps independently. To calculate the radial unit vectors, we estimate the directions perpendicular to the tube surface through a method developed by Amini and Duncan (1992). For each myocyte, we consider its 10 closest neighbors and collect their coordinates in a coordinate matrix as

$$C = \begin{bmatrix} x_i & y_i & z_i \end{bmatrix}_{n \times 3}, \quad (2.1)$$

The covariance matrix is calculated as

$$A = \text{cov}(C). \quad (2.2)$$

Next, the eigenvalues and eigenvectors of the covariance matrix are estimated,

$$A \cdot V_i = \lambda_i \cdot V_i. \quad (2.3)$$

The eigenvector corresponding to the *smallest* eigenvalue of the covariance matrix gives an estimate of a vector perpendicular (or normal) to the tube surface

$$\hat{n} \approx \hat{V}_1, \quad \text{with } |\lambda_1| < |\lambda_2| < |\lambda_3|. \quad (2.4)$$

Consequently,  $\hat{n}$  corresponds to the direction along which the positions of the cells in that neighborhood have the least amount of variation.

In contrast to the normal direction, which can be locally determined, the longitudinal direction  $\hat{t}$  should be calculated considering the cell distribution in a wider region. We extended this method for the longitudinal direction, therefore, by using a rough, “overall direction” of the curved tube. In the early stages of the heart tube development, this can be a straight line between two points at each end of the tube. For each myocyte, we define an anisotropic neighborhood using an ellipsoid such that the main axis is three times larger than the diameter, and is parallel to the overall direction of the tube (Fig. 2.2). The covariance matrix of the coordinates of these neighboring points is calculated and its eigenvalues and eigenvectors are determined. The eigenvector corresponding to the *largest* eigenvalue gives the direction in which the points are most distributed and so should be close to the longitudinal unit vector,  $\hat{t}$ . To have a more accurate

approximation, this procedure is repeated for each point by taking an ellipsoid whose main axis is along the previously computed direction instead of the tube's overall direction. This helps correcting the previously computed longitudinal unit vector. Figure 2.2 shows this procedure for two sample myocytes just before the contraction onset. Since we describe the displacement in a one-dimensional system along the axis of the tube, the longitudinal direction is averaged over all the cells in a given group and assigned to all the points in that layer.

After computing these directions independently at rest and at all other time points, we define the coordinate system for each myocardial cell, as follows. The longitudinal direction,  $\hat{t}$ , is taken at rest and is fixed for all time points. The normal vector,  $\hat{n}$ , at any given time point is substituted by its normalized projection on a plane perpendicular to  $\hat{t}$ ,

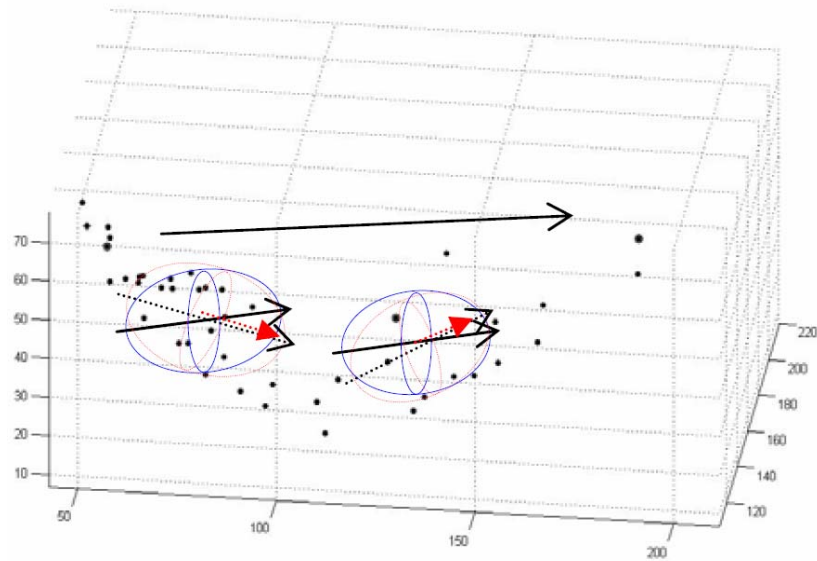


**Figure 2.2** The procedure for finding the longitudinal unit vector at each cell position is shown for two sample points. An ellipsoid is defined at each point, whose main axis has the same direction as the overall direction of the tube (solid ellipsoids and solid arrows). Based on the position of the neighboring points contained in the ellipsoid, a new ellipsoid is computed, whose direction is closer to the real local longitudinal unit vector (dashed ellipsoid and dashed arrows).



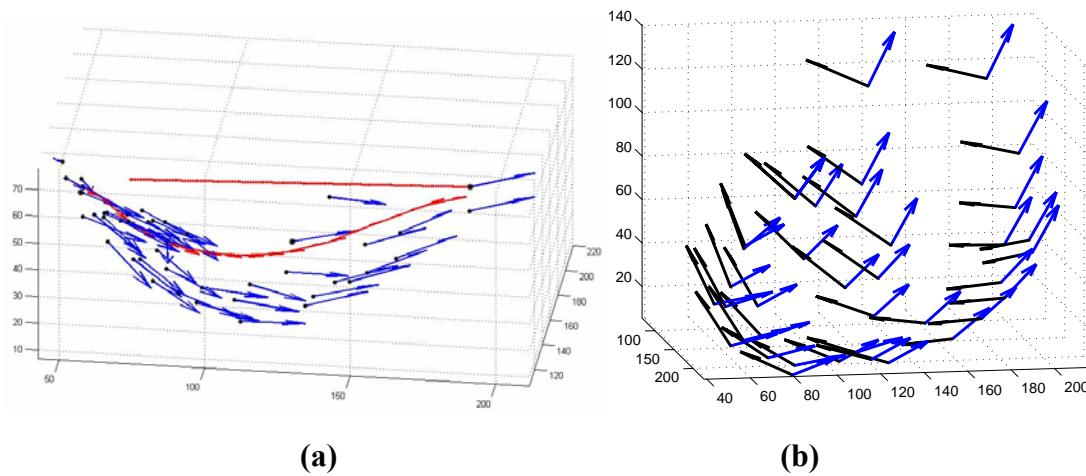


**Figure 2.4** Same dataset as in figure 2.2 (26hpf) (a) Calculated longitudinal unit vectors. The left side corresponds to the beginning of the tube (in-flow) and the right side to the end (out-flow). The straight line determines the *overall direction* while the curve shows one calculated path near the tube wall. (b) Myocytes and the calculated longitudinal and circumferential unit vectors for a 34 hpf embryonic heart at rest. The point of view is along the longitudinal direction, from the in-flow toward the out-flow. In both (a) and (b), data points are mainly located underneath the tube but for 34 hpf the data is incomplete at the very bottom. Coordinate system origins and directions as well as viewpoints in (a) and (b) are different.

### c) Spatio-Temporal smoothing

The point spread function (PSF) of the microscope determines the resolution of the image. The distance between slices in the through-plane ( $z$  direction) was chosen to be  $5\mu\text{m}$ , which is about half of the axial extent of the microscope PSF. Often, the measured displacement of the imaged myocytes is about, or less than, the order of magnitude of the PSF. Abrupt changes in the position of the myocardial cells along the  $z$  direction, therefore, are mainly caused by the large axial sampling step and additive noise. Averaging the displacement over the data points allows limiting the contribution of this artifact. We used a Gaussian filter to smooth the displacement in time and space, to

stabilize the calculations using noisy and sparse data. The sigma of the filter was set to 4.5  $\mu\text{m}$  in space and 7 ms in time.

d) Strain and Torsion calculation

As discussed in the methodology section, strain calculations can be used to determine the location of active sites in the embryonic heart. In a Lagrangian coordinate system, we may easily compute the one-dimensional strain of the embryonic heart along its main axis via differentiation of the longitudinal displacement of the particles. When the tube experiences a deformation in the longitudinal direction that changes the length of a tube piece from  $L_1$  to  $L_2$ , as shown in Figure 2.5 (a), the linear strain (Timoshenko et al. 1968) is calculated as

$$\varepsilon = \frac{\Delta L}{L_1} = \frac{L_2 - L_1}{L_1} = \frac{dl_2 - dl_1}{L_1}, \quad (2.5)$$

where  $dl_1$  and  $dl_2$  are the Lagrangian displacements of the two extremities of this piece. In Figure 2.5 (b) the longitudinal displacement is plotted versus the primary position along the tube. According to Equation (2.5), therefore, the strain,  $\varepsilon$ , is equal to the slope of the corresponding segment in this plot, i.e.,  $\tan(\alpha)$ . If we choose an infinitesimal piece of the tube, then the corresponding value of  $\varepsilon$  equals to the derivative of the plot. Considering the Lagrangian displacement as a function of the primary position  $f(L)$ , the strain is

$$\varepsilon = \frac{dl_2 - dl_1}{L_1} = \tan(\alpha) = \frac{df}{dL}. \quad (2.6)$$

Instead of a simple finite difference, we use the least-squares method to optimize the approximation of the linear strain. That is, at each point along the axial direction, we

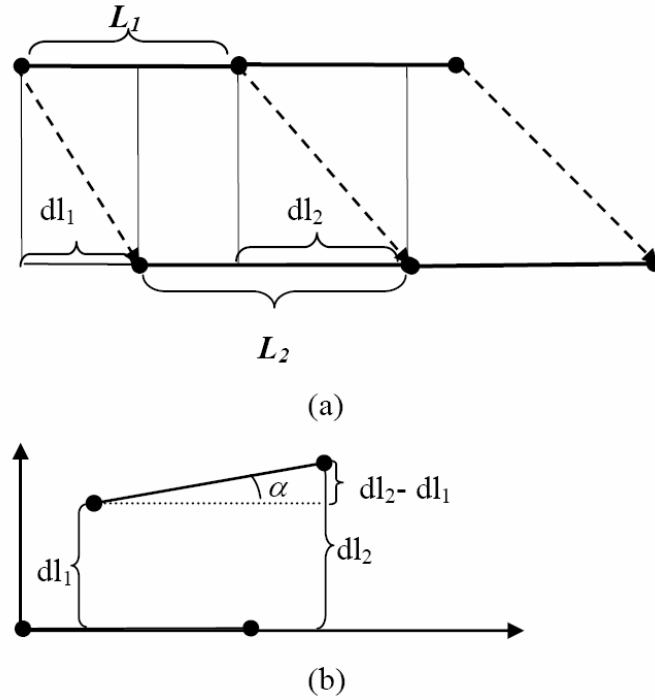


**Figure 2.5 (a)** An example of 1D displacement. A segment of length  $L_1$  has been deformed to a segment of length  $L_2$ . The longitudinal displacements of the two ends of this segment are  $dl_1$  and  $dl_2$ , respectively. **(b)** Plot of longitudinal displacement as a function of primary length that shows  $\tan(\alpha)$  corresponds to the longitudinal strain.

calculated this derivative based on its 7-point neighborhood to decrease the sensitivity of the derivation to noise.

Similarly, the angle of torsion  $\theta$  can be calculated as

$$\theta = \frac{g(L,t)}{R(L,t)}, \quad (2.7)$$

where  $g$  is the circumferential displacement function and  $R$  is the radius of the HT cross-section in a given position and time. The torsion angle per unit length  $T$ , therefore, which is the derivative of  $\theta$  with respect to the longitudinal position, may be computed as

$$T(L,t) = \frac{d\theta}{dL} = \frac{1}{R(L,t)} \left( \frac{dg}{dL} - \frac{dR}{dL} \cdot \frac{g}{R} \right). \quad (2.8)$$

#### e) Principal curvature estimation

If the tube is twisted or bent, the curvature can be quite different for two sides of the tube, e.g., the ventral and dorsal sides. Having the tube rectified along its main axis, however, we may assume that the cross section of the tube with any plane perpendicular to the axis is almost a circle whose radius is also known as the principal curvature of the wall at that point. To determine this curvature for each layer, we first find the vectors normal to the wall at each myocyte location in that group. Then, we extend those vectors and calculate their approximate intersection using a least-squares error method.

Since the measured spots are mainly distributed in a small portion of the wall, this calculation is very sensitive to noise, especially for the slices in which there are only few spots. In order to increase the calculation robustness, we compute the radius based on the normal vectors at 7 time points around the rest time of the heart tube. Furthermore, we apply a Gaussian filter to the computed curvature values to smooth the results spatially. The corresponding filter sigma was set to 4.5  $\mu\text{m}$ , about the thickness of the sections used for grouping the spots.

Once the radius is calculated for the rest position, we may estimate the volumetric squeeze fraction (VSF) factor, which shows the pump efficiency. The VSF is similar to the ejection fraction; while the latter is based on the lumen volume, however, the former is based on the volume surrounded by myocardium (epicardial surface). In the case of the Tg (*cmlc2*:GFP) zebrafish, the only information imaged about the heart tube comes from the myocardial cells, which constitute the outer layer of the tube wall. The total volume, therefore, is the summation of both the wall and internal volumes. For a valveless pump, the evaluation of the pumping efficiency poses another challenge

because the volume squeeze does not happen synchronously along the tube. To determine an estimate, therefore, we may define the VSF for each thin slice independently as a function of time that shows its volume change in the cardiac cycle. A slice VSF is determined as

$$VSF(L,t) = -\frac{\Delta V}{V} \approx -\frac{\Delta A}{A} - \frac{\Delta L}{L}, \quad (2.9)$$

where  $A$  and  $L$  are the cross-sectional area and the length of the tube segment respectively, and the slice volume  $V$  is  $A$  times  $L$ . The second term is the longitudinal strain,  $\varepsilon$ . Assuming the cross section of the tube is a circle, its primary area is estimated as  $A = \pi R^2$ , where  $R$  is the estimated radius of the tube at the distance  $L$  from the inflow when the tube is at rest. Having the radial variation of  $R$  at time  $t$  as  $\Delta R$ , the changes of cross section area is calculated as  $\Delta A = \pi(2R + \Delta R)\Delta R$ . Therefore VSF is estimated as

$$VSF(L,t) \approx -\frac{\Delta R(2R + \Delta R)}{R^2} - \varepsilon. \quad (2.10)$$

The total volume of the tube is also determined by integration of  $\pi(R + \Delta R)^2(1 + \varepsilon)$  along the tube for each time step. The term  $(1 + \varepsilon)$  acts as the Jacobian of the transformation from the Lagrangian to the Eulerian framework.

#### f) Wave Propagation Investigation

The tube contraction shows some wave propagation behavior that can even be observed visually in the sequence of unprocessed images. Recently, the mode of pumping of the early embryonic heart has been described as an impedance pump (Forouhar et al. 2006;

Hickerson et al. 2005). This model is based on the propagation of waves along the tube. Here, we quantitatively characterize this wave.

Wave propagation in the embryonic heart is a nonlinear phenomenon in a non-homogeneous structure, that makes an accurate analysis complicated. A simple approach to demonstrate the presence of a wave in the longitudinal wall motion, however, is by analyzing the timing of the *major displacement* for each slice along the tube. The major displacement is defined at each slice as 99% of its maximum longitudinal displacement. For a typical wave with a constant velocity, an almost linear profile is expected for the timing of the major displacement versus the position along the tube.

To distinguish between the observed wave and a wave that exists in a peristaltic pump we also measure the time of *major shortening* at all tube slices. The latter is defined as the time at which the myocardial cells experience 15% shortening (negative strain) or its maximum shortening, if it never reaches 15%. For a peristaltic pump, in contrast to an impedance pump, the strain is expected to be almost a constant wave that travels with a steady speed.

## **2.3 Results**

### **2.3.1 Calculation of the directions**

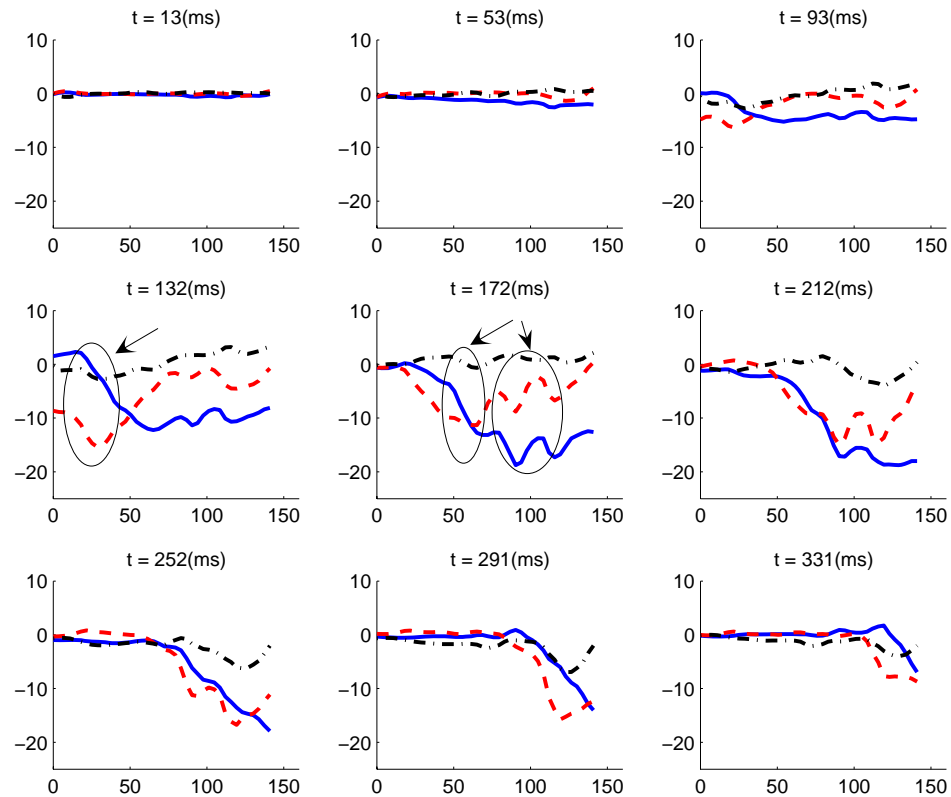
The mathematical methods described in §2.2.3(b) were used in both 26 hpf and 34 hpf data sets to calculate the three major directions at each myocyte. The results are shown in Figures 2.4 (a) and (b) for 26 and 34 hpf, respectively, and reveals the sparseness of the reliable points which are located mainly in the ventral side underneath the tube.

Figure 2.4 also shows that the concentration of the captured points at the beginning of the tube is larger than at its end. It should be noted that not all the myocytes in the scanned region have been captured on the images. We only chose those reliably captured during the whole cardiac cycle. The larger number of captured points in some regions of these graphs, therefore, does not mean that more myocytes are present in those regions. These images show that the accuracy of the method is enough for the purpose of this study. To avoid confusion, normal vectors have not been shown.

### **2.3.2 Slice Displacement**

The three components of the average displacement in each slice, versus the position along the long axis of the tube, have been plotted for the 26 hpf data set in Figure 2.6. Each plot shows these components for a specific time. Circumferential movements are not significant at this age. The longitudinal and radial displacements show a wavelike motion from left to right, which is the direction of the flow. In the beginning of the cycle, plots of the longitudinal motion exhibit an overall movement towards the in-flow extremity of the tube (negative value for longitudinal displacement). These plots show a negative slope for this plot near the in-flow, which presents a shortening. This negative slope moves towards the right, but not with a constant velocity.

Regions in which a large, negative strain occurs simultaneously with a major narrowing of the tube (local minimums of the dashed curve) are marked with ovals in two subplots. The first site is located close to the beginning of the tube and the other three are at 55, 80, 110  $\mu\text{m}$ , from this beginning.



**Figure 2.6** The longitudinal (solid line), radial (dashed line), and circumferential (dash-dotted line) displacements of cells for the 26 hpf dataset as a function of longitudinal position along the heart tube and for different time points in the cardiac cycle. Positions of high slope in the longitudinal displacement that coincide with a local minimum of the radial displacement are possible candidates for contraction sites. Arrows indicate four such positions. All distance units are in  $\mu\text{m}$ . The period of the beating is around 400 ms.

A comparison between the time at which the *major* axial displacement and the *major* shortening occur, both as defined in §2.2.3(f), can be seen in Figure 2.7. The very beginning of the tube has a different movement direction from the rest of the tube. It seems that the center of contraction toward which all myocytes are dragged, is around 20  $\mu\text{m}$  and, therefore, the very beginning of the tube experiences a positive axial movement when the rest shows a mainly negative displacement, with an almost linear profile for the

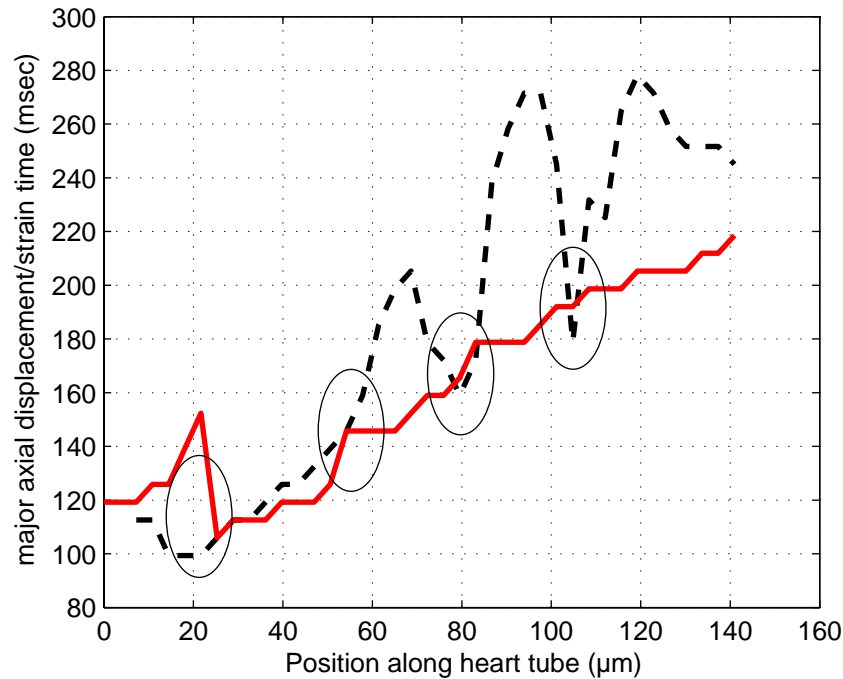


**Figure 2.7 Comparison at 26 hpf between the time of *major* axial displacement (time at which 99% of the maximum displacement for each slice occurs, solid line) and the time of *major* shortening (time at which the slice starts experiencing a 15% shortening (negative axial strain) or at which it reaches its minimum strain if it never reaches 15%, (dashed line). A delay between the shortening strain and the major displacement is known as a sign of passive behavior. From the plot, we infer that only a small portion at the beginning of the tube (up to 25  $\mu\text{m}$ ), as well as sites around 55, 80 and 110  $\mu\text{m}$  are active at this age.**

time of major displacement. The slope of the plot determines that the speed of the displacement wave is almost 1 mm/sec. In contrast, the time of major shortening exhibits a non-linear pattern. It shows that the major strain usually takes place after the major displacement except for a short region close to the in-flow tract, and small regions around 55, 80 and 110  $\mu\text{m}$ , that is, the same regions identified earlier that exhibit considerable negative strains and major narrowing simultaneously (Fig. 2.7).

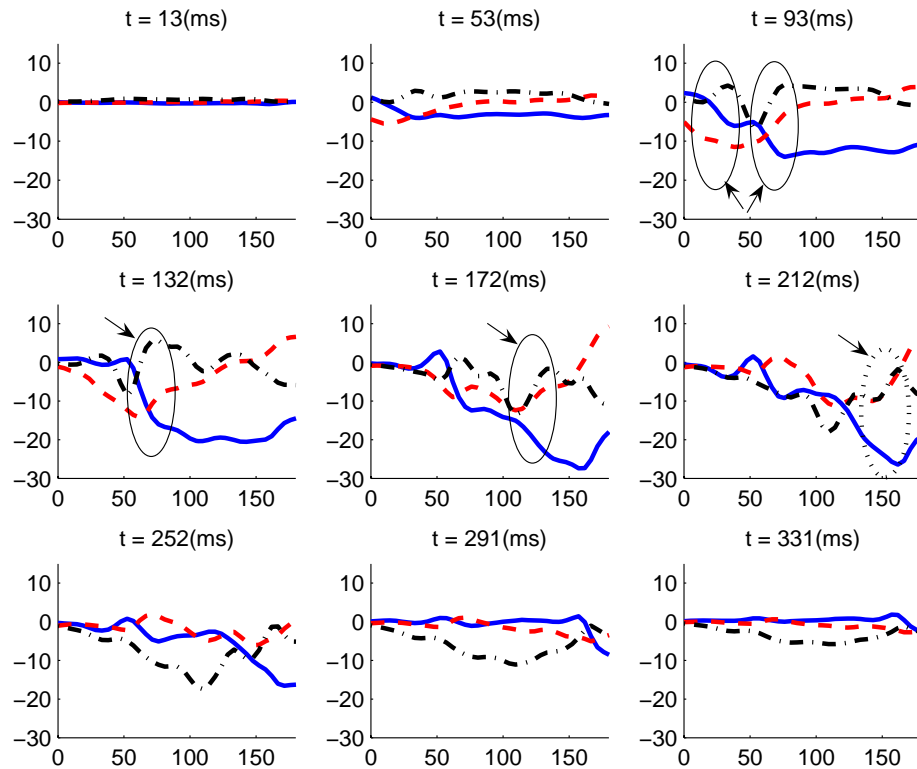


**Figure 2.8** The longitudinal (solid line), radial (dashed line), and circumferential (dash-dotted) displacements of the 34 hpf heart tube as a function of longitudinal position along the heart tube and for different time points in the cardiac cycle. All distance units are in  $\mu\text{m}$ . The period of the beating is around 400 msec.

Similar procedures were applied to the 34 hpf data set, too. It was observed that the circumferential movement at this stage was much more significant than that of 26 hpf. This movement, therefore, was also considered in addition to the radial and longitudinal displacements to determine active regions at 34 hpf (results in Figs. 2.8 and 2.9). The marked regions in Figure 2.8 around 20, 60, and 125  $\mu\text{m}$  show large negative strain (longitudinal displacement) simultaneously with major narrowing (radial displacement). Significant torsion, which can be inferred from the relatively strong bipolar circumferential movement, constitutes another evidence of activity. A fourth region around 150  $\mu\text{m}$  also shows the same active behavior but not as strongly as other sites.

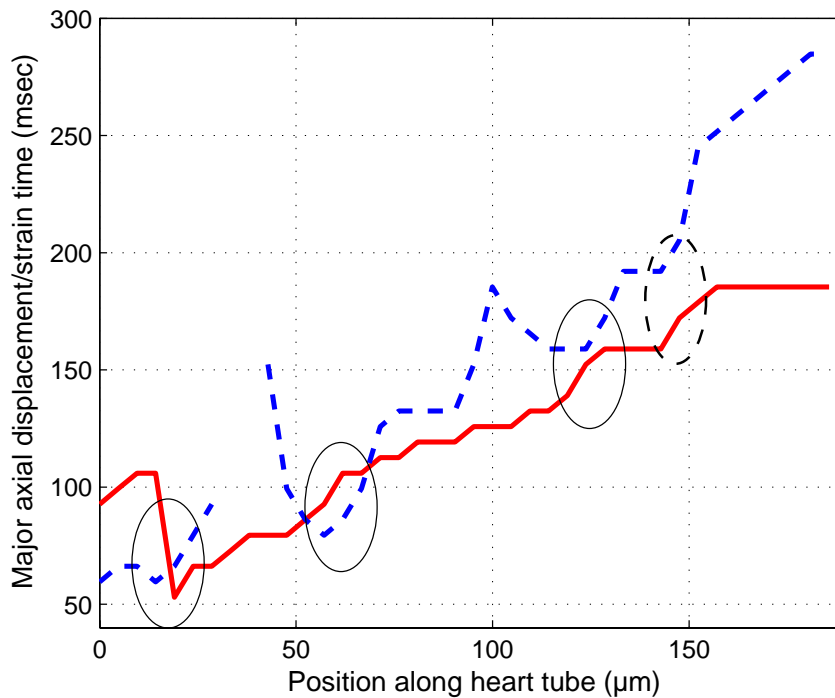


**Figure 2.9 Comparison at 34 hpf between the tim of *major* axial displacement (solid line) and the *major* shortening (dashed line). A small portion at the beginning of the tube (around 20  $\mu\text{m}$ ), as well as sites around 60, and 125  $\mu\text{m}$  are active at this age. A decrease in the delay at 150  $\mu\text{m}$  shows a possible activity site but not as clearly as at other three regions. The discontinuity of major shortening curve is caused by the fact that there was no shortening at 40  $\mu\text{m}$ .**

Figure 2.9 shows that the axial displacement travels at the speed of 1 mm/sec, which is approximately equal to the wave speed at 26 hpf age. This figure shows, furthermore, that the major shortening of the above three regions occurs just before or about the same time of their major displacement. In the fourth possible active site, however, the major shortening follows the maximal displacement with a delay of 25 ms, which is still the minimum amount of delay in its neighborhood. Similarly, a weak activity may be recognized around 90  $\mu\text{m}$  in both Figures 2.8 and 2.9. This activity is not strong enough, however, to be categorized along with activity in other sites. It should be noted that some activities mentioned here may depend on others, based on structural relations and,

therefore, may not be considered independently. Here we focus only on sites with major activities. Figure 2.9 shows a discontinuity in the plot of the major strain time. This discontinuity is caused by the fact that the region around the position of 40  $\mu\text{m}$  shows almost no shortening during the cycle. This interesting fact is discussed in §2.4.

### 2.3.3 Other parameters: Strain, Torsion, Curvature, and VSF

For both data sets, geometrical parameters, i.e., strain, torsion, curvature and VSF are calculated at all time steps and for all the slices. We have summarized the results as follows.

Figure 2.10 shows the range of changes of the axial strain at any given slice during the whole cardiac cycle at 34 hpf by showing its maximum and minimum. It is quite

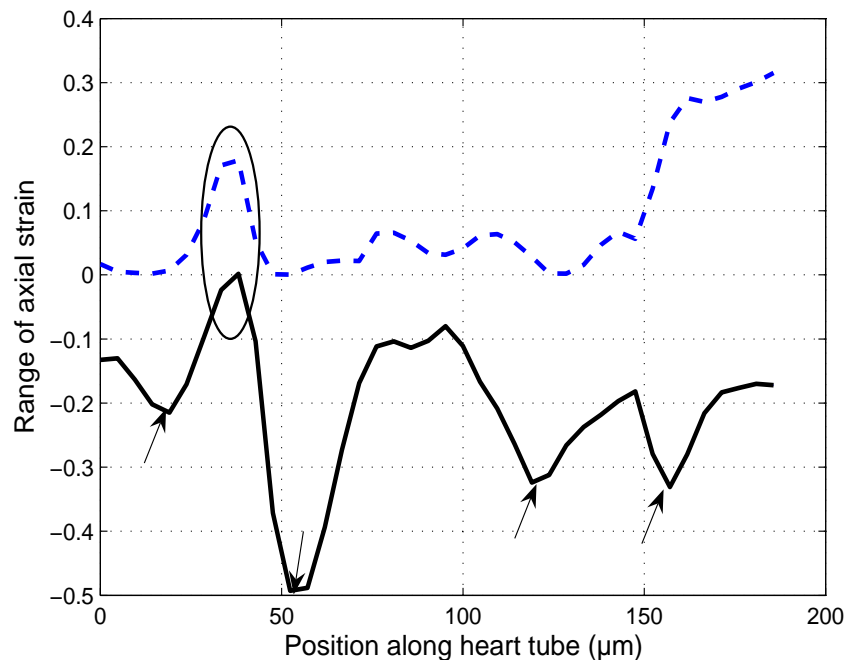


**Figure 2.10. Minimal (solid line) and maximal (dashed line) axial strains over the whole cardiac cycle as a function of the position along the length of the heart tube for a 34 hpf heart. Interestingly, sites where the shortening is maximal (minima in the solid line, indicated by arrows) correspond to possible active points. The position at 40  $\mu\text{m}$  exhibits lengthening but no shortening.**

remarkable that at the 40  $\mu\text{m}$  no shortening was observed, while a significant amount of shortening, up to 50%, exists in its neighboring points. Instead, the lengthening has a local maximum at 40  $\mu\text{m}$ . It also shows that for the three active sites mentioned in §2.3.2, i.e., around 20, 60 and 125  $\mu\text{m}$ , no stretch is seen while they are sites of local maximum shortening. The fourth possible active site at 150  $\mu\text{m}$ , however, has both the local maximum shortening and significant lengthening.

Figure 2.11 illustrates the calculated radius of the 26 hpf heart tube at each given slice when the tube is at its rest position. It also shows the minimum of the radius for each slice independently through the cardiac cycle. Calculation of curvature by using a limited

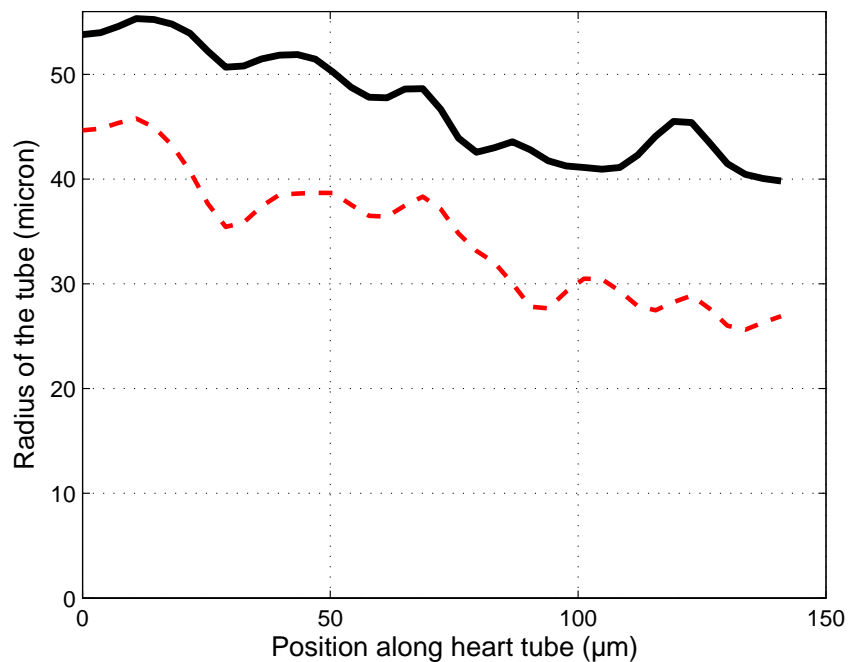


**Figure 2.11.** The calculated radius of the 26 hpf tube heart at each given slice when the tube is at its rest position (solid line). Dashed line shows the minimum of the radius for each slice independently through the cardiac cycle. Despite the sensitivity of the curvature calculation to the errors in normal unit vectors, the plot shows enough stability in the entire tube length. Therefore the calculated radius is accurate enough for the calculation of the torsion and VSF.

number of points that are mainly focused on a small part of the tube is highly sensitive to the errors in the position of those points, as well as the calculated normal unit vectors. According to Figure 2.11, nevertheless, the locally calculated radius changes smoothly along the tube. This means our computation method is stable and, therefore, the calculated radius is accurate enough for estimation of the torsion and VSF.

Since torsion only becomes significant at the age of 34 hpf, we only need to show the torsion at this age. Figure 2.12 shows the maxima and minima of the torsion in degree/ $\mu\text{m}$  in a rightward system looking from the in-flow. Remarkably, these local maxima and minima are complementary, except for the tract around the position at 150  $\mu\text{m}$ , the fourth possible active site.

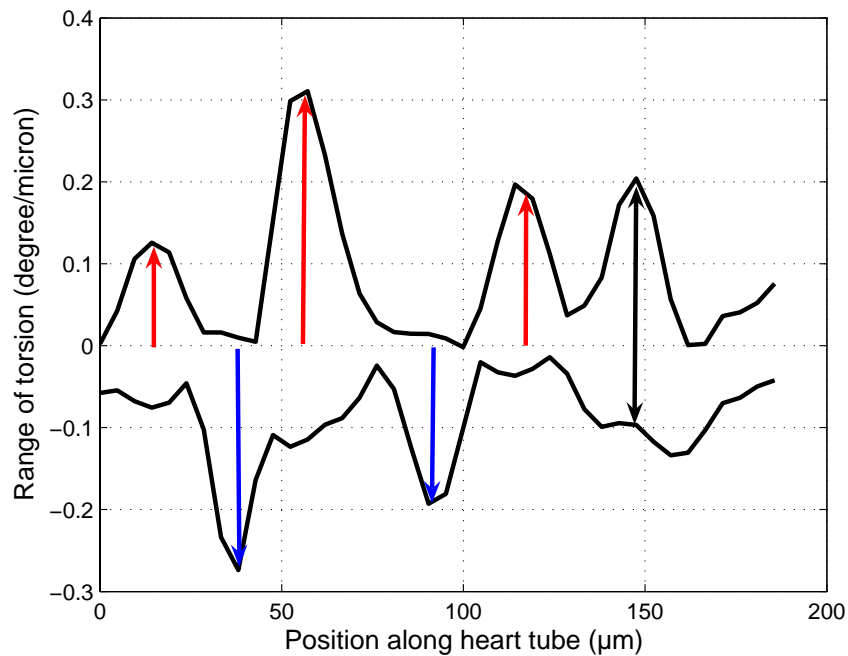


**Figure 2.12** The maximum and minimum of the torsion in degree/ $\mu\text{m}$  are shown along the axial direction. It is remarkable how complementary these local maximum and minimums are, except for the tract around the position of 150  $\mu\text{m}$ , the fourth possible active site.

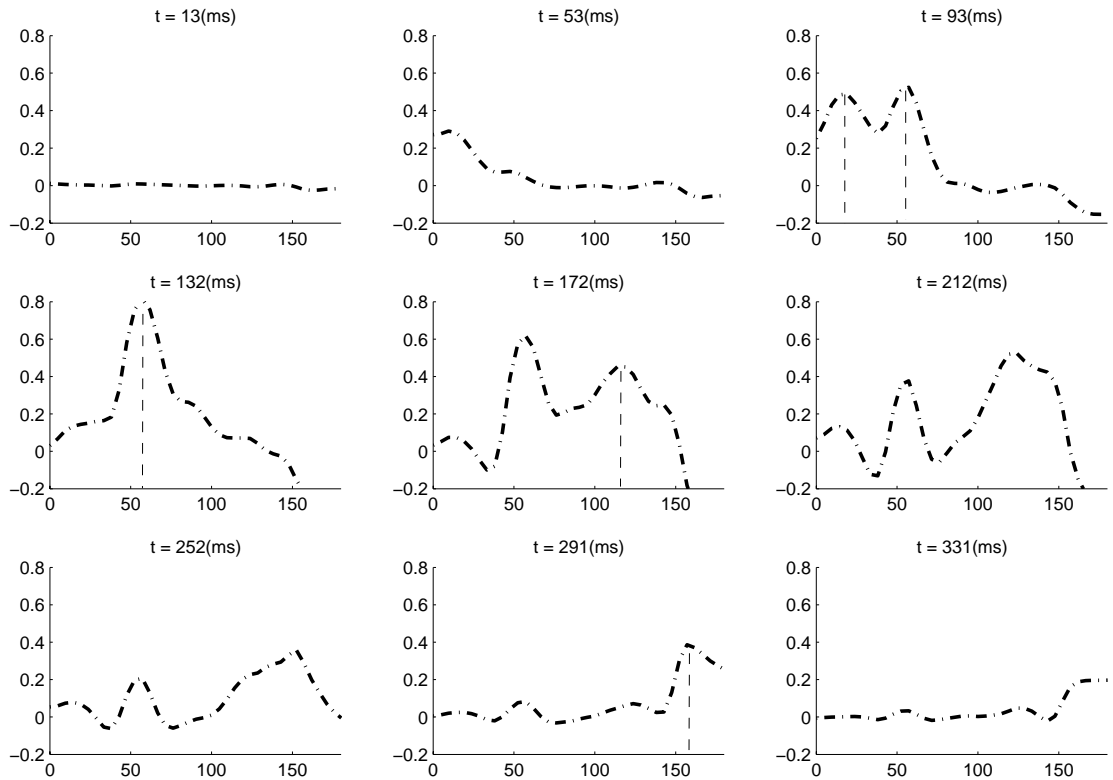


**Figure 2.13 Volumetric squeeze fraction at the age of 34 hpf for each slice as defined in equation (2.10). These plots determine the significant local volumetric squeeze fractions at the same four regions defined by other calculations as active sites. All distance units are in  $\mu\text{m}$ .**

Figure 2.13 shows the VSF for each slice at different times. The estimate of the total volume of the tube is shown in Figure 2.14, during the whole period. Both figures are for the age of 34 hpf.

## 2.4 Discussion of results

In this research, we introduced a Lagrangian semi-cylindrical coordinate system along with a host of computational methods, all of which produced a set of consistent results when applied to various quantitative measures of the HT deformation. The consistency of the results can be considered as a measure of the accuracy and robustness of the

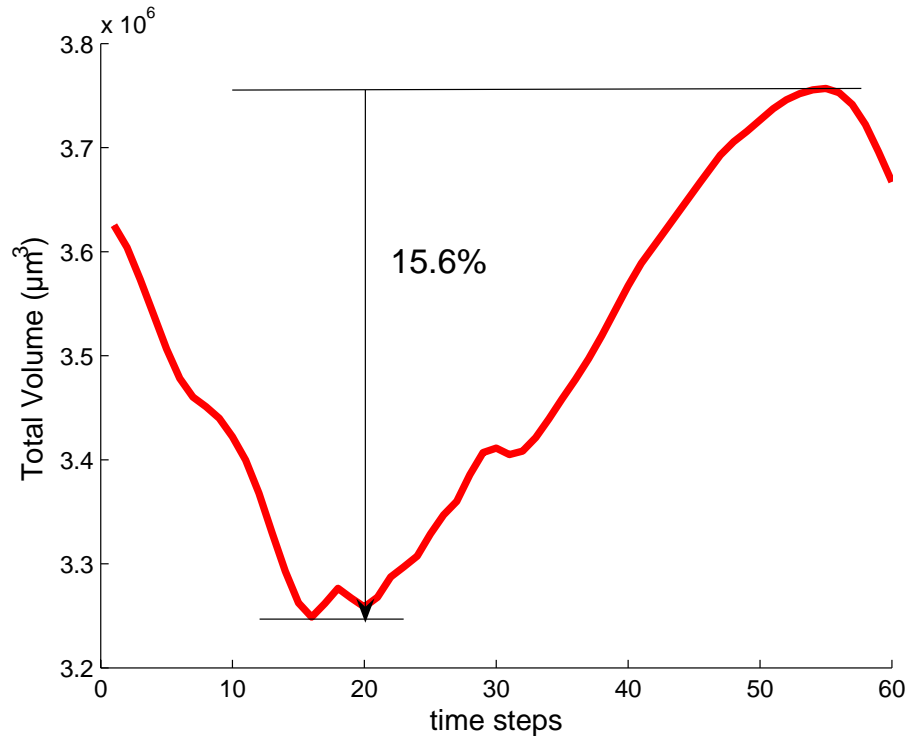


**Figure 2.14 Estimation of the total volume of the tube at each 60 time steps during the whole cardiac cycle. Although the local VSF can be as high as 80% for some slices, the maximum changes of the total volume is only 15.6%.**

approach. This approach helped in understanding the function of the embryonic heart by identifying the active sites along the heart tube versus passively reacting regions. For example, Figure 2.6 shows the wavelike propagation of the components of the displacement. Based on the observation of latter, we may consider four sites as possible active sites for the 26 hpf zebrafish. In these sites, the local maximum of the narrowing along the tube coincides with a maximum shortening. These regions are located around positions at 20, 55, 80 and 110  $\mu\text{m}$ .

This is in complete agreement with the results of the axial strain analysis shown in Figure 2.7. The main concept of the analysis is to consider the delay between the time of major shortening and major displacement. As explained in the methodology, a major

contraction prior to, or almost concurrent with, the major displacement is an indication of the activity. Figure 2.7 clearly differentiates the same active sites determined in Figure 2.6 from other points along the tube. The active region at the very beginning of the tube (near the in-flow) is wider than others and demonstrates the indications of the activity stronger than other active regions. Since it is also very close to the one extremity of the tube, the reflection of its contraction from that extremity can be quite significant. The interference of the reflected waves with the original activity in this region, therefore, may result in an impedance-pump behavior at this age (26 hpf).

Active sites in the heart tube for the 34 hpf zebrafish are recognized by scrutinizing the displacement components shown in Figure 2.8. In addition to coincidence of the maximum narrowing and shortening, another factor that can help predict the activity and passiveness of the segments at this age is derived from the circumferential movement (twist) in the tube. As explained in the methodology section, regions in which the twist is initiated should be active parts of the tube, especially if there is a close pair of twists in opposite directions, which suggests a springlike structure for the active element embedded in the tube wall. The conclusion about the location of the active sites at this age, therefore, is validated by the fact that a bipolar twist exists at each of these sites in Figure 2.8. These sites are located around positions at 20, 60, and 125  $\mu\text{m}$  from the in-flow. The region around 150  $\mu\text{m}$  is also a possible active site, but, as explained in §2.3.2, its activity is not as clear as for the other three sites. The strain analysis in Figure 2.9 shows total agreement with the location of active sites determined through analysis of the displacements in Figure 2.8.

It should be noted that neither the origin of the longitudinal axis, nor the size of these two data sets (26 and 34 hpf) are the same. Finding a correspondence between the points in these two datasets, therefore, is not straightforward. The distribution of the determined active sites along the tube, however, does not significantly change between 26 and 34 hpf. Also, the patterns of the major shortening time and wave propagation velocity are very similar in the two data sets.

Figures 2.10 and 2.12 show further characteristics of active sites. These sites show major shortening and large positive torsions, but, the last active site, which is in the vicinity of 150  $\mu\text{m}$ , shows the additional behavior of lengthening and negative torsion, as well. This additional phenomenon might be due to a short or weak activation of this site. This means that during some intervals of the cardiac cycle, this active site behaves as a passive region in response to, either the activity of other active sites, or its own reflection from the end of the tube. These two figures also elicit the behavior of passive parts. It can be observed from Figure 2.10 that no shortening has been measured at 40  $\mu\text{m}$ . Instead, that position exhibits a clear local maximum in the lengthening. Also, according to Figure 2.12, the torsion at the location of 40  $\mu\text{m}$  occurs in a direction opposite to that of its neighboring active sites. While Figure 2.12 shows similarity in the behavior of the tracts around the positions at 90  $\mu\text{m}$  and 40  $\mu\text{m}$ , these tracts do not show much similarity in Figure 2.10. It may be explained by assuming a weak activity for the tract around 90  $\mu\text{m}$  in a short period of time and then passive performance in other times.

Figure 2.13 completes our conclusion about the active sites along the embryonic heart tube by showing significant local VSF at the very same four regions.

## Limitations of the study

We have assumed there is an axial symmetry around the main axis of the tube after rectification. This assumption is not accurate, especially at 34 hpf stage, when the looping has been started. As each component of the movement was averaged in the slices perpendicular to the main axis, the methods are not able to discern between different sides of the tube and take their differences into account. There is a chance, therefore, that the local effects which exist only in one side of the HT are over- or underestimated at their corresponding slice.

The other limitation of this study is that the methods have been applied to only two data sets, one at each stage. We understand that for making any biological conclusion many more data are needed. The focus of this study, therefore, is the developed approach and methods such that they can be applied on the four-dimensional laser confocal microscopy images. This approach resulted in a set of consistent outcomes at these two stages.

## **2.5 Conclusion**

Here, an innovative kinematic-based approach has been presented to investigate the structure and function of the embryonic heart based on the spatial distribution of its active regions, and their role as the initiator of a wavelike passive wall deformation in the rest of the tube. Our approach is based on a Lagrangian semi-cylindrical coordinate system and accompanying computational methods. We applied these methods to images of fluorescently labeled zebrafish hearts obtained by four-dimensional confocal laser scanning microscopy at two developmental stages. The convergence of the results shows that these methods are sufficiently accurate and robust for the study of the early stages of

the zebrafish cardiogenesis. Furthermore, these computational tools revealed potentials of this imaging technique in providing detailed information about the HT geometry and kinematics like curvature, torsion and VSF. Our detailed studies of the two developmental stages confirmed our previous finding (Forouhar, 2006) regarding existence of selective active myocardial regions. This new understanding has provided better insights into the pumping mechanism of the embryonic heart by a more accurate identification of the active sites in the heart tube. Our approach also provides a clue for identifying regions of myocardial tube that may possess different material properties.

## 2.6 References

- Alford, P. W. and L. A. Taber (2003). "Regional epicardial strain in the embryonic chick heart during the early looping stages." J Biomech **36**(8): 1135-41.
- American Heart Association (2006). "Heart Disease and Stroke StatisticsM2006 Update." Dallas, TX: Am. Heart Assoc. DOI: 10.1161/CIRCULATIONAHA.105.171600.
- Amini, A. A. and J. S. Duncan (1992). "Differential geometry for characterizing three-dimensional shape change." Proc SPIE Math Methods Med Imaging **1768**: 170-181.
- Berne, R. M. and N. Sperelakis (1979). The Cardiovascular system. Baltimore, American Physiological Society.
- Buckberg, G. D., M. L. Weisfeldt, M. Ballester, R. Beyar, D. Burkhoff, H. C. Coghlan, M. Doyle M, et al. (2004). "Left ventricular form and function: scientific priorities and strategic planning for development of new views of disease." Circulation **110**(14): e333-6.
- Fishman, M. C. and K. R. Chien (1997). "Fashioning the vertebrate heart: earliest embryonic decisions." Development **124**(11): 2099-117.
- Forouhar, A. S., M. Liebling, A. Hickerson, A. Nasiraei-Moghaddam, H. J. Tsai, J. R. Hove, S. E. Fraser, M. E. Dickinson and M. Gharib (2006). "The embryonic vertebrate heart tube is a dynamic suction pump." Science **312**(5774): 751-3.
- Gilbert, S. F. (2000). Developmental biology. Sunderland, Mass., Sinauer Associates: xviii, 749 p.
- Hashima, A. R., A. A. Young, A. D. McCulloch and L. K. Waldman (1993). "Nonhomogeneous analysis of epicardial strain distributions during acute myocardial ischemia in the dog." J Biomech **26**(1): 19-35.
- Hickerson, A. I., D. Rinderknecht and M. Gharib (2005). "Experimental study of the behavior of a valveless impedance pump." Experiments in Fluids **38**(4): 534-540.
- Hove, J. R., R. W. Koster, G. Acevedo-Bolton, S. E. Fraser and M. Gharib (2003). "Intracardiac fluid forces are an essential epigenetic factor for embryonic cardiogenesis." Nature **421**(6919): 172-7.

- Huang, C. J., C. T. Tu, C. D. Hsiao, F. J. Hsieh and H. J. Tsai (2003). "Germ-line transmission of a myocardium-specific GFP transgene reveals critical regulatory elements in the cardiac myosin light chain 2 promoter of zebrafish." Dev Dyn **228**(1): 30-40.
- Jensen, O. E. and T. J. Pedley (1989). "The Existence of Steady Flow in a Collapsed Tube." Journal of Fluid Mechanics **206**: 339-374.
- Jin, S. W., D. Beis, T. Mitchell, J. N. Chen and D. Y. Stainier (2005). "Cellular and molecular analyses of vascular tube and lumen formation in zebrafish." Development **132**(23): 5199-209.
- Liebling, M., A. S. Forouhar, M. Gharib, S. E. Fraser and M. E. Dickinson (2005). "Four-dimensional cardiac imaging in living embryos via postacquisition synchronization of nongated slice sequences." Journal of Biomedical Optics **10**(5):- eid 054001-1-10.
- Nakamura, A., R. R. Kulikowski, J. W. Lacktis and F. J. Manasek (1980). Heart looping: a regulated response to deforming forces. In R. van Praagh, A. Takao, editors. Etiology and morphogenesis of congenital heart disease. Mount Kisco, NY: Futura Publishing. p 81–98.
- Nerurkar, N. L., A. Ramasubramanian and L. A. Taber (2006). "Morphogenetic adaptation of the looping embryonic heart to altered mechanical loads." Developmental Dynamics **235**(7): 1822-1829.
- Romanoff, A. L. (1960). The avian embryo; structural and functional development. New York, Macmillan.
- Taber, L. A., H. Sun, E. B. Clark and B. B. Keller (1994). "Epicardial strains in embryonic chick ventricle at stages 16 through 24." Circ Res **75**(5): 896-903.
- Taber, L. A. (1995). "Biomechanics of growth, remodeling, and morphogenesis." Applied mechanics reviews **48**(8): 487-545.
- Timoshenko, S. and D. H. Young (1962). Elements of strength of materials. Princeton, N. J., Van Nostrand.
- Tobita, K. and B. B. Keller (2000a). "Maturation of end-systolic stress-strain relations in chick embryonic myocardium." Am J Physiol Heart Circ Physiol **279**(1): H216-24.

- Tobita, K. and B. B. Keller (2000b). "Right and left ventricular wall deformation patterns in normal and left heart hypoplasia chick embryos." Am J Physiol Heart Circ Physiol **279**(3): H959-69.
- Trinh, L. A. and D. Y. Stainier (2004). "Cardiac development." Methods Cell Biol **76**: 455-73.
- Vogel, S. (1994). Life in moving fluids : the physical biology of flow. Princeton, N.J., Princeton University Press.
- Zamir, E. A. and L. A. Taber (2004). "Material properties and residual stress in the stage 12 chick heart during cardiac looping." J Biomech Eng **126**(6): 823-30.

## Methods to Measure 3D Systolic and Diastolic Strain Patterns in the Left Ventricle from DENSE MRI

### 3.0 Abstract

Displacement-encoded imaging with stimulated echoes (DENSE) provides high temporal and spatial resolution measurement of three-dimensional Lagrangian displacement over the whole cardiac cycle. Data acquisition in this manner, however, is time consuming. The goal of this study is to use effective analytical and image processing tools to increase the derived information from acquired DENSE magnetic resonance imaging (MRI) data. Namely, we calculate the map of out-of-plane components of the Lagrangian strain tensor in addition to in-plane components from a single-slice DENSE MRI dataset covering both systolic and diastolic parts of the cardiac cycle. Feasibility of the method is shown in a human subject, and results are compared to those of other studies. The methods developed in this study are general and can be used with other data acquisition techniques, such as zHARP, that capture three-dimensional displacement.

### 3.1 Introduction

Left ventricular function is a complex process involving contraction (systole) and expansion (diastole), designed to propel blood around the body with each stroke. The left ventricular volume changes associated with this cardiac output have long been known to

be complex (Parmley 1979), and it has been realized that there are significant local variations in the time course, magnitude, and pattern of deformations within the myocardial wall (Humphrey 2002). In humans, systolic myocardial shortening and diastolic lengthening vary with longitudinal position along the left and right ventricular free walls on a long-axis plane. Moreover, in the course of heart failure and other cardiac diseases and deficiencies, wall deformations become very pronounced and vary from the normal, healthy function of the myocardium. It is, therefore, of immense use to be able to capture these abnormal deformation patterns as possible indices for determining the nature and extent of cardiac malfunction. For a full description of myocardial contraction, Lagrangian data are essential. This form of data ensures that the behavior (displacement and distortion) of the same particles within the myocardial tissue are followed in the frame of reference, what is commonly referred to as “tissue tracking.” Conversely, in an Eulerian coordinate system, displacement vectors of the same coordinate point but different times are not necessarily of the same tissue. In principle, the integration of the Eulerian velocity should yield the path of each material point and its corresponding strain values. In practice, serious numerical difficulties arise. At a given instant in time, the estimated position may not correspond to the true position of the material point, thus the velocity or displacement measured at this location will not coincide with its true value.

Much of the basic research in the past has been carried out in experiments on animals under anesthesia with open chest, which leads to measurable modifications of true physiology. Sonomicrometry, for example, has been used for the purpose of determining strain values and twist motions in the cardiac wall (Ratcliffe, Gupta et al. 1995). In the past 20 years, standard *in vivo* MRI has allowed a non-invasive means for the direct

examination of many of these concepts in the living heart. In particular, variations in wall thickening around the ventricular circumference and shortening of the ventricles can be readily quantified in real time. While standard MRI relies upon identifying the endocardial and epicardial borders of the heart, it yields little information about the myocardial wall itself. Three MRI techniques are now available which can be used to track individual points in the myocardial wall at various time points in the cardiac cycle. These are tagging (Zerhouni, Parish et al. 1988; Axel and Dougherty 1989), phase contrast (Bryant, Payne et al. 1984; van Dijk 1984; Pelc, Drangova et al. 1995), and DENSE (Aletras, Ding et al. 1999).

In general, the fundamental difficulty in recovering myocardial motion from the temporal sequence of snapshots of the velocity or displacement field acquired by conventional techniques, such as cine phase-contrast velocity imaging (Pelc, Sayre et al. 1994), is that Eulerian displacement fields are measured, while the objective is to derive the Lagrangian path of each object point (Meyer, Constable et al. 1996), as mentioned earlier.

Myocardial tagging with spatial modulation of magnetization (SPAMM) (Zerhouni, Parish et al. 1988; Axel and Dougherty 1989) is capable of revealing intramyocardial tissue motion. In tagging, black lines or “tags” in the myocardium are generated by a sequence of radio-frequency and magnetic-field gradient pulses, which are used to saturate parallel planes of magnetization perpendicular to the imaging plane. In order to reconstruct the three-dimensional motion of material points, a number of two-dimensional tagged image sections must be obtained in at least two orientations, usually aligned parallel and perpendicular to the longaxis of the left ventricle. By providing a

limited number of “markers” across the myocardium itself, tagged MRI allows for complex twisting motions during systole and diastole to be recognized. As well as poor spatial resolution in MR tagging, however, it remains a fundamental problem to track tags over a complete cardiac cycle, comprising both systole and diastole, due to the fading of the tags over time. This is often remedied by performing a second acquisition (‘retagging’) somewhere later in the cardiac cycle. The same tissue elements, however, are generally not tagged in each of the two processes. Hence, the motion fields derived from two tagging processes may be incoherent. Another remedy for the tagging method is the harmonic phase (HARP) imaging technique (Osman, Kerwin et al. 1999) which has the potential of rapidly detecting tag locations without the need for myocardial segmentation. In comparison to regular tagging, HARP also gives better spatial resolution which is limited by the spatial resolution of the image rather than the density of tagging pattern.

Nevertheless, only in-plane motion, which is the approximated two-dimensional projection of the three-dimensional motion of the material points, can be obtained from tagging or HARP techniques directly. These techniques, therefore, acquire the displacement data not purely in the Lagrangian frame. In order to obtain data pertaining to three-dimensional motion, two-dimensional tag data must be acquired in two orthogonal views, typically short and longaxis, as mentioned above. Once again, the same tissue elements are not always tagged in each of the two views and, therefore, the motion in each view can only partially contribute to an overall scheme aimed at estimating the complete three-dimensional motion and deformation. Slice following (SF), in combination with sequences such as CSPAMM (Stuber, Spiegel et al. 1999), also

go some way in alleviating the aforementioned problems. The recently proposed method, zHARP (Abd-Elmoniem, Stuber et al. 2005), which is a modified version of SF-CSPAMM, uses HARP processing to provides three-dimensional displacement in a Lagrangian frame. The methods developed in this study are, therefore, applicable to zHARP as well.

Detailed functional data at a macroscopic (tissue) level can be acquired by the application of displacement-encoded imaging with stimulated echoes (DENSE), a phase contrast method of imaging (Aletras, Ding et al. 1999). In this technique, a series of phase-labeled images are acquired at the same time point in the cardiac cycle, while the time labeling is moved along the cycle. The result is that the same data point in the image always corresponds to the same physical tissue, while its phase marks the former positions of that tissue at the various phases of cardiac motion. The ‘back-tracking’ ability makes DENSE a suitable technique to acquire the Lagrangian displacement field (Wen and Bennett 2004). This method provides more data points across the myocardial wall than can be achieved by MR tagging for a more elaborate analysis. This approach will also be more tolerant of physiological motion and more reliable *in vivo* and may, therefore, give rise to novel information about cardiac-wall motion. Moreover, DENSE has been used successfully, thus far, in detecting small focal regions of abnormal contraction in patients (Aletras, Wen et al. 2000), in characterizing mouse ischemia models (Gilson, Yang et al. 2002), and in acquiring detailed functional data of canine hearts *in vivo* (Wen, Bennett et al. 2005). Kim et al. have used tissue tracking of human hearts via two-dimensional breath-hold cine DENSE imaging (2004), although this method is not Lagrangian either.

Availability of new MRI modalities such as DENSE and zHARP that allow capturing high-resolution, 3-D Lagrangian motion from a single, acquired-image orientation, also demand analytical methods that can take advantage of these new capabilities to obtain functional data, such as strain field information. In this work, we have introduced some novel approaches that will complement the current MRI-based quantitative analysis techniques. Specifically, our technique is suitable for analyzing Lagrangian image data sets in all three coordinate dimensions and for deriving maps of all six elements of the strain tensor. The importance of calculating out-of-plane strains from a single slice is further emphasized by noting that our chosen DENSE imaging process tends to be very time consuming, and also that the distance factor (i.e., distance between consecutive short-axis slices of the left ventricle) is generally too large in most strain imaging techniques (especially in zHARP) to derive accurate information in the perpendicular (long axis) direction.

Our aim is to employ effective analytical and image processing tools to increase the derived information acquired from the three-dimensional deformation of a slab of myocardium, through DENSE MRI data, and to determine patterns of true myocardial motion in a Lagrangian frame. Our methods are sufficiently general, however, that they can easily be applied to other three-dimensional deformation imaging methods (e.g., zHARP) as well. We calculate the out-of-plane components of the Lagrangian strain tensor in addition to in-plane components from a single-slice DENSE MRI dataset covering a complete cardiac cycle. Finally, we demonstrate the feasibility of the method in a human subject and conclude by comparing our results to those of other studies.

## 3.2 Methods

### 3.2.1 DENSE MRI Data Acquisition

Details of the DENSE method are provided in previous publications by Aletras et al. (1999, 2000). In brief, a stimulated echo acquisition (STEAM) sequence is used to encode position information of the voxels into their phase. The phase information is preserved over the cardiac cycle by the STEAM sequence. Displacement of the voxels in three-dimensional space during this time is reflected in their phase changes and can be measured accurately.

In this study, DENSE MRI images were acquired on a Siemens Trio 3T MR whole-body scanner at the Caltech brain imaging center with an eight-channel cardiac array coil. A single-slice long-axis (LA) dataset of high spatial and temporal resolution was acquired from the heart of a healthy 25-year-old female volunteer with informed consent. The experiment was carried out under free respiration conditions over a period of 45 minutes. To synchronize the RF pulses with the motion of the chest and heart, respiratory and heart monitoring were achieved using a pneumatic bellows and ECG.

In order to directly acquire Lagrangian displacement vectors relative to a fixed time during the cardiac cycle, the image acquisition section of the DENSE sequence was positioned at a constant 600 ms after the R wave of the ECG trigger, while the encoding section was placed at a series of times steps after the trigger.

The imaging parameters were as follows: field of view (FOV) was 192 mm  $\times$  110 mm; the size of the acquisition matrix was 128  $\times$  72, giving a final spatial resolution of 1.5 mm

$\times 1.5$  mm while the slice thickness was 5 mm. 20 phases, each of 30 ms duration, were collected, which together cover 600 ms of the cardiac cycle starting 30 ms after detection of the QRS complex (acquisition window = 850 ms). In this manner, all major deformations from the beginning of systole throughout most of diastole were covered. The heart is almost at rest during the part of the cycle not captured in the imaging process (almost 200 ms) and so no major strain is expected on that period. Other parameters are as follows: TR = 3.1 ms; TM = 600 ms; number of averages = 3; the displacement encoding sensitivity is 0.503 radians/mm for in-plane directions and 0.587 radians/mm for the out-of-plane direction.

### **3.2.2 DENSE Data Post-Processing**

After obtaining the DENSE images, segmentation is performed by masking all parts of the anatomy except for the myocardium. Since DENSE always acquires the image at a specific time from the beginning of the cardiac cycle, each point is supposed to be at a constant position at all frames. Performing segmentation for only one time frame, therefore, is enough for all other time steps. Having the three components of the displacement at all points, it is possible to generate an image that shows the displacement magnitude of pixels. If we create this image at a time point that has undergone a major displacement, it can be a good indicator of myocardial anatomy and, hence, a good template for segmentation by manual masking of other tissues. It is useful to have the displacement magnitude images of a few phases together when performing the manual masking, as it helps avoid inaccurate masking at noisy points. For this study, we have masked all parts of the heart other than left ventricle (LV).

Phase unwrapping has then been done on the segmented images by scanning the myocardium area while searching for sudden changes in displacement magnitude. These changes are fixed later by adding or subtracting the correction values, which are proportional to the  $2\pi$  changes in phase. This step was repeated separately for all three directions of displacement and for all phases. Filtration of the displacement vectors was performed at this step and will be explained in Section 3.2.4.

The acquired long-axis data proved to be amenable to analysis by solid mechanics methods. Deformation gradient matrices were calculated from the displacement vectors for each of the myocardial material points provided by DENSE MRI data at every time frame. The strain maps could then be generated from these matrices by describing the deformation of the left ventricle in the Lagrangian reference frame.

### 3.2.3 Deformation Gradient Tensor

The deformation of a continuum is described by the second-order deformation gradient tensor  $\underline{\underline{F}}$ , which relates the vectors connecting two material points before, and after, deformation. Calling the position of the material particles as  $X$  and  $x$  in the reference and deformed configurations respectively, matrix  $\underline{\underline{F}}$  transforms length element  $dX$  in the reference frame to that of  $dx$  in the deformed frame:

$$\underline{dx} = \underline{\underline{F}} \cdot \underline{dX} . \quad (3.1)$$

Once  $F$  is computed, the strain tensor  $E$  can be calculated accordingly:

$$E_{ij} = 0.5 \left( \sum_k F_{ki} F_{kj} - \delta_{ij} \right), \quad (3.2)$$

where  $\delta_{ij}$  is the Kronecker delta function.

### 3.2.4 Displacement smoothing

The elements of the deformation gradient tensor are calculated by derivation ( $F_{ij} = \partial x_i / \partial X_j$ ) and are, therefore, very sensitive to any noise in the measured displacement. As a remedy to this problem, smoothing the measured displacement is needed, based on our knowledge of the physics of this deformation. For instance, we know that the significant temporal frequencies of the heart motion are lower than five times the heart rate (Young 1991). A 5th-order Fourier basis function should, therefore, be sufficient for temporal fitting.

Noise can induce some outlier points in the tissue tracking process. These outliers can generate large errors in the calculation of the local strain. A five-pixel median filter has been applied to each component of the displacement vector to reduce the outliers effect.

We observed that these two simple steps provide enough smoothness to achieve reliable calculation for in-plane components of the deformation gradient matrix. Although components of  $F$  relating to out-of-plane direction are more noise sensitive, no further filtering or smoothing was applied to the displacement in that direction. Instead, we tried special methods to calculate individual elements of the matrix  $F$  which determine the out-of-plane deformation.

### 3.2.5 Estimation of Deformation Gradient Tensor

To minimize the noise effects,  $\underline{\underline{F}}$  is estimated via the least-square method, i.e., by minimizing the following quantity for every point over its neighborhood covering almost  $50 \text{ mm}^2$  ( $0.5 \text{ cm}^2$ ) of the material area in the imaging plane:

$$\sum \|\underline{dx} - \underline{F} \cdot \underline{dX}\|^2. \quad (3.3)$$

Theoretically, we should be able to calculate all elements of the matrix  $F$  even from a single-slice DENSE image. This results from the fact that, unlike MR tagging techniques, DENSE is able to measure out-of-plane displacements in a full Lagrangian framework. That is, a surface instead of a plane is studied and, therefore, out-of-plane gradients may potentially be measured from the surface curvatures. It is important to note, however, that this problem is very close to inducing singularity conditions in the deformation matrix, as would be the case if all data were positioned on one plane. Thus, due to the smaller spatial variation, the gradients in the direction normal to the surface are highly noisesensitive. What this means is that for the typical material point neighborhood mentioned above, the variation of the out-of-plane coordinate ( $\sim 0.8$  mm) is almost one order of magnitude less than that for in-plane components ( $\sim 8$  mm), whereas the expected absolute error of positioning is constant in all directions. Consequently, the expected error in calculation of the out-of-plane elements of the matrix  $F$  (henceforth termed  $\delta_2$ ) is almost one order of magnitude greater than the same quantity for in-plane elements ( $\delta_1$ ).

Considering the image plane as  $XY$ , the first two columns of the matrix  $F$  can be easily calculated by using this method, but the third column ( $\partial/\partial Z$  gradients), which has the major role in the calculation of out-of-plane strains, does not have reliable values, as explained above.

In order to compute out-of-plane strains, we have employed mathematical methods along with physical assumptions, to account for the aforementioned noise sensitivity. As a first step, the calculation of elements  $F_{13}$  and  $F_{23}$  of the deformation gradient matrix, which

represent the effects of out-of-plane displacements on in-plane deformation, was stabilized by biasing the distribution of the neighboring points used in the least-square method in the first and second directions, respectively (Fig. 3.1). These elliptical neighborhoods decrease the noise sensitivity by increasing the small variation of the coordinates in the out-of-plane direction (an almost 20% in the variation, i.e., from 0.8 mm to 1 mm). More importantly, it

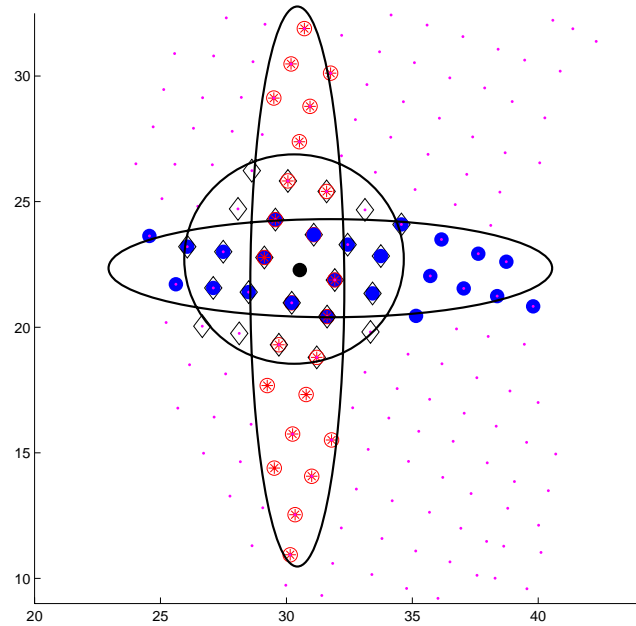


**Figure 3.1.** Small points show a selection of the material points in the apex of the heart, captured in a single image slice. The circle in the middle shows the point used in the calculation of the first two columns of the matrix  $F$ . The two ellipsoids show the weighted directions that are used to estimate  $F_{13}$  and  $F_{23}$ .

also decreases the effect of noise by considering more global behavior, that is, extending the region in the targeted direction causes the noise to be averaged over a higher number of points in the same row.

When we extend the neighborhood in the first direction and try to recalculate the first row of the matrix  $\underline{F}$  (i.e.,  $F_{1i}$ ), it is possible to keep the second element,  $F_{12}$ , fixed as the range of the points' coordinates in the second direction is small. In this manner, we calculate  $F_{11}$  and  $F_{13}$ , as if all points of the neighborhood were located in one row; consequently, the noise in the out-of-plane direction will be averaged and considerably decreased. As  $F_{11}$  is more accurate, only the  $F_{13}$  is replaced in the matrix  $F$ .

A similar procedure is performed to obtain  $F_{23}$ . However, this trick obviously does not work for  $F_{33}$ . Using extended neighborhoods means that to calculate  $F_{13}$  and  $F_{23}$ , the smaller local ‘indentations’ are neglected, while the focus merely remains on the more global effect of out-of-plane direction on the in-plane deformation. We should, therefore, expect to miss small local changes in the out-of-plane strains.

### 3.2.6 Anti-deformation gradient matrix $G$

$F$  is the tensor that transforms the rest positions of the myocardial points within a neighborhood to an arrangement as close as possible to their deformed shape. It is possible to simultaneously define the tensor  $G$  to do the exact inverse operation. Ideally, matrix  $G$  should be the inverse of matrix  $F$ , but this is not the actual case, since we can only estimate each of these matrices. Application of these matrices on the neighborhood

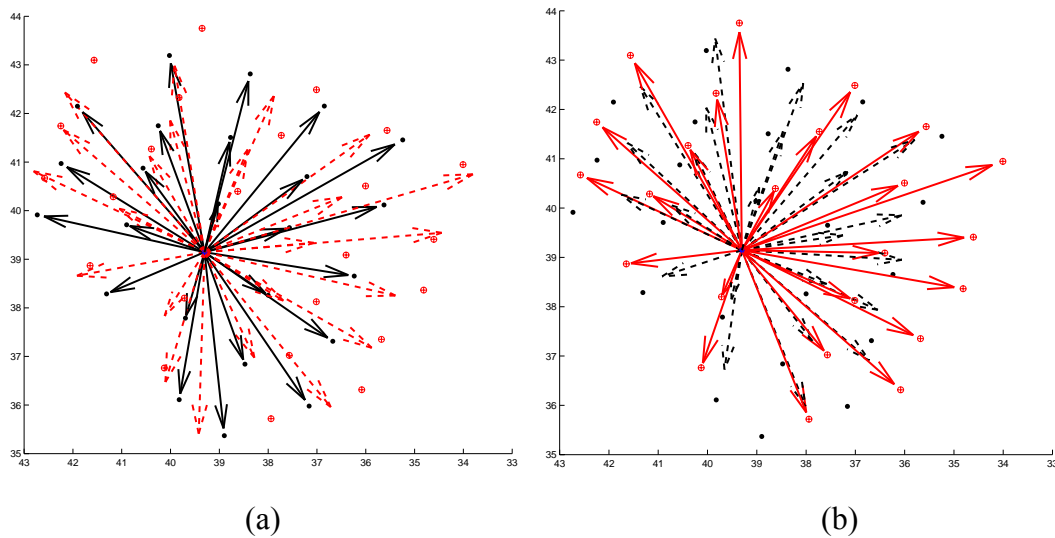


**Figure 3.2.** One sample point and the material points in its neighborhood are shown in black dots. After deformation, the relative positions of the neighboring points are moved to red points. (a) The effect of matrix  $F$  in modeling this deformation. ( $\underline{dx}$  is shown in black vectors and  $\underline{F} \cdot \underline{dX}$  is shown in red dashed vectors). (b) The effect of  $G$  on the deformation of  $\underline{dx}$  (solid red vectors) to  $\underline{G} \cdot \underline{dx}$  (dashed black vectors). Neither of the matrices performs the perfect matching of original and deformed points.

of a sample point is shown in Figure 3.2.

We know the calculated  $F$  and  $G$  are acceptable approximations for the first two columns of the deformation gradient matrix and its inverse. They both have accuracy problems, however, in their third columns. It is important to note that the error in the calculation of  $F_{13}$  and  $F_{23}$  can be very different from that of  $G_{13}$  and  $G_{23}$ . For instance, a very small variation of the out-of-plane position of the neighboring points, when they are at rest, can be magnified severalfold after deformation. As a result, while the error in the calculation of  $F_{13}$  and  $F_{23}$  is quite large for some points, one can expect a much smaller margin of error in calculation of  $G_{13}$  and  $G_{23}$  at the same points and vice versa. Thus, we may improve the strain calculation by correcting the out-of-plane deformation and strains based on a combination of  $F$  and  $G$  using the following methods.

a) Estimation of  $F_{33}$ :

The real deformation gradient matrix for an incompressible body like the myocardium has a determinant equal to unity. This makes the algebraic formula of the inverse matrices of  $F$  and  $G$  quite simple, as the  $F_{33}$  element of the matrix  $F$  can be easily estimated based on in-plane elements of matrix  $G$ :

$$F_{33} \approx (G^{-1})_{33} = \frac{\begin{vmatrix} G_{11} & G_{12} \\ G_{21} & G_{22} \end{vmatrix}}{|G|} = \begin{vmatrix} G_{11} & G_{12} \\ G_{21} & G_{22} \end{vmatrix}. \quad (3.4)$$

Also, for  $G_{33}$  we have:

$$G_{33} \approx \begin{vmatrix} F_{11} & F_{12} \\ F_{21} & F_{22} \end{vmatrix}. \quad (3.5)$$

b) Estimation of  $F_{13}$  and  $F_{23}$ :

For these two elements, we calculate the  $\partial/\partial Z$  gradients of  $x$  and  $y$ . As explained above, the error is mainly caused by the small denominator. Consequently, errors that decrease the denominator's absolute value make more changes in the estimated quantities, and on average, we end up with overestimated values for  $F_{13}$  and  $F_{23}$ , as well as for  $G_{13}$  and  $G_{23}$ . This will, in turn, result in the overestimation of the absolute values of  $E_{13}$  and  $E_{23}$ . Hence, we calculate the sum of these two latter quantities based on  $F$  and  $G$  separately. In case the calculated sum based on  $G$  is smaller, we then recalculate  $F_{13}$  and  $F_{23}$  from the orthogonality of the columns of  $F$  to rows of  $G$ , that is:

$$\sum_{k=1}^3 F_{1k} G_{k3} = 0 \Rightarrow F_{13} = -\frac{F_{11} \cdot G_{13} + F_{12} \cdot G_{23}}{G_{33}}, \quad (3.6)$$

$$\sum_{k=1}^3 F_{2k} G_{k3} = 0 \Rightarrow F_{23} = -\frac{F_{21} \cdot G_{13} + F_{22} \cdot G_{23}}{G_{33}}. \quad (3.7)$$

These two equations also guarantee that the third column of  $G$  is equal to that of the inverse of  $F$ .

### 3.2.7 Error Analysis

As explained in Section 3.2.5, the expected error in the calculation of the third column of matrices  $F$  and  $G$  ( $\delta_2$ ) is almost one order of magnitude greater than the same quantity for the first two columns ( $\delta_1$ ), even if the absolute error in the displacement measurement is constant in different coordinates. In the method suggested above, however, for the calculation of  $F_{33}$ , the expected error will be  $2\delta_1$  rather than  $\delta_2$ :

$$(G_{11} + \delta_1) \cdot (G_{22} + \delta_1) - (G_{12} + \delta_1) \cdot (G_{21} + \delta_1) \approx F_{33} + (G_{11} + G_{22})\delta_1 \approx F_{33} + 2\delta_1. \quad (3.8)$$

This approximation is derived from the fact that values of diagonal elements of matrices  $F$  and  $G$  are perturbed around unity while the other matrix elements are perturbed around zero.

For two other elements of the third column, i.e.,  $F_{13}$  and  $F_{23}$ , errors are of the higher order of  $\delta_2$ . Incorporating the errors in Equation (3.6) yields:

$$F_{13} + \delta_3 = -\frac{(F_{11} + \delta_1) \cdot (G_{13} + \delta_2) + (F_{12} + \delta_1) \cdot (G_{23} + \delta_2)}{(G_{33} + 2\delta_1)} \approx -\frac{F_{11} \cdot G_{13} + F_{12} \cdot G_{23} + (F_{11} + F_{12})\delta_2}{(G_{33} + 2\delta_1)} \quad (3.9)$$

$$\Rightarrow F_{13} + \delta_3 \approx F_{13} + \frac{\delta_2}{G_{33}} \Rightarrow \delta_3 \approx \frac{\delta_2}{G_{33}}.$$

Since the absolute value of  $G_{33}$  is around unity, this formula leads to a substitution for  $F_{13}$  with an expected error in the same order of  $\delta_2$ . Rather than the expected error, however, the actual error from this method can be much smaller than that in the direct calculation of  $F_{13}$  for some points. As explained in Section 3.2.6, the error in  $G_{13}$  and  $G_{23}$  can be several times smaller than the primary error of  $F_{13}$  and vice versa, depending on the extent of the deformation. The aim is to determine positions for which this replacement of matrix elements is useful. Considering the fact that error is usually overestimated, we apply the formula only when it decreases the sum of absolute shear for out-of-plane strains.

The aforementioned criterion resulted in the recalculation of  $F_{13}$  and  $F_{23}$  for almost 62% of the points. For these points, the average decrease in the absolute value of the out-of-plane shear strains is 0.165, while the corrected average of these strains for the same

points, after correction, is 0.425, i.e., out-of-plane shear strains of these points (62% of all points) were overestimated by 39% in comparison to the recalculated values.

According to Equation (3.2), only out-of-plane strains are affected by  $F_{i3}$ . Among them,  $E_{33}$  is affected the highest as it is calculated merely based on the third column of matrix  $F$ :

$$E_{33} = (F_{13}^2 + F_{23}^2 + F_{33}^2 - 1) / 2. \quad (3.10)$$

Therefore, the estimated error in  $E_{33}$  is:

$$\begin{aligned} E_{33} + \delta E_{33} &= \left( (F_{13} + \delta_2)^2 + (F_{23} + \delta_2)^2 + (F_{33} + 2\delta_1)^2 - 1 \right) / 2 = E_{33} + (F_{13} + F_{23})\delta_2 + \delta_2^2 + 2F_{33}\delta_1 \\ \Rightarrow \delta E_{33} &\approx (F_{13} + F_{23})\delta_2 + \delta_2^2 + 2F_{33}\delta_1 \approx (F_{13} + F_{23})\delta_2 + \delta_2^2 + 2\delta_1 \approx \delta_2 + 2\delta_1. \end{aligned} \quad (3.11)$$

$\delta E_{33}$  is thus almost two times larger than errors in  $E_{13}$  or  $E_{23}$  and its value can result in a rather significant relative error, since  $E_{33}$  does not usually have magnitudes larger than 0.25. We have attempted to solve this problem using an alternative calculation for  $E_{33}$ .

### 3.2.8 $E_{33}$ Correction

The out-of-plane strain  $E_{33}$  is estimated by approximating the thickening of the layer. Considering the two-dimensional problem, in projecting the points on the image plane, each voxel is thereby represented by a small quadrilateral on that plane. We use the in-plane elements of the deformation gradient matrix to determine the changes in the area of this quadrilateral. Calling this area  $S_1$  and  $S_2$  before and after deformation, we have:

$$\frac{S_2}{S_1} = \lambda_1 \lambda_2, \quad (3.12)$$

where  $\lambda_1$  and  $\lambda_2$  are stretch ratios of the two-dimensional deformation in the principal directions (principal strains), which are calculated as the square roots of the eigenvalues of the corresponding matrix  $C=F^T F$  in 2-D.

Accounting for the incompressibility of the myocardium, we may expect that the stretch in the third (out-of-plane) direction is calculated from  $\frac{1}{\lambda_1 \lambda_2}$  and, therefore, the strain in that direction will be  $\frac{1}{\lambda_1 \lambda_2} - 1$ . To minimize the noise, we may also take advantage of both matrices  $F$  and  $G$  in this calculation. Considering the reverse action of the anti-deformation matrix  $G$ , we estimate  $E_{33}$  using the following equation:

$$E_{33} \approx \frac{1}{2} \left( \frac{1}{\lambda_{1F} \lambda_{2F}} - \frac{1}{\lambda_{1G} \lambda_{2G}} \right), \quad (3.13)$$

where  $\lambda_{iF}$  are the stretch ratios derived from  $F$  when it is reduced to a 2 x 2 (in-plane) matrix. Similarly,  $\lambda_{iG}$  are the same quantities for the reduced matrix  $G$ .

### 3.2.9 Filtration of Strain

Although the steps mentioned earlier lead to more realistic calculated strains with a higher expectation of accuracy, they never guarantee a low noise calculation for all points. One could easily imagine that noisy displacements will survive the mild, two-step smoothing applied in the beginning and ultimately result in non-realistic strains. The crucial point to note is that we tried to increase the probability of tolerable strain calculation such that the points with acceptable strain are abundant enough to be used for the correction of strains in other points of the LV myocardium. In other words, in each

local neighborhood, we need a sufficient number of points with acceptable strains to estimate the elements of the strain tensor in that neighborhood. Since the whole process consists of several steps, its success may be only verified at the end by examining the accuracy of our calculated strains compared to other techniques.

Within the strain tensor, strains with absolute values higher than one are filtered out, since it is clear that myocardium tissue cannot have such strains physiologically. The mean and standard deviations of the strains are then calculated over the remaining points. The strains whose magnitudes are different from the calculated mean by more than 2 standard deviations are ignored. Next, in order to put the outliers aside, a five-pixel median filter is applied to the strain map. Finally, a moving average filter that acts over a  $1 \times 1 \text{ cm}^2$  area are used to fill the voids created by the ignored points and smooth the strain.

### **3.2.10 RCL strains**

Accounting for the elongated ellipsoid shape of the left ventricle, it is common that strains are usually presented in the RCL coordinate system, whose axes and vectors lie in the radial, circumferential, and longitudinal directions at any given point of the heart. Once the main long axis of the heart is known, these three directions can be defined uniquely for any point within the myocardium, including those on the epi- and endocardium. For LA slices, the determination of the RCL directions are not much affected by the position of the main long axis of the LV, apart from near the apex where these directions are not well defined. In our method, these directions are calculated automatically for every single point of the myocardium. Figure 3.3 shows these

directions before the contraction starts, i.e., at rest. Since all deformations are calculated in comparison to the position of points at this moment, the calculated directions at rest are used to express the strain tensor in RCL coordinate system for all time steps. Figure 3.3 (a) shows the longitudinal (L) directions, while (b) and (c) show the radial (R) and circumferential (C) directions. The main long axis is shown by dashed line. At each point, we express the strain tensor in its own local *RCL* coordinate system.

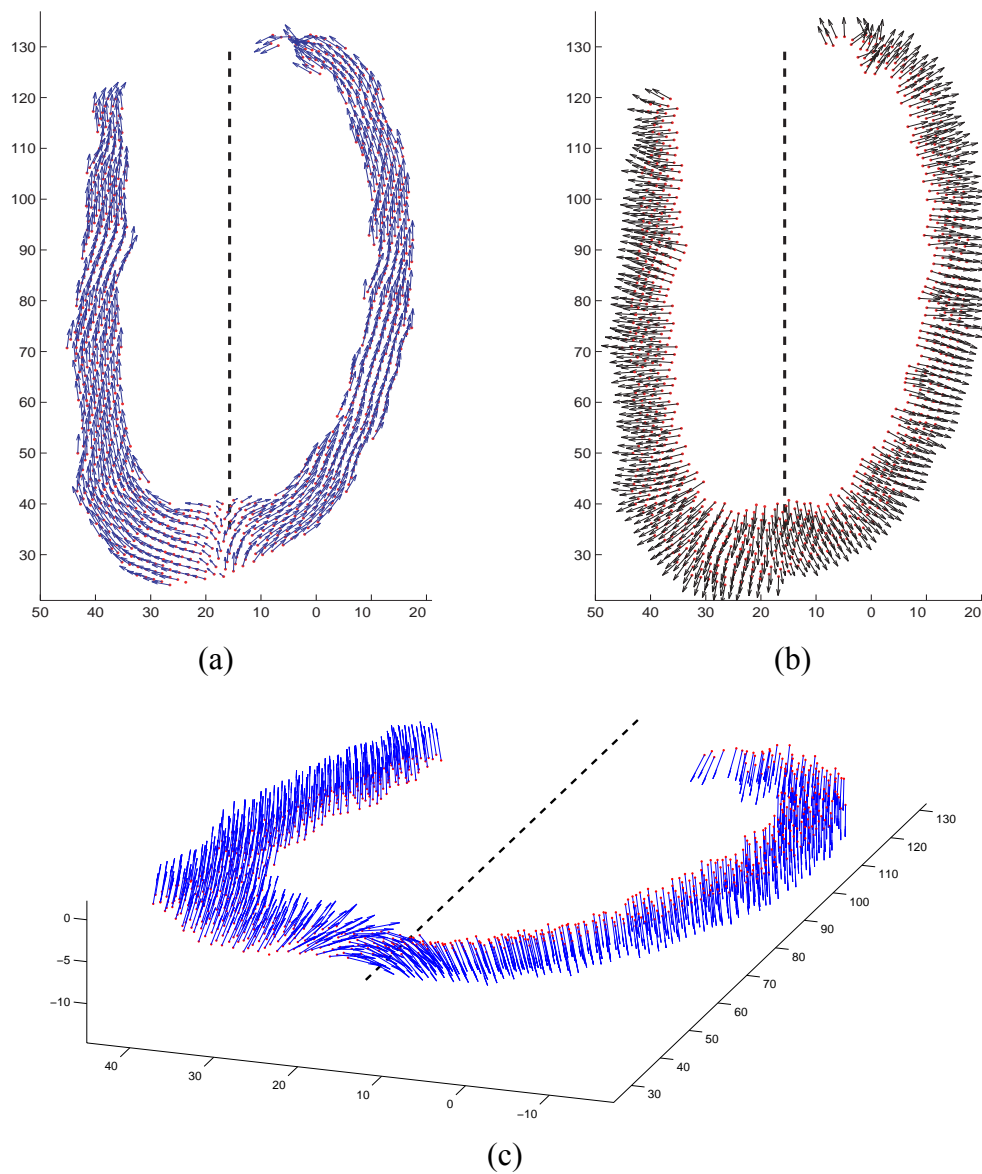


**Figure 3.3. Longitudinal (a), radial (b), and circumferential (c) unit vectors of the deformation superimposed on myocardial data points acquired via DENSE MRI.**

### 3.3 Results

Figure 3.4 illustrates the two-dimensional projection of a long-axis DENSE grid (or material) point dataset acquired at the time of maximum contraction (330ms after QRS). The points represent the positions of tissue elements at the initial acquisition time (start of systole) in the cardiac cycle. It is worth noting that unlike tagging, which provides a maximum of 3 to 4 transmural points across the myocardial wall, DENSE yields up to 7 such data points.

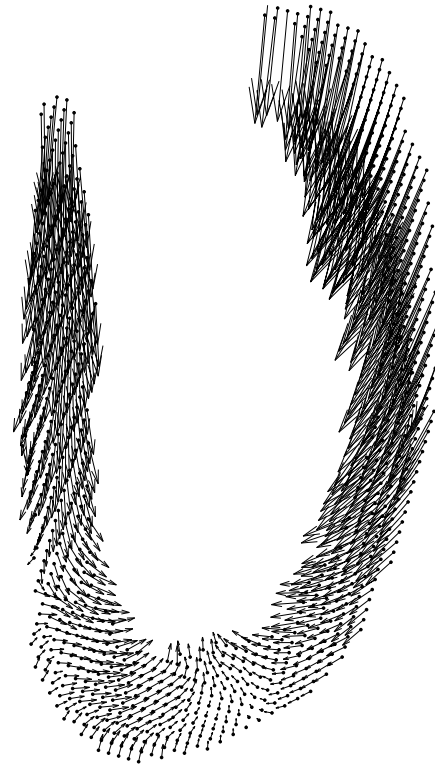


**Figure 3.4. Data acquisition points on the left ventricle wall in the MRI long-axis slice of a human heart.**

Figure 3.5 illustrates the ventricular volume curve, estimated from the two-dimensional slice as a function of time (steps). It is also apparent from this figure that the ‘resting state’ of the left ventricle, based on which the strains are calculated, is defined before contraction starts around timestep 1.

#### Comparative Study

Calculated strains are compared to those measured by Moore et al. (2000) and Young et al. (1994). Moore’s measurement is based on three-dimensional tagging dataset acquired for  $n=31$  hearts, while Young has used a three-dimensional finite element MR tagging-based model on twelve volunteers. Table 3.1 shows the peak values of  $E_{LL}$ ,  $E_{CC}$  and  $E_{RR}$  calculated in the proposed method in comparison to Moore’s and Young’s calculations

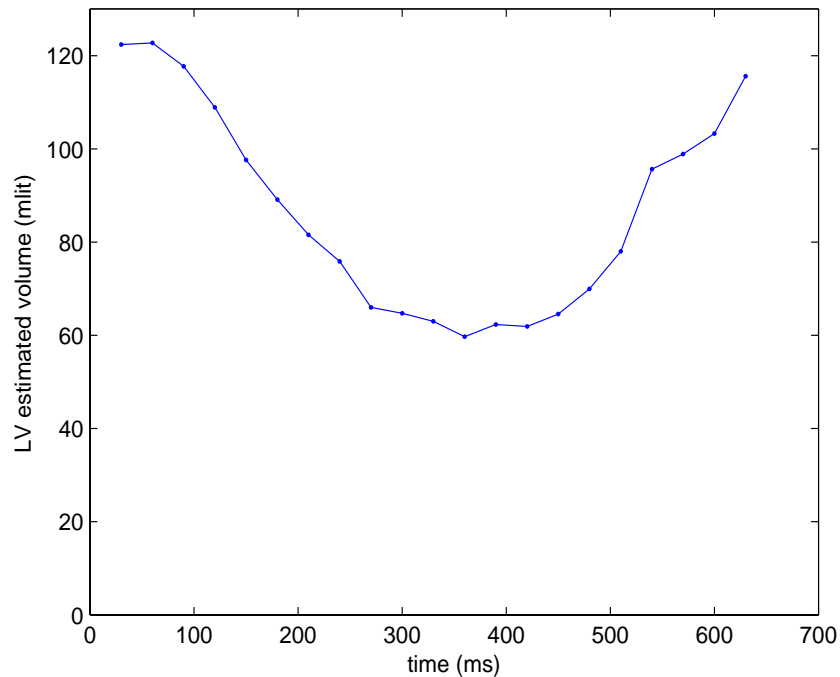


**Figure 3.5 Left ventricular volume curve as a function of time, estimated from the two-dimensional long-axis slice.**

(mean  $\pm$  standard deviation ( $\sigma$ )). This has been done over six areas on the septum and the lateral (free) wall, shown in Figure 3.6. Points in green show 30%, 55%, and 80% of the distance from the apex to the aortic valve annulus and are called apical, equatorial and basal. Elements of the strain matrix have been averaged in each of these six regions and the peak values of their means are shown in Table 3.1. Among these 18 calculations (3 quantities at 6 regions) for this single study case, only three do not fall in the range of  $[\text{mean} \pm 2\sigma]$  presented by Moore, i.e., 83.3% of our calculations is within that range which is a good agreement between the two sets of results. Differences between our results and what Moore and Young have calculated, as well as disagreements between these other two result sets are discussed in the discussion section.

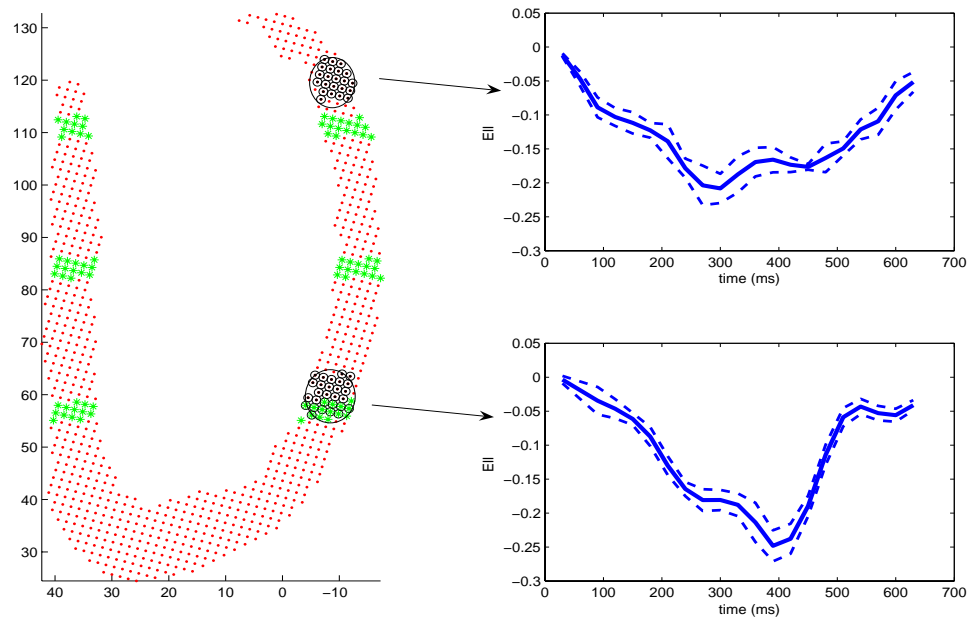


**Figure 3.6 (Left)** Tracked myocardial points on the LV; six regions determined with small stars are at 30%, 55% and 80% of the distance from the apex to the aortic valve in which the comparisons of Table 3.1 have been performed. **(Right)** Mean value of  $E_{LL}$  as a function of time, shown in two regions of the free wall; solid plots show  $E_{LL}$  averaged over the points; the dashed lines show mean  $\pm$  std over the same group of points.

**Table 3.1** The peak values of strain averaged over six regions on the septum and LV free wall as shown in Figure 3.6 compared to those reported by Moore and Young

Strain	Region	Septal Wall			Lateral (Free) Wall		
		Peak	Moore	Young	Peak	Moore	Young
$E_{LL}$	Basal	-0.10	-0.14 $\pm$ 0.03	-0.14 $\pm$ 0.03	-0.24	-0.15 $\pm$ 0.03	-0.19 $\pm$ 0.04
	Equatorial	-0.17	-0.15 $\pm$ 0.03	-0.15 $\pm$ 0.02	-0.19	-0.14 $\pm$ 0.04	-0.16 $\pm$ 0.03
	Apical	-0.18	-0.18 $\pm$ 0.04	-0.19 $\pm$ 0.02	-0.24	-0.19 $\pm$ 0.03	-0.18 $\pm$ 0.03
$E_{CC}$	Basal	-0.16	-0.17 $\pm$ 0.03	-0.19 $\pm$ 0.03	-0.22	-0.21 $\pm$ 0.03	-0.21 $\pm$ 0.03
	Equatorial	-0.14	-0.16 $\pm$ 0.03	-0.20 $\pm$ 0.02	-0.18	-0.22 $\pm$ 0.03	-0.21 $\pm$ 0.02
	Apical	-0.28	-0.18 $\pm$ 0.03	-0.20 $\pm$ 0.03	-0.14	-0.24 $\pm$ 0.04	-0.22 $\pm$ 0.02
$E_{RR}$	Basal	0.39	0.45 $\pm$ 0.12	0.21 $\pm$ 0.10	0.64	0.52 $\pm$ 0.19	0.25 $\pm$ 0.09
	Equatorial	0.49	0.42 $\pm$ 0.19	0.16 $\pm$ 0.10	0.53	0.38 $\pm$ 0.18	0.21 $\pm$ 0.10
	Apical	0.58	0.36 $\pm$ 0.22	0.07 $\pm$ 0.06	0.59	0.49 $\pm$ 0.29	0.10 $\pm$ 0.06

Table 3.2 shows the shear strains for the same six regions at the time of maximum deformation, i.e., 360 ms after the R wave, compared to Moore's calculations. Comparing the results of our single study to those of Moore, three out of eighteen calculated shear strains do not fall in the range of  $[\text{mean} \pm 2\sigma]$  presented by Moore and 50% are in the  $[\text{mean} \pm \sigma]$  interval. These results will be discussed later in more detail in the discussion section. At this point, we have demonstrated that our results fall in the acceptable range.

Besides the peak strain values, the temporal changes of the strains can also be important, as they can reveal details of the cardiac function. For instance, the mean value of  $E_{LL}$  as a function of time is shown at two regions of the free wall in Figure 3.6. This figure illustrates that although the contraction profiles are almost similar in the base and apex in the first 250 ms of the cycle, the peak strain at the apex happens at a later time (400 ms) and the strain decreases in magnitude rapidly afterward.

**Table 3.2** The peak values of shear strain averaged over six regions on the septum and LV free wall as shown in Figure 3.6 compared to those reported by Moore

Strain	Region	Septal Wall			Lateral (Free) Wall		
		Peak	Moore	Variation Coef. (%)	Peak	Moore	Variation Coef. (%)
$E_{LC}$	Basal	0.02	0.01±0.05	500	0.00	0.03±0.05	166
	Equatorial	-0.09	0.03±0.05	160	0.07	0.03±0.04	133
	Apical	0.11	0.04±0.05	125	0.00	0.04±0.03	75
$E_{LR}$	Basal	-0.02	0.03±0.09	300	-0.04	0.05±0.07	140
	Equatorial	-0.06	0.08±0.05	62.5	-0.01	0.07±0.06	85.7
	Apical	0.05	0.06±0.09	150	-0.02	0.05±0.08	160
$E_{RC}$	Basal	0.19	0.01±0.06	600	-0.09	0.05±0.07	140
	Equatorial	-0.10	0.02±0.08	400	-0.03	0.05±0.06	120
	Apical	0.03	0.11±0.10	91	0.08	0.05±0.08	160

Figure 3.7 shows the distribution of all six elements of strain at peak systole ( $t = 360$  ms) and Figure 3.8 shows the map of out-of-plane strain ( $E_{CC}$ ) during systole and most of diastole, i.e., 18 frames in total.

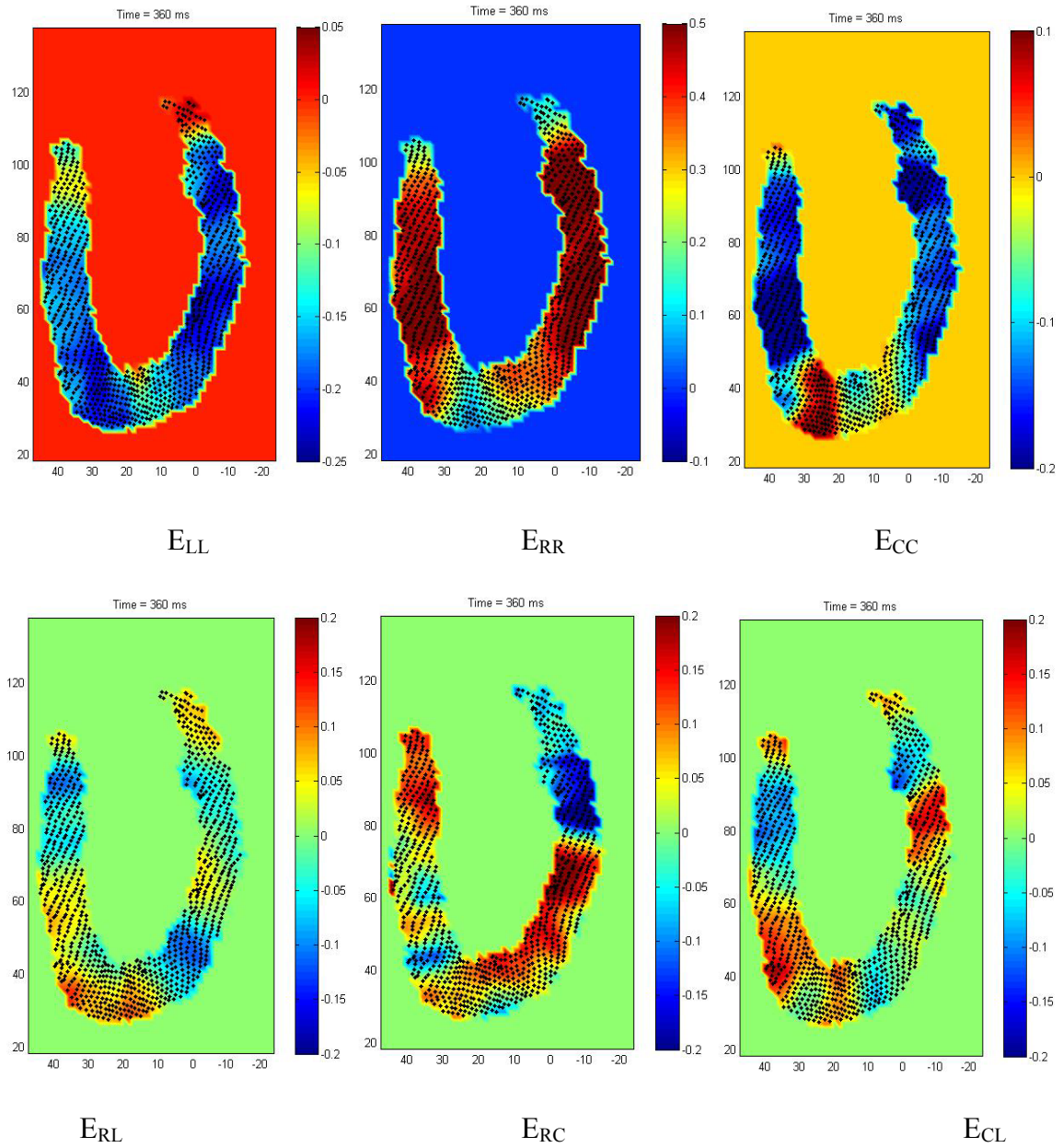


**Figure 3.7. Distribution of all six elements of the strain matrix at peak systole ( $t = 360$  ms).**

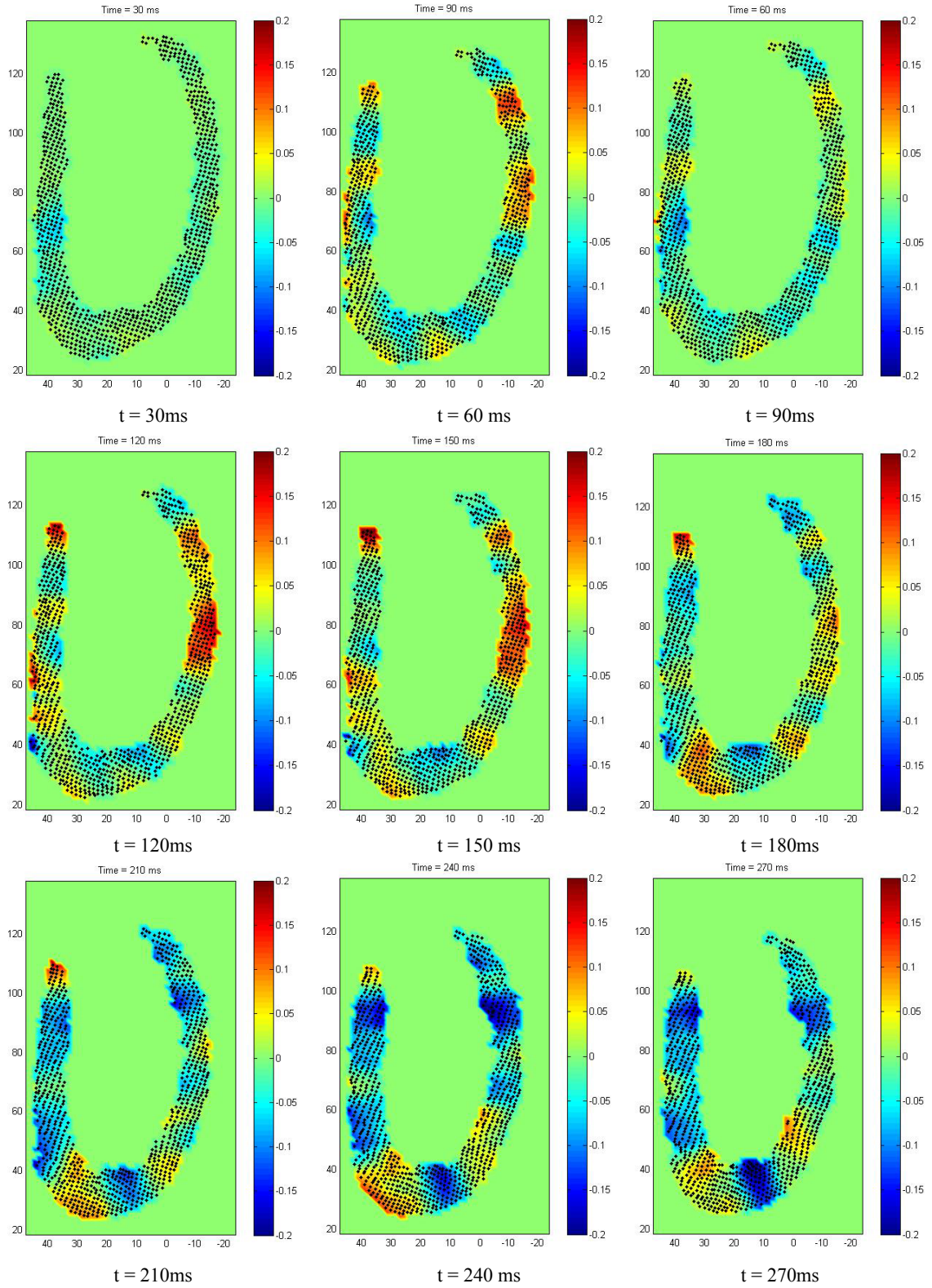


**Figure 3.8** Map of out-of-plane strain ( $E_{cc}$ ) during systole and most of diastole (18 frames in total; Continued on the next page).

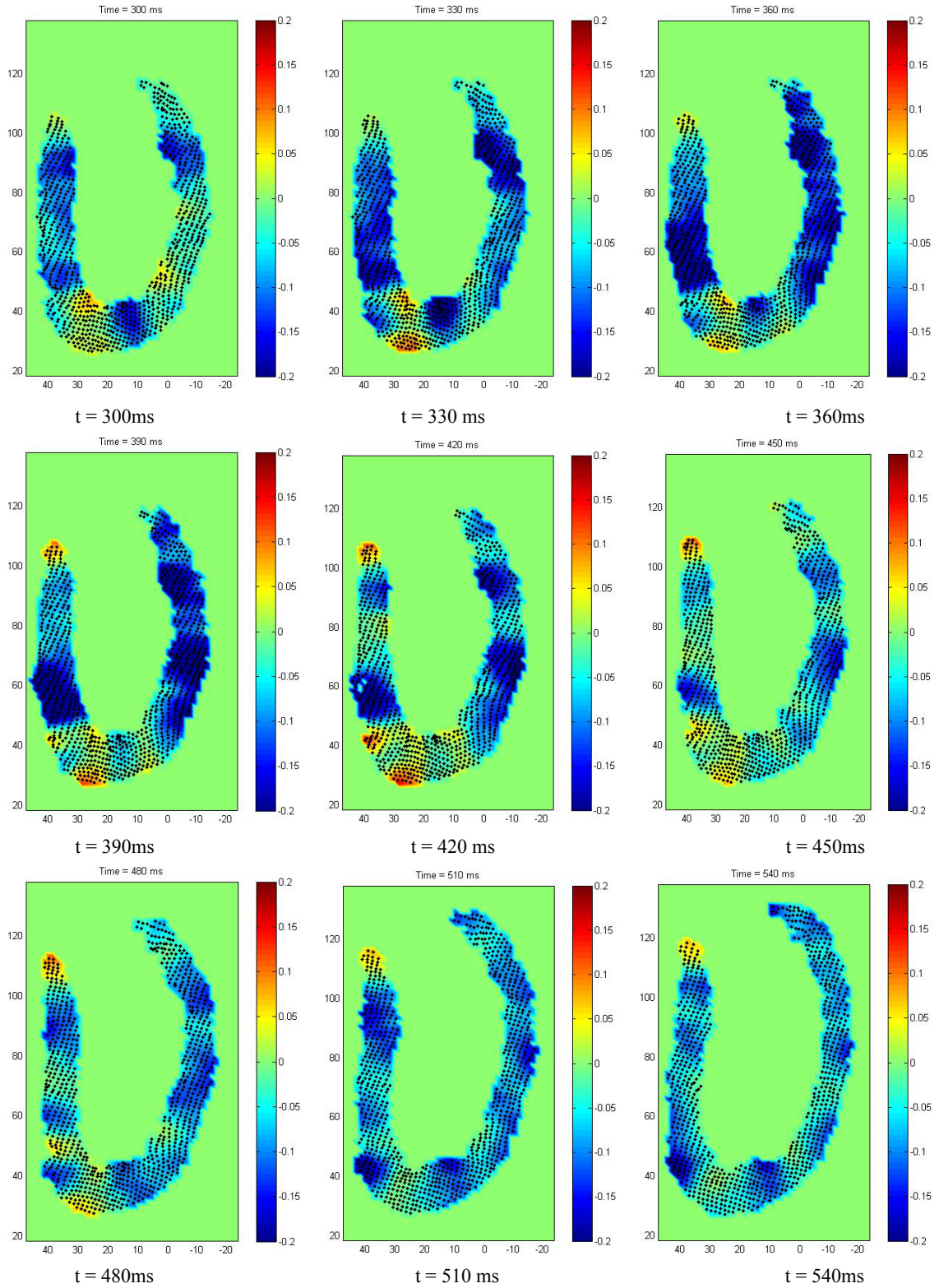


Figure 3.8 (Continue from the previous page).

### 3.4 Discussion

In order to validate our results, we compare them to those of Moore (2000) and Young (1994). Young's calculation of the average  $E_{RR}$  in different regions of the heart wall varies from 0.07 to 0.25, while the same range for Moore is quoted as 0.36 to 0.52. For other normal strain elements, however, i.e.,  $E_{LL}$  and  $E_{CC}$ , their results are in much better agreement. It should also be noted that Moore's calculation of  $E_{RR}$  seems to be more in line with available physiological data (60% ejection fraction) and clinical evidence (Taratorin and Sideman 1995; Lessick, Fisher et al. 1996). For the validation of  $E_{RR}$ , therefore, we focus solely on Moore's calculation, which shows great agreement with our results, i.e., all our six calculations for  $E_{RR}$  are in the range of  $[\text{mean} \pm \sigma]$  (rather than  $2\sigma$ ).

In comparing our results to those of Moore and Young, it becomes apparent that, in general, 83.3% of our strain results in this single-case study fall in their quoted range of  $[\text{mean} \pm 2\sigma]$  ( $E_{RR}$  of Young's calculation was ignored). The highest discrepancy occurred in the case of  $E_{CC}$ , for which only 66.6% fell in the range of  $[\text{mean} \pm 2\sigma]$  as listed by Moore and Young. As explained in previous sections, this was not unexpected. A possible explanation for the observed discrepancy is the averaging of the strains over regions of the myocardial wall. For example, the peak value of apical  $E_{CC}$  on the free wall, calculated by our method, is shown as -0.14 in the table; however, if we only focus on the epicardium, this value is -0.17 which no longer falls out of range. Another disagreement is that the peak value of apical  $E_{CC}$  on the septum is overestimated, that is, -0.27 in comparison to  $-0.18 \pm 0.03$  of Moore and  $-0.20 \pm 0.03$  of Young. Nevertheless,

according to our results, this value drops very rapidly in the course of time, and if we had a lower temporal resolution, this peak would not be observed. In other words, it could be a sharp peak which is missed by the different time steps in the tagging images used in Moore and Young's respective studies.

We did not include Young's calculations for shear strain in Table 3.2, since 22.2% of the shear strain means calculated by Moore fall out of the  $[\text{mean} \pm 2\sigma]$  interval presented by Young for the same quantities, while only 55.6% of these fall within the  $[\text{mean} \pm \sigma]$  interval. One reason for this discrepancy is that in Young's calculation, the region of interest is much larger than the one chosen in Moore's study as well as ours.

For shear strains, the agreement of our results with Moore's is acceptable, although a little less so for normal strains. To explain this discrepancy, we should note that the variation coefficients ( $\sigma/\text{mean}$ ) of shear strains are in the range of 62.5% to 600% (average: 200%) in Moore's calculations. These huge variations show either a high inter-subject variability or a large error margin. Regardless of the reason, using Moore's or Young's result set as a gold standard should therefore be practiced with caution.

Lessick et al. (1996) observed increasing gradients of thickening from base to apex. Our method shows this clearly on the septal wall through the increase in  $E_{RR}$ , whereas Moore's results do not show this pattern on either wall. Nonetheless, it is worth noting that our case study used only a single slice of the heart.

Another aspect to consider is the disagreement between the results presented by Moore and Young. For instance, their calculations for  $E_{CC}$  on the septal wall are different by 10% - 25%. Nonetheless, it should be noted that our case study used only a single slice of

the heart. Overall, it seems that our methods yield an acceptable estimation of the strain for in- and out-of-plane strains.

Finally, it should be noted that the results in the region very close to the apex suffer from the fact that RCL directions there could not be well defined. This fact imposes some problems when all values are transformed to that coordinate system.

A source of error in our method could be that we assume the heart function is completely periodic, meaning all the myocardial points follow a perfect periodic path and are in their initial location at the time of data acquisition. This assumption is not sufficiently accurate and may result in errors.

### **3.5 Chapter Conclusion**

We have demonstrated that our methods are able to calculate three-dimensional systolic and diastolic strain patterns in the left ventricle with high spatio-temporal resolution from a single-slice DENSE MRI dataset. The feasibility of obtaining very favorable spatio-temporal resolution for tissue tracking by DENSE MRI from human subjects has also been shown. Finally, we have illustrated the feasibility, and then validated the calculation of, all six elements of the myocardial strain matrix ( $E$ ) from a single slice with three-dimensional motion. As mentioned before, the methods developed in this study are general and can be used with other data acquisition techniques such as zHARP. Our work provides a framework for the detailed analysis of cardiac deformation and contraction (physiology), both in time and space. For example, we are able to demonstrate various functional behaviors of the heart wall, such as asymmetry of strains and non-uniform contraction patterns within the ventricle wall.

In conclusion, results similar to those shown here provide implications for cardiac function, enable us to determine characteristic indices for normal hearts and to quantify focal regions of abnormal contraction in diseased hearts, namely diastolic dysfunction and dilated cardiomyopathy, and will prospectively have an impact on patient diagnosis and clinical treatment in the future.

### 3.6 Chapter References

- Abd-Elmoniem, K. Z., M. Stuber, N. F. Osman, and J. L. Prince, "ZHARP: Three-dimensional motion tracking from a single image plane," in *Information Processing in Medical Imaging*, Berlin: Springer, 2005, PP. 639 - 651.
- Aletras, A. H., S. Ding, et al. (1999). "DENSE: displacement encoding with stimulated echoes in cardiac functional MRI." *J Magn Reson* **137**(1): 247-52.
- Aletras, H. Wen, R. Y. Kwong, and A. E. Arai, "Strain analysis of human MI using dual-echo DENSE: An automated quantitative MRI method. *Circulation* 102(18):2368, 2000.
- Axel, L. and L. Dougherty (1989). "MR imaging of motion with spatial modulation of magnetization." *Radiology* **171**(3): 841-5.
- Bryant, D. J., J. A. Payne, et al. (1984). "Measurement of flow with NMR imaging using a gradient pulse and phase difference technique." *J Comput Assist Tomogr* **8**(4): 588-93.
- Gilson, W. D., Y. Q. Yang, B. A. French, and F. H. Epstein, "Gadolinium-enhanced displacement-encoded MRI can simultaneously image infarct area and myocardial function in mice," *Circulation* 106(19):2168, 2002.
- Humphrey, J. D., *Cardiovascular Solid Mechanics: Cells, Tissues, and Organs*. New York: Springer-Verlag, 2002.
- Kim, D., W. D. Gilson, et al. (2004). "Myocardial tissue tracking with two-dimensional cine displacement-encoded MR imaging: development and initial evaluation." *Radiology* **230**(3): 862-71.
- Lessick, J., Y. Fisher, et al. (1996). "Regional three-dimensional geometry of the normal human left ventricle using cine computed tomography." *Ann Biomed Eng* **24**(5): 583-94.
- Meyer, F. G., R. T. Constable, A. J. Sinusas, and J. S. Duncan, "Dense nongrid motion tracking from a sequence of velocity fields," in *Proc. of the IEEE Conference on Computer Vision and Pattern Recognition*, San Francisco, 1996, p. 839.
- Moore, C. C., C. H. Lugo-Olivieri, et al. (2000). "Three-dimensional systolic strain patterns in the normal human left ventricle: characterization with tagged MR imaging." *Radiology* **214**(2): 453-66.
- Osman, N. F., W. S. Kerwin, et al. (1999). "Cardiac motion tracking using CINE harmonic phase (HARP) magnetic resonance imaging." *Magn Reson Med* **42**(6): 1048-60.
- Parmley, W. W., L. Talbot, "Heart as a pump," In: *Handbook of Physiology: Section 2: The Cardiovascular System, Volume 1: The Heart*, volume Edited by R. M. Berne, Bethesda, MD: American Physiological Society, 1979, pp. 429-460.
- Pelc, L. R., J. Sayre, et al. (1994). "Evaluation of myocardial motion tracking with cine-phase contrast magnetic resonance imaging." *Invest Radiol* **29**(12): 1038-42.
- Pelc, N. J., M. Drangova, et al. (1995). "Tracking of cyclic motion with phase-contrast cine MR velocity data." *J Magn Reson Imaging* **5**(3): 339-45.
- Ratcliffe, M. B., K. B. Gupta, et al. (1995). "Use of sonomicrometry and multidimensional scaling to determine the three-dimensional coordinates of multiple cardiac locations: feasibility and initial implementation." *IEEE Trans Biomed Eng* **42**(6): 587-98.

- Stuber, M., M. A. Spiegel, et al. (1999). "Single breath-hold slice-following CSPAMM myocardial tagging." Magma **9**(1-2): 85-91.
- Taratorin, A. M. and S. Sideman (1995). "3D functional mapping of left ventricular dynamics." Comput Med Imaging Graph **19**(1): 113-29.
- Van Dijk, P. (1984). "Direct cardiac NMR imaging of heart wall and blood flow velocity." J Comput Assist Tomogr **8**(3): 429-36.
- Wen, H. and E. Bennett, (2004). "In vivo measurement of the elasticity and internal viscous damping constant of the myocardium in diastole," J. Cardiovascular Magnetic Resonance, **6**(1): 366-8.
- Wen, H., E. Bennett, et al. (2005). "Magnetic resonance imaging assessment of myocardial elastic modulus and viscosity using displacement imaging and phase-contrast velocity mapping." Magn Reson Med **54**(3): 538-48.
- Young, A. A. "Epicardial deformations from coronary cine angiograms," In: *Theory of heart: biomechanics, biophysics, and nonlinear dynamics of cardiac function*, Edited by L. Glass L, P. Hunter, and A. McCulloch, New York: Springer-Verlag, 1991, pp. 175-207.
- Young, A. A., C. M. Kramer, et al. (1994). "Three-dimensional left ventricular deformation in hypertrophic cardiomyopathy." Circulation **90**(2): 854-67.
- Zerhouni, E. A., D. M. Parish, et al. (1988). "Human heart: tagging with MR imaging-a method for noninvasive assessment of myocardial motion." Radiology **169**(1): 59-63.

## CHAPTER 4

### Macro-structure of the heart

#### 4.0 Abstract

The importance of considering the macro-structure of the myocardium is discussed and an approach to define this structure is proposed based on the spatial distribution of the heart regional function. This local function, which determines the regional contribution of the myocardium in pumping the blood, is quantified in LV by shortening index,  $SI$ , and wall thickening  $WT$ , as characteristic parameters. These parameters were calculated using advanced MRI techniques that measure the myocardium displacement. We showed how regions with a higher degree of contractile function may form a macro-structure for the LV. The existence of such a band-shaped structure is emphasized by histological evidences and its compatibility with micro-structural organization of the fibers is shown.

#### 4.1 Introduction

The heart function may be investigated at the molecular level by studying the actin-myosin proteins in the muscle fibers (Davis, Hassanzadeh et al. 2001, 2002). The function of these proteins is to generate a contraction force along the fibers. Each fiber generates a force tangent to itself, however in any given location their resultant force might be directed in another direction because of the transmural variation of the fiber directions (Streeter, Spotnitz et al. 1969). This effect can be illustrated by considering a rope when it is pulled along its length. The fibers in the rope are not necessarily aligned in the axial (pulling) direction. In a similar fashion, we propose to look for macro-structure in the myocardium based on its role as a pathway for the transmission of contractile force. If such a structure exists, knowledge of its normal morphology and

function may open a new horizon for better diagnosis strategies, evaluation, modeling, and treatment of heart disease. The goal of this research is to investigate the existence of such a structure through the imaging of the heart kinematics.

We define the dominant macro-structure of the myocardium as the pathway that is determined based on the local contractile behavior of the myocardium. The first required step in determining the heart's macro-structure is to define the *regional* contractile functionality as oppose to the global function of the heart. In other words, the contribution of each region of the heart in the entire pumping process should be characterized with some measurable factor. The next step is to calculate this characteristic factor for all points in the ventricle wall and discover locations with larger contribution to the overall functionality. The effectiveness of this approach depends on the proper identification of the cardiac regions that exhibit higher contractile activity and the nature of their linkage and inner connectivity.

#### **4.2 Wall Thickening**

The regional functionality of the left ventricle (LV) is important for the evaluation of dysfunctional myocardial regions. In this respect a regional ejection fraction (EF) can be define by calculating the myocardium area in the short axis images of the LV at the end of systole and diastole (Lapeyre, Klodas et al. 2005). For this approach to work, LV needs to be segmented and the center axis of the LV tracked during the cardiac cycle. Tracking the center axis of the LV is a challenge in this method.

The wall thickening (WT) and the wall motion (WM) are two other representative factors for evaluating the LV regional activity (Fujii, Ohashi et al. 2005). The WT has shown

some advantages over WM in applications such as the evaluation of postoperative cardiac function (Taki, Higuchi et al. 2002).

During the last twenty years, MRI has been used to determine both WT and WM (Sechtem, Sommerhoff et al. 1987), but the early applications were mainly based on the measurements over cine magnitude images and therefore were not accurate. When MR strain imaging methods such as tagging were developed, however, the local strain analysis showed its superiority to the previous planar WT analysis in the differentiation of normal and dyskinetic regions (Gotte, van Rossum et al. 2001). Furthermore, these new techniques also improved WT measurement methods. By using tagging, along with more precise measures of the WT, Moore et al. showed that the contraction indices and WT had better accuracy and tighter normal ranges than the calculated strain components (2000).

In this study, using DENSE MRI as the main imaging method, we extended the Moore et al. method to show the transmural changes of WT across the wall. We then used the map of WT and a related index, i.e., *SI*, to find the macro-structure of the LV.

### **4.3 Importance of WT & *SI***

The adult heart is a positive displacement pump which has an almost constant external volume. The EF as the ratio of the stroke volume to the end diastolic volume, is almost 60% in a normal human LV (Guyton and Hall 2000), while the contraction of myofibers falls in the range of 12% to 15%. If this contraction only generated a longitudinal shortening in the LV, as shown schematically in Figure 4.1 using a prolate spheroidal coordinate system, then it would result in an EF of about 15%. This reveals the

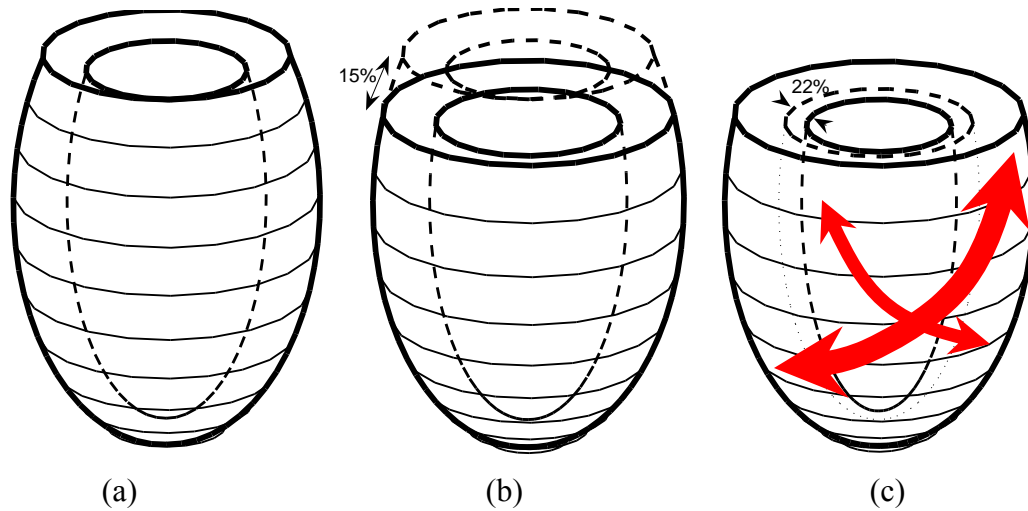


**Figure 4.1** The model of the LV (a) at end diastole, (b) with only longitudinal contraction and (c) with wall thickening in addition to shortening.

importance of the wall thickening, since in this schematic, a WT of 22% guarantees not only the incompressibility of the myocardium muscle but also a realistic EF of about 60%. These numbers are only quoted to give an idea of the importance of WT. In a real physiological case, the typical thickening of the heart wall is usually higher than 40% (Moore, Lugo-Olivieri et al. 2000).

It is important to note that the wall thickening is not determined solely by the incompressibility of the myocardium. In the schematic of Figure 4.1, if the LV could dilate circumferentially, a WT of 10% would satisfy the incompressibility but results in only 15% EF (Fig. 4.2). This demonstrates how crucial the circumferential lengthening could be to the heart's operation. The experimental results also reinforce this logic. Figure 4.3 illustrates the longitudinal as well as circumferential tensile strains in a long axis slice of the heart at end systole, and it shows that at end systole, all points along the wall are contracted circumferentially as well as longitudinally (see Chapter 3 for more details).

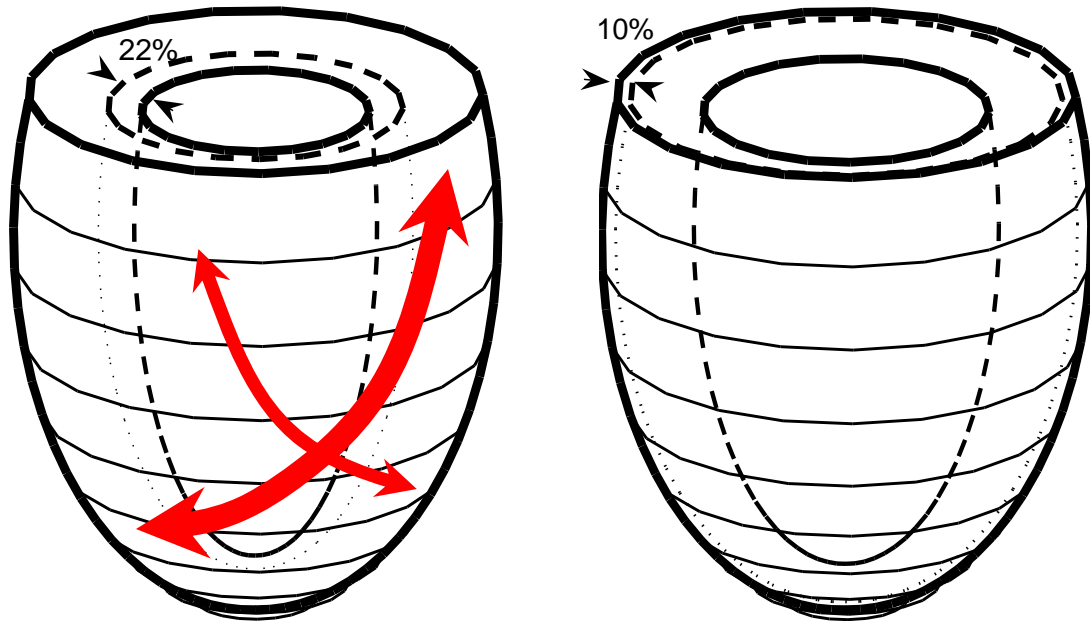


**Figure 4.2.** The conservation of mass may be satisfied in many different ways. In this schematic contraction in the endocardium (left) has been compared to the dilation of the epicardium (right). The amount of WT is quite different in these two cases.

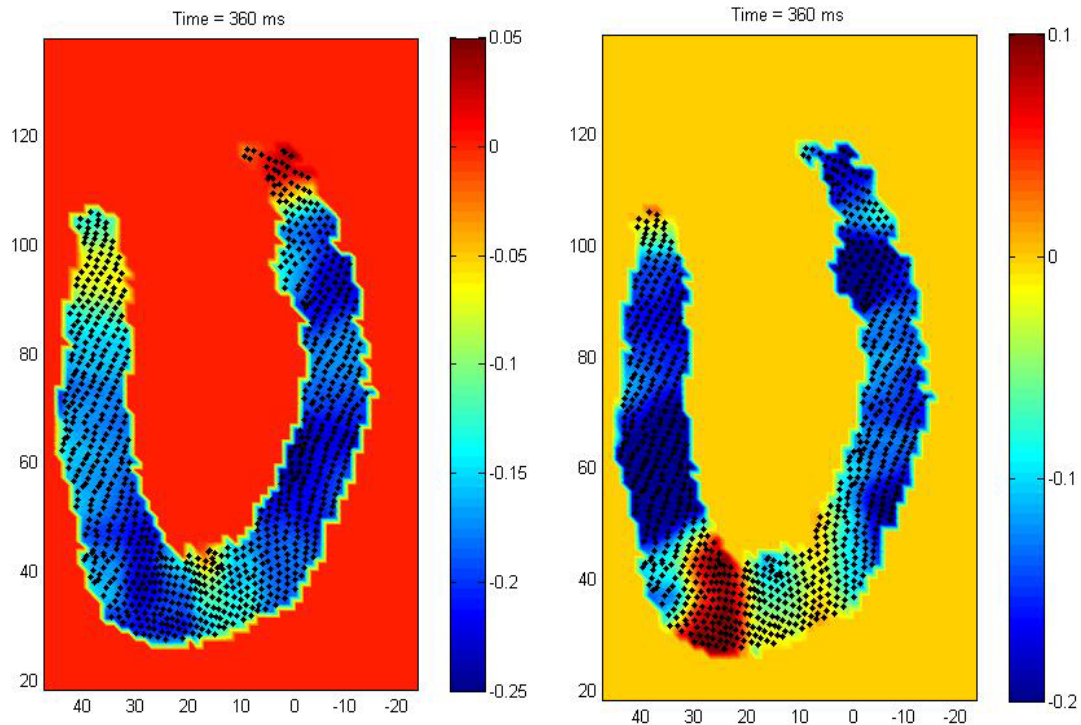


**Figure 4.3.** Longitudinal (left) and circumferential (right) tensile strains at end systole in a normal human LV. The values near the apex is not reliable because of the ambiguity of RLC unit vectors at this region. Both tensile strains are negative.

The macroscopic structure, therefore, should be in the form of two intersecting bands to ensure the existence of tangential shortening in the LV and create a contraction in both directions. A spiral pathway is the most probable way to unify these intersecting bands. Thus, we may expect the main axes of contraction to be in the form of arrows shown in the schematic (c) of Figure 4.1. There is a good evidence for these logical conjectures from MR strain measurements. Moore et al. have shown that the principal strains of the LV wall during the shortening phase are directed in these two speculated directions (2000).

At the microstructure level, the tangential shortening is guaranteed by transmural changes of the fiber directions from left-hand twist at the epicardium to right-hand twist at the endocardium (Streeter, Spotnitz et al. 1969). Recent statistical investigations through three-dimensional diffusion-weighted MRI have shown that in the anisotropic regions of the LV, fibers have two consistent and dominant orientations, approximately  $45^\circ$  and  $117^\circ$  (Helm, Tseng et al. 2005). These results, which are supported by previous histological studies (Dokos, Smaill et al. 2002), may connect the microstructure with the suggested macro-structure.

Moore et al. have suggested a scalar quantity to measure the tangential shortening in a manner which is not sensitive to the in-plane deformation (2000). This quantity, known as the shortening index ( $SI$ ), measures the change of the in-plane area based on the stretch tensor  $U$ , in the radial, longitudinal and circumferential (RLC) coordinate system, is calculated as:

$$SI = \sqrt{\left| (U_{RC}, U_{CC}, U_{LC}) \times (U_{RL}, U_{CL}, U_{LL}) \right|} - 1 . \quad (4.1)$$

Furthermore they showed that, considering the incompressibility of the myocardium, the thickening of the wall is also calculated by elements of  $U$ :

$$T = \frac{1 + U_{RC}(U_{CR}U_{LL} - U_{CL}U_{LR}) - U_{RL}(U_{CR}U_{LC} - U_{CC}U_{LR})}{U_{CC}U_{LL} - U_{CL}U_{LC}} - 1, \quad (4.2)$$

where  $T$  and  $SI$  can be measured at any point inside the heart muscle.

Considering that the functionality of the LV comes from wall thickening and its tangential shortening, these two dependent scalar quantities can be used as the quantitative characteristics for the LV's regional functionality. We calculated the maps of  $T$  and  $SI$  with high spatial resolution based on the maximum deformation of the LV, i.e., from the enddiastole to the endsystole. The macro-structure of the LV was subsequently sought by calculation and comparison of the isosurfaces of these quantities for their relatively higher absolute values.

#### 4.4 Experimental methods

DENSE MRI has been used to measure the displacements of the heart muscle points. Advantages of this imaging method were discussed in the previous chapter. For this study, particle tracking was performed on ten short-axis (SA) images captured from the heart of a 36-year-old male volunteer. Experiments were performed in a Siemens Trio 3T MR whole-body scanner at the Caltech brain imaging center with an eight-channel cardiac array coil. The parameters are, TR = 3.1 ms, TM = 250 ms, number of averages = 3, number of phases = 3, in-plane resolution = 1.5mm x 1.5mm. Slice thickness of the SA images is 5mm, while they were spaced every 7.5 mm. The experiment was performed under free respiration condition. To synchronize the RF pulses with the

motion of the heart and chest, respiratory and heart monitoring were achieved using a pneumatic bellows and ECG. The displacement field was smoothed by a moving average filtering. We captured the positions of the designated muscle volume elements at 4 equally spaced times, where the first and last positions correspond to the end diastole and end systole in the heart cardiac cycle. A similar study was conducted on a 2-year-old male volunteer to capture the displacement on 8 SA slices which were separated every 12 mm. The voxel size in the second study was 1.7mm x 1.7mm x 6 mm.

#### 4.5 Results

The measured displacement field for the first volunteer is shown in Figure 4.4. Some long-axis (LA) slices were also added to make a better three-dimensional perception. This LA information may be used for interpolation of the displacement data (see appendix D), however, they have not been used in this study.

Similar results are shown in Figure 4.5 for the second volunteer where the short axis images are not perpendicular to the main axis of the LV. These displacement fields may be used for calculation of the global, as well as local, quantitative factors of the LV like EF, torsion, and strain maps. Due to the scope of this study, we focus on the  $SI$  and  $T$  defined above. Using the methods previously discussed, we calculated the deformation gradient tensor  $F$ , the right stretch tensor  $U$  in the  $RLC$  coordinate system, and, finally  $SI$  and  $T$  using equations (4.1) and (4.2). Having these values for all imaged pixels, their volumetric iso-surfaces then were calculated by the Matlab software.

For visualization purposes, we set a threshold for the absolute value of these quantities, such that material points with  $SI$  (or  $T$ ) below that threshold were removed from the

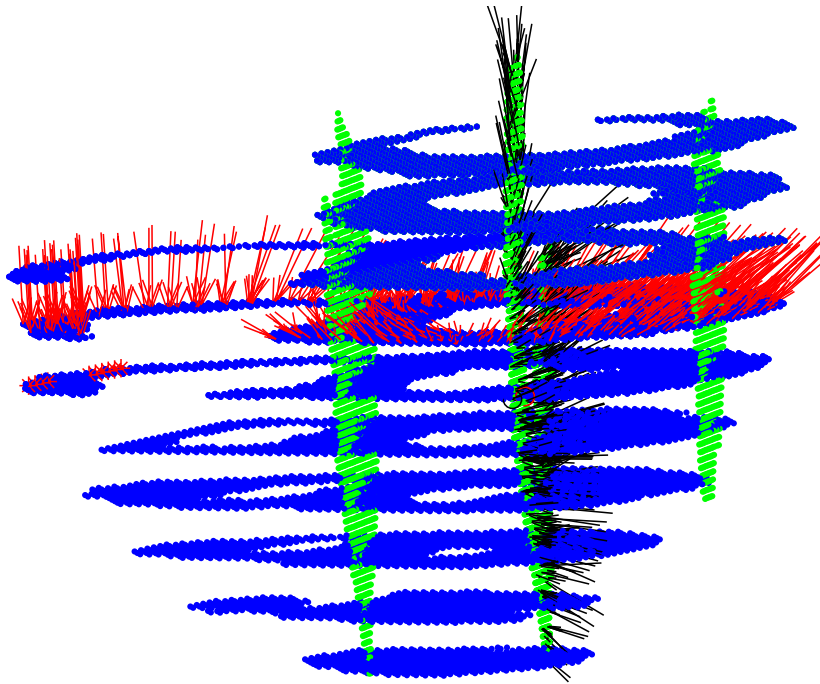


**Figure 4.4 The displacement field from DENSE for 10 SA slices and 3 LA slices of the heart (case one).**

solution domain. We increased this threshold uniformly until the disconnection of the remaining regions started. Figure 4.6 shows the results of this procedure for the calculated  $SI$  in the first case from different view points. We observed from the two datasets acquired from human subjects that contraction strength is not uniformly distributed in the LV, rather it is wrapped around the heart like a band. This band starts from the superior-anterior section of the LV, goes down to its inferior posterior through the LV free wall, rotates around the apex and finally arrives at the septum. The other side of the contraction band initiates from the superior-posterior of the heart and through the LV free wall reaches the septum and becomes connected to the other part. Despite minor differences that might be caused by noise, the overall patterns look similar in both studies. Results for the second study are presented in Figure 4.7.

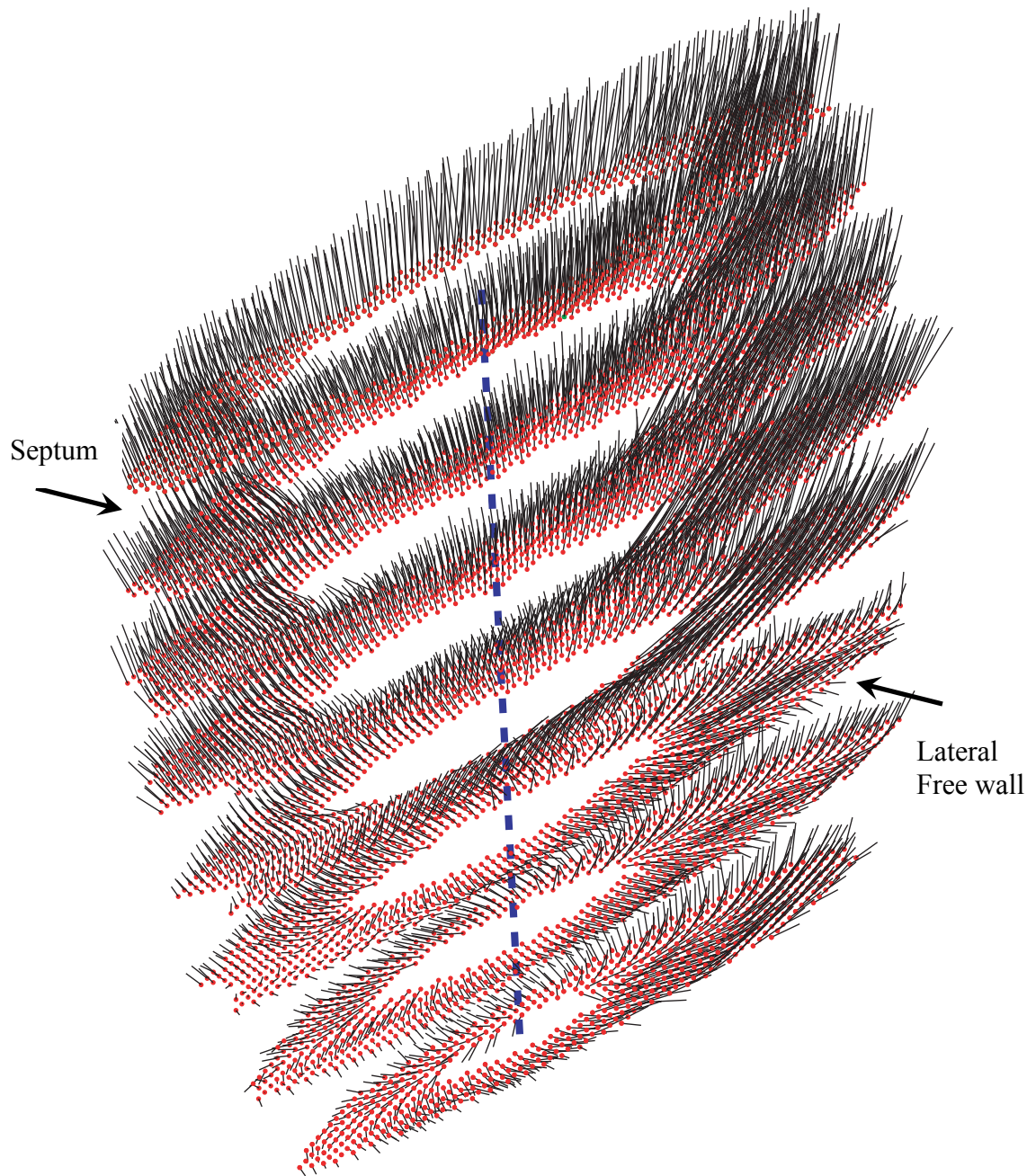


**Figure 4.5** Displacement field of the left ventricle for another heart (case two). The SA slices are not perpendicular to the main axis of the heart (dashed line). Free wall and septum are determined.

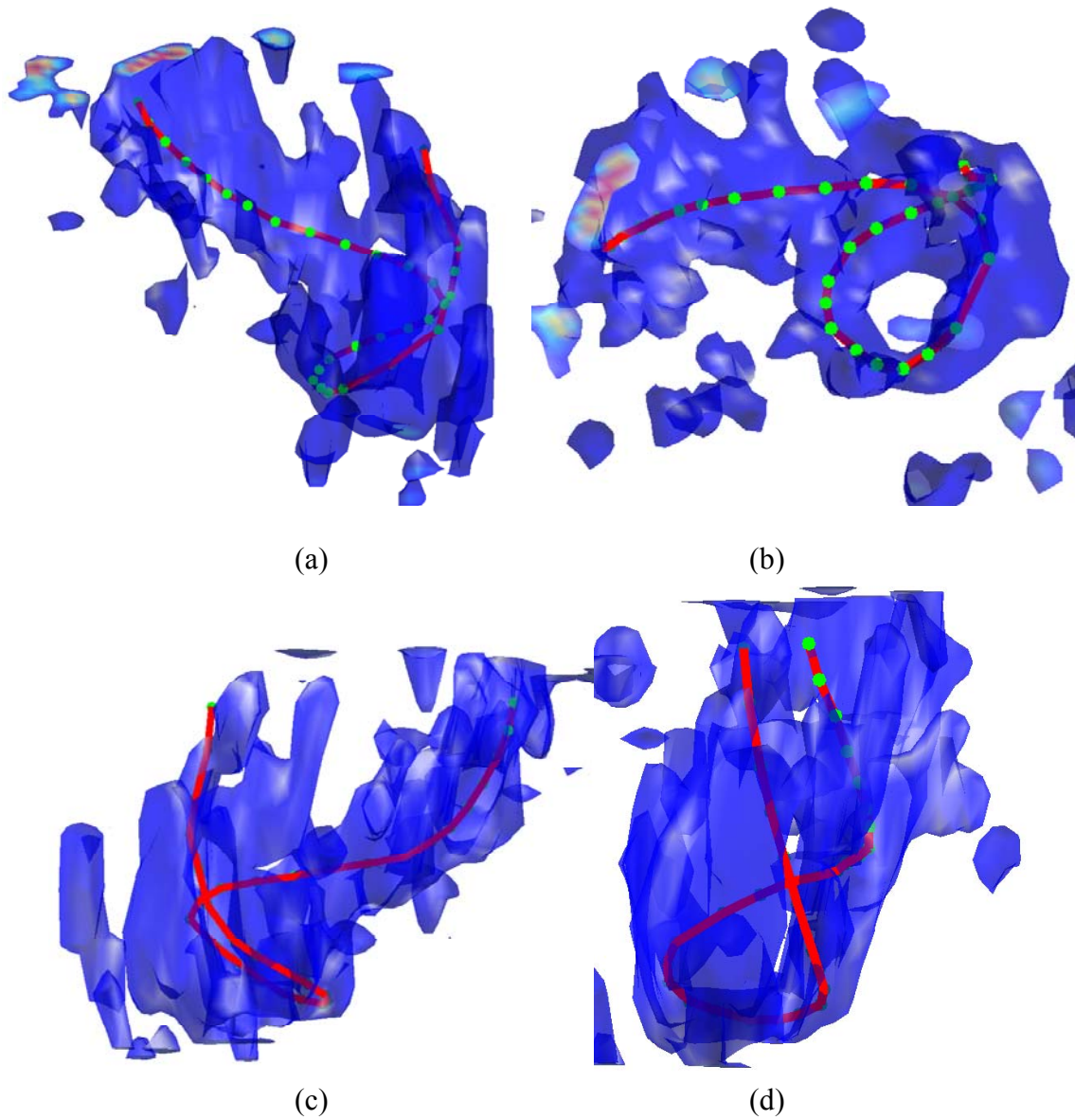


**Figure 4.6** calculated isosurfaces of  $SI$  for the first case from four different view points. The red curve shows the path of the muscle band, predicted by Torrent-Guasp theory, which has a good correlation with the isosurfaces (see Figure 4.8).

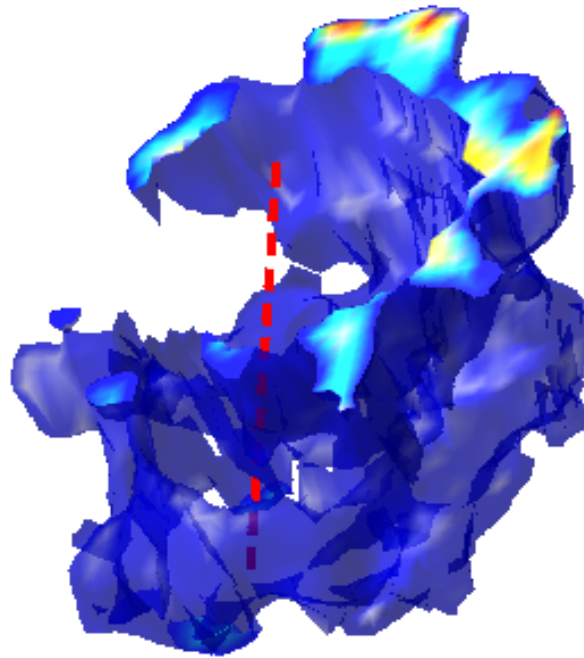


**Figure 4.7** calculated isosurfaces of  $SI$  for the second case. Despite minor differences that might be caused by noise, the overall pattern looks similar to that of figure 4.6.

#### 4.6 Discussion

These results agree with our expectations of an intersecting spiral macro-structure of the LV. It is important to note that the contraction and WT, as well as the tangential shortening of the wall, happen all around the LV, however, Our findings show that this activity has not been uniformly distributed on the wall. Instead, it acts as if a band has been wrapped around the heart, acting as the backbone of the heart contraction.

It is interesting to note that this discovery has a strong histological evidence, that is, the blunt dissection of the heart in the form of a muscle band by Torrent-Guasp (1966, 2001, 2004) (Fig. 4.8). He hypothesized that the pathway of contraction in the heart is on a muscle band which has a shape of helical structure. This is the first time that functional data from a beating heart reveal a pathway based on maximum local contractility.

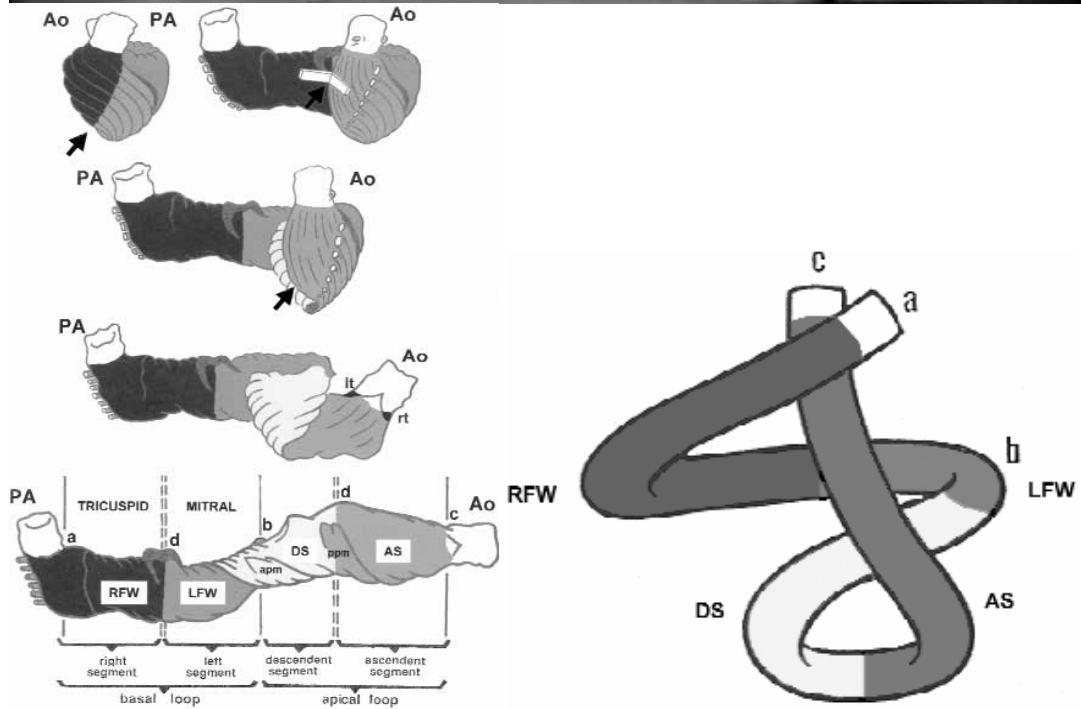
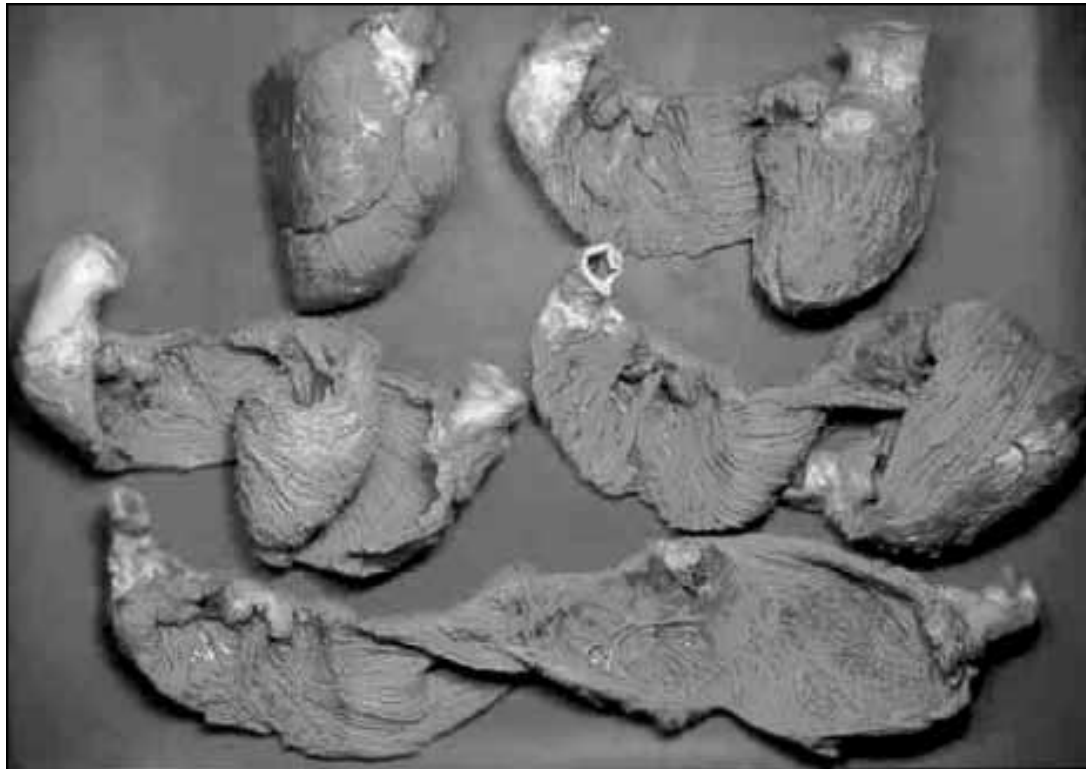


**Figure 4.8** Torrent-Guasp blunt dissection (Top). Schematic representation of the ventricular myocardial band (bottom). From b to c shows LV. All parts of this Figure are from Torrent-Guasp paper which was published in *The Journal of Thoracic and Cardiovascular Surgery*, Volume 122, Francisco Torrent-Guasp et al., p 389-392, Copyright Elsevier (2001). (with written permission)

The most important challenge then is to explain how such a macroscopic structure adheres to the observed micro-pattern of myofibers. It is important to show that our observation is compatible with myofiber patterns that has been observed through histology (Streeter 1979) and the diffusion tensor MRI (Helm, Tseng et al. 2005). The main point of these studies is that the fiber angles change gradually from left-hand twist at the epicardium to right-hand twist at the endocardium.

Using the general information of the fiber orientation in the LV wall (Streeter 1979), some previous investigators quantified the fiber orientation by two angles at each point: the helix fiber angle and the transverse angle. The former is defined as the angle between the circumferential direction and the projection of fiber path on the tangential surface while the latter is the angle between the same circumferential direction and the projection of fiber path on the axial cross section of the LV (Vendelin, Bovendeerd et al. 2002).

Vendelin et al. generalized the findings of the Streeter by applying it to an axisymmetric case (2002). Furthermore, they simplified the transmural changes of the fiber direction by assuming that the helix fiber angle changes linearly from a positive angle (right-hand twist) subendocardially to a negative angle (left-hand twist) subepicardially. They also assumed that the transverse angle is a linear function of  $\bar{\theta}$ , the parameter determining the longitudinal location on the ellipsoid coordinate system, and is tangent to the wall at the endo- and epicardium (Vendelin, Bovendeerd et al. 2002):

$$\alpha_h = P_1 + P_2 \bar{\xi}, \quad (4.3)$$

$$\alpha_t = P_3 \bar{\theta} (1 - \bar{\xi}^2), \quad (4.4)$$

where  $\bar{\xi}$  is the normalized factor in the range of  $[-1,1]$  which determines the radial position from endo- to epicardium. They used optimization algorithms to find parameters  $P_1$  to  $P_3$  that give the most uniform strain and stress in the myocardium. Using their optimum values of  $P_1 = 22.5$ ,  $P_2 = -69$ ,  $P_3 = 5$ , we calculated the path of the fibers. Figure 4.9 shows a bundle of these fibers with the designated parameters, and it illustrates how this bundle can make a muscle band with a configuration similar to the band in figure 4.6.

If one of these possible bundles shows a slightly denser population of fibers, that collection of muscle fibers will show more contractility. Higher  $SI$  and  $T$  values, therefore, will be measured over that bundle. Considering the asymmetrical geometry of

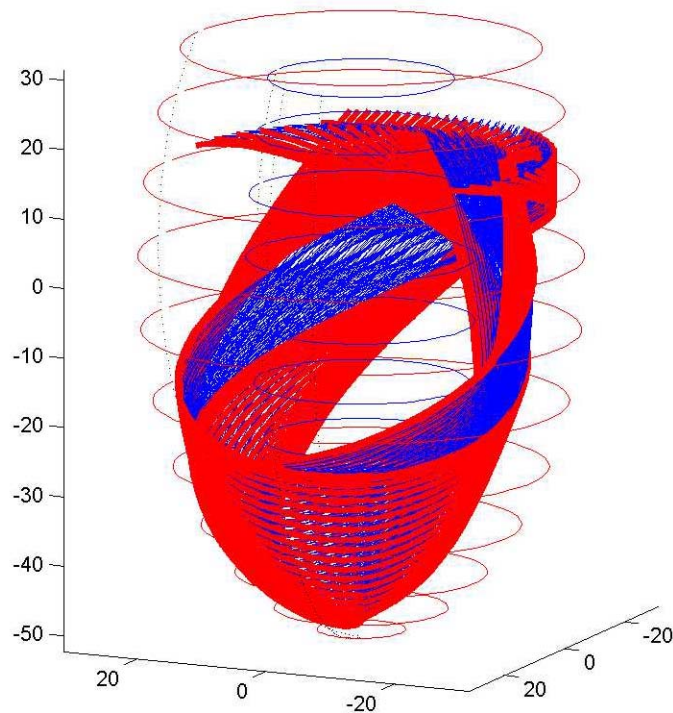


**Figure 4.9** A bundle of fibers as predicted by the optimization modeling in Vendelin, Bovendeerd et al. (2002).

the whole heart, it is obvious that the axisymmetry condition can not be quite true for the LV. The other evidence of LV being asymmetric is provided by the tracking the stages of the heart development. That is while the formation of the LV starts with no symmetry there should be some fingerprint of asymmetry in the adult heart. Thus, the non-uniform density of the fibers is completely expected, and indicates that the contributions of different myocardial regions in the pumping of blood are not equal.

#### **4.7 Chapter Conclusion**

The relation of the form and function of the LV has been studied through investigating the spatial distribution of its regional functionality. *SI* and *WT* were chosen as the characteristic parameters which show this functionality. These parameters were calculated using advanced MRI techniques for measuring the myocardium displacement. We showed how regions with a higher degree of functionality may form a macro-structure for the LV. The histological evidences emphasize the existence of such a band-shaped structure. We further showed the compatibility of the macro-structure with micro-structural organization of the fibers in the LV.

#### 4.8 Chapter References

- Davis, J. S., S. Hassanzadeh, et al. (2001). "The overall pattern of cardiac contraction depends on a spatial gradient of myosin regulatory light chain phosphorylation." Cell **107**(5): 631-41.
- Davis, J. S., S. Hassanzadeh, et al. (2002). "A gradient of myosin regulatory light-chain phosphorylation across the ventricular wall supports cardiac torsion." Cold Spring Harb Symp Quant Biol **67**: 345-52.
- Dokos, S., B. H. Smaill, et al. (2002). "Shear properties of passive ventricular myocardium." Am J Physiol Heart Circ Physiol **283**(6): H2650-9.
- Fujii, H., H. Ohashi, et al. (2005). "Reverse remodeling after endoventricular circular patch plasty in the mid-term period." Interactive CardioVascular and Thoracic Surgery **4**(6): 602-605.
- Gotte, M. J., A. C. van Rossum, et al. (2001). "Quantification of regional contractile function after infarction: strain analysis superior to wall thickening analysis in discriminating infarct from remote myocardium." J Am Coll Cardiol **37**(3): 808-17.
- Guyton, A. C. and J. E. Hall (2000). Textbook of Medical Physiology. Philadelphia: Saunders.
- Helm, P. A., H. J. Tseng, et al. (2005). "Ex vivo 3D diffusion tensor imaging and quantification of cardiac laminar structure." Magn Reson Med **54**(4): 850-9.
- Lapeyre, A. C., 3rd, E. Klodas, et al. (2005). "Quantitation of regional ejection fractions using gated tomographic imaging with 99mTc-sestamibi." Chest **127**(3): 778-86.
- Moore, C. C., C. H. Lugo-Olivieri, et al. (2000). "Three-dimensional systolic strain patterns in the normal human left ventricle: characterization with tagged MR imaging." Radiology **214**(2): 453-66.
- Sechtem, U., B. A. Sommerhoff, et al. (1987). "Regional left ventricular wall thickening by magnetic resonance imaging: evaluation in normal persons and patients with global and regional dysfunction." Am J Cardiol **59**(1): 145-51.
- Streeter, D. D., Jr. (1979). Gross morphology and fiber geometry of the heart. Handbook of Physiology. The Cardiovascular System. The Heart. Bethesda, Am. Physiol. Soc. **1**: 61-112.
- Streeter, D. D., Jr., H. M. Spotnitz, et al. (1969). "Fiber orientation in the canine left ventricle during diastole and systole." Circ Res **24**(3): 339-47.
- Taki, J., T. Higuchi, et al. (2002). "Electrocardiographic gated (99m)Tc-MIBI SPECT for functional assessment of patients after coronary artery bypass surgery: comparison of wall thickening and wall motion analysis." J Nucl Med **43**(5): 589-95.
- Torrent-Guasp, F. (2001). "La mecanica agonista-antagonista de los segmentos descendente y ascendente de la banda miocardica ventricular." Rev Esp Cardiol **54**: 1091-1102.
- Torrent-Guasp, F., M. J. Kocica, et al. (2004). "Systolic ventricular filling." Eur J Cardiothorac Surg **25**(3): 376-86.
- Torrent-Guasp, F. (1966). "On cardiac morphology and functionalism. I." Rev Esp Cardiol **19**(1): 48-55.

Vendelin, M., P. H. Bovendeerd, et al. (2002). "Optimizing ventricular fibers: uniform strain or stress, but not ATP consumption, leads to high efficiency." Am J Physiol Heart Circ Physiol **283**(3): H1072-81.

## CHAPTER 5

### Conclusion

#### 5.1 Primary Contributions

This thesis presents a study on the relationship between the structure and function of the myocardium in both embryonic and adult hearts. This relationship was investigated through an in-depth analysis of the spatial distribution of the local contractile function in the myocardium. The crucial point in our approach was to choose proper parameters that express the local function. We then calculated these parameters based on the measurements provided by advanced imaging techniques such as DENSE MRI and confocal microscopy. We explained that the local functionality in the embryonic heart is expressed by the positive work performed during deformation, and in the adult heart by the tangent surface shortening. This method resulted in novel understandings of the local and global functions in each of these hearts.

##### 5.1.1 Embryonic Heart

Appreciating the effect of hemodynamic forces on the heart development *in vivo* (Hove, Koster et al. 2003), we focused on investigating the pumping mechanism of the heart tube on the zebrafish animal model. We discovered that the functionality of the embryonic heart is not uniformly distributed along the tube, while the previously considered theory of peristalsis implied otherwise (Vogel, 1994). We proved that in the pre-looping stages, only specific parts of the tube are active. In the very early stages, this activity is mainly concentrated in the beginning of the tube and causes the tube to act as a dynamic suction pump (Forouhar, Liebling et al. 2006). Consequently, we understood that the active

filling, which is a functional characteristic of the adult heart (Buckberg, Clemente et al. 2001), is also an underlying mechanism of pumping in the embryonic heart. We also discovered another similarity of these two hearts in their respected torsional movements, which is a known characteristic of the adult heart. While such a movement is not considerable at the age of 26 hpf, it becomes significant when approaching 34 hpf, where at that stage the looping has just started. The positions that generate the twist, were also located.

In the course of this research, an innovative kinematic-based paradigm has been introduced to investigate the structure and function of the embryonic heart based on the spatial distribution of its active regions. Furthermore, through the computational methods, we showed the potential of the four-dimensional confocal laser scanning microscopy in providing detailed information about the HT geometry and kinematics. This information was obtained by tracking the myocytes as the only data used in our approach.

### 5.1.2 Adult Heart

Inspired by the muscle-band theory of Torrent-Guasp (Torrent-Guasp 2001; Torrent-Guasp, Kocica et al. 2004), we defined the macro-structure of an adult heart based on the local wall thickening as well as shortening index  $SI$ . For the first time, we have established credible evidence for the existence of a myocardial muscle band based on its contractile function, as it had been suggested through histological findings of Torrent-Guasp. That is, we showed the iso-surfaces of the  $SI$  are highly correlated with the path of the described muscle band. We have managed to show that previous models based on

micro-structure of the muscle fibers are consistent with the macro-structure of the left ventricle as suggested by Torrent-Guasp.

Our computations were based on measurements of the myocardium deformation through the DENSE MRI which is an advanced imaging technique for tissue tracking. Improvement and optimization of DENSE imaging protocols for cardiac MRI on 3T machine were emphasized during experimental part of the research. We showed that capturing the high spatio-temporal resolution DENSE images from human subjects over the whole cardiac cycle is feasible, and consequently the temporal changes of the strain maps were computed.

By employing this novel imaging technique (DENSE MRI) and image processing algorithms, we developed accurate and efficient computational methods to compute the deformation parameters. In order to compensate for the small number of imaging planes that can be captured from a patient due to limitations in the imaging techniques, we developed a novel method to compute all the six elements of the strain tensor based on displacements of the points in a single slice image.

## **5.2 Future works**

### 5.2.1 Embryonic Heart

The developed methods in this research for finding the active regions of the myocardium can be extended to investigate the role of connective tissues and their relation to the myocyte cells linkage and network. While in chapter 2 we focused to find the location of the active points, the next step is to consider the timing as well as the strength of the

activity. The indications for activity, described in chapter 2, may be presented in a quantitative manner. For example, the first indication which is the large negative strain simultaneous with a major narrowing can be quantified by multiplication of negative strains and narrowing to show the strength of this activity.

Furthermore, the timing of these activities can be measured and compared to shed more light on the pumping process. We also may measure the point to point strain between myocytes to learn more about their connectivity. The primary steps in these directions have been taken and reported in appendix B of this thesis. However, a comprehensive study is still needed over higher number of embryos to result in any biological statement about the myocytes interconnections. These connections may be hypothesized as a premature form of the muscle-band. These studies should also be extended to the later stages of the heart development

### 5.2.2 Adult Heart

Having found the first functional evidence of a muscle band, the characteristics of a normal band should be sought through performing this process over a large number of the normal population. Once these characteristics are found, their deviations from the normal values may be investigated in different heart disease like ischemia or aneurism. These parameters may present a myocardium model and their variations from the normal situation can help in medical decision making as well as the planning of restoration surgeries. We may also use these parameters to evaluate the effectiveness of the different treatments for the heart failure.

DENSE MRI also can be used for several local and global parameters of the heart. Some of these calculations are presented in appendix C of this thesis.

For both embryonic and adult heart our findings may be exploited in dynamic heart modeling. Especially in combination with material properties of the myocardium, they may help in calculation of the stresses.

### 5.3 Chapter References

- Buckberg, G. D., C. Clemente, et al. (2001). "The structure and function of the helical heart and its buttress wrapping. IV. Concepts of dynamic function from the normal macroscopic helical structure." Semin Thorac Cardiovasc Surg **13**(4): 342-57.
- Forouhar, A. S., M. Liebling, et al. (2006). "The embryonic vertebrate heart tube is a dynamic suction pump." Science **312**(5774): 751-3.
- Hove, J. R., R. W. Koster, et al. (2003). "Intracardiac fluid forces are an essential epigenetic factor for embryonic cardiogenesis." Nature **421**(6919): 172-7.
- Torrent-Guasp, F. (2001). "La mecanica agonista-antagonista de los segmentos descendente y ascendente de la banda miocardica ventricular." Rev Esp Cardiol **54**: 1091-1102.
- Torrent-Guasp, F., M. J. Kocica, et al. (2004). "Systolic ventricular filling." Eur J Cardiothorac Surg **25**(3): 376-86.
- Vogel, S. (1994). Life in moving fluids : the physical biology of flow. Princeton, N.J., Princeton University Press.

**The Embryonic Vertebrate Heart Tube Is a Dynamic Suction Pump****Published in *Science*, 312 751-753 (5 May 2005)**

Arian S. Forouhar<sup>1</sup>, Michael Liebling<sup>2</sup>, Anna Hickerson<sup>1</sup>, **Abbas Nasiraei-Moghaddam**<sup>1</sup>, Huai-Jen Tsai<sup>3</sup>, Jay R. Hove<sup>4</sup>, Scott E. Fraser<sup>1,2</sup>, Mary E. Dickinson<sup>2,5</sup>,  
Morteza Gharib<sup>1</sup>

1-Option in Bioengineering, Caltech, Pasadena, CA 91125

2-Biological Imaging Center, Beckman Institute, Caltech, Pasadena, CA 91125

3-Institute of Molecular and Cellular Biology, National Taiwan University, Taiwan

4-Genome Research Institute, University of Cincinnati, Cincinnati, OH 45221

5-Department of Molecular Physiology and Biophysics, Baylor College of Medicine,  
Houston, TX 77030

\*To whom correspondence should be addressed. E-mail:  
mgharib@caltech.edu

Supporting Online Material  
[www.sciencemag.org/cgi/content/full/312/5774/751/DC1](http://www.sciencemag.org/cgi/content/full/312/5774/751/DC1)  
Materials and Methods  
Figs. S1 and S2  
Movies S1 to S4  
13 December 2005; accepted 6 April 2006  
10.1126/science.1123775

---

<sup>1</sup> This APPENDIX consists of the text and figures of the accepted version of our published paper in *Science* magazine. The format is therefore different from other chapters. Movies are only accessible through the magazine website.

**The embryonic vertebrate heart begins pumping blood long before the development of discernable chambers and valves. At these early stages, the heart tube has been described as a peristaltic pump. Recent advances in confocal laser scanning microscopy and four-dimensional visualization have warranted another look at early cardiac structure and function. Here we examine the movement of cells in the embryonic zebrafish heart tube and the flow of blood through the heart, and obtain results that contradict peristalsis as a pumping mechanism in the embryonic heart. We propose a more likely explanation of early cardiac dynamics in which the pumping action results from suction due to elastic wave propagation in the heart tube.**

The cardiovascular system is the first functional organ system to develop in vertebrate embryos. In its earliest stages it consists of a primitive heart tube that drives blood through a simple vascular network. Cardiac physiologists have long conjectured that the valveless embryonic heart tube drives circulation by means of peristaltic contractions (1,2), a pumping mechanism that pushes blood through the heart tube by progressively reducing the tube volume (3). Confirmation of this pumping mechanism requires *in vivo* visualization and quantification of both heart wall motion and blood cell motion, which is difficult with traditional imaging modalities. The zebrafish offers a powerful vertebrate model for cardiogenetic studies (4-7) with multiple advantages for *in vivo* imaging: eggs are externally fertilized, embryos are nearly transparent providing optical access to the earliest stages of cardiogenesis, and many GFP- (green-fluorescent protein) labeled transgenic strains have been derived.

Recent improvements in confocal microscopy (8) and four-dimensional (three spatial dimensions + time) reconstruction protocols (9) permit us to take full advantage of these qualities and revisit the pumping mechanism of the early embryonic heart tube. Here, we test three implications of peristaltic pumping in the heart, namely that (i) there should be a unidirectional wave traveling along the endocardial layer; (ii) blood cell velocities should be bounded in magnitude by the instantaneous traveling wave speed through the heart tube wall; and (iii) cardiac output should increase linearly with heart rate.

To test the nature of cardiac pumping we employed *in vivo* high-speed confocal imaging of zebrafish hearts prior to valve formation. Optical sections through 26-hour-postfertilization (hpf) Tg(*gata1*::GFP) zebrafish hearts, expressing GFP in blood cells, endocardium, and myocardium, were reconstructed into four-dimensional data sets (9) (Movie 1), which provide direct three-dimensional data on the position of myocardial and endocardial cells throughout the cardiac cycle (Movies 1-3). By tracking the position of the trailing edge of the endocardial wave crest during the cardiac cycle, we identified the speed and direction of the traveling wave through the heart wall. The wave originates in myocardial cells positioned near the inflow tract of the heart tube (Fig. 1) and upon contraction, a bidirectional wave propagates axially along the heart tube wall (Fig. 1 and Movies 1,2). The proximity of the pacemaker cells to the venous boundary of the heart tube, along with the speed of the traveling wave, combine to make this bidirectional wave undetectable through traditional imaging modalities.

In a peristaltic heart tube model, the net flow is exactly equal to the volume displaced during contractions. This dynamic imposes a direct relationship between the upstream blood velocity and the local traveling wave velocity. Specifically, since peristalsis is

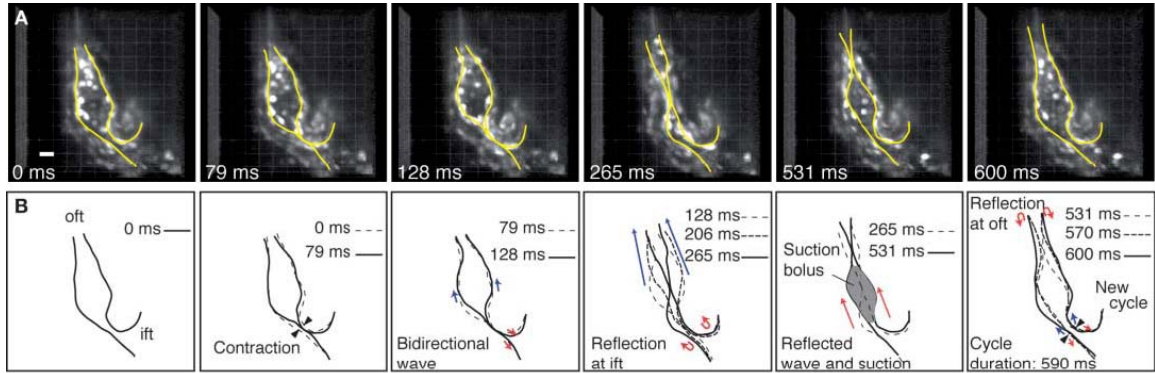


**Figure 1. Biomechanics of embryonic heart tube contractions contradicts peristalsis as the main pumping mechanism. (A) Three-dimensional reconstructions of a 26 hpf *Tg(gata1:GFP)* zebrafish heart tube at six time points. Yellow lines denote the shape of the endocardial layer. (B) Superimposed outlines of different time points highlight bidirectional traveling wave (red and blue arrows). Black arrowheads indicate contraction location. Shaded gray region indicates suction bolus. Regions of mismatched impedance at the inflow tract (ift) and outflow tract (oft) of the heart tube are reflection sites. Grid spacing is 20  $\mu\text{m}$ .**

governed by static pressure rather than dynamic pressure (3), it would imply that the upstream blood velocity in the zebrafish heart does not exceed the simultaneous local traveling wave velocity. However, in each of the cases observed ( $n=5$ ), the maximum velocity of the upstream blood accelerates to velocities exceeding the wall wave speed (Fig. 2).

To investigate how the cardiac output varied with the contractile wave frequency *in vivo*, we altered temperature to manipulate heart rates, and tracked blood cells to determine the flow rate. In this temperature range (24-34  $^{\circ}\text{C}$ ), fish develop normally, and we do not expect a non-linear change in blood viscosity. If the heart tube were a peristaltic pump, the cardiac output should increase linearly with the contractile wave frequency. However, we found that the blood velocity response, and thus the net flow rate response, to a monotonic heart rate change is surprisingly non-linear (Fig. 3).

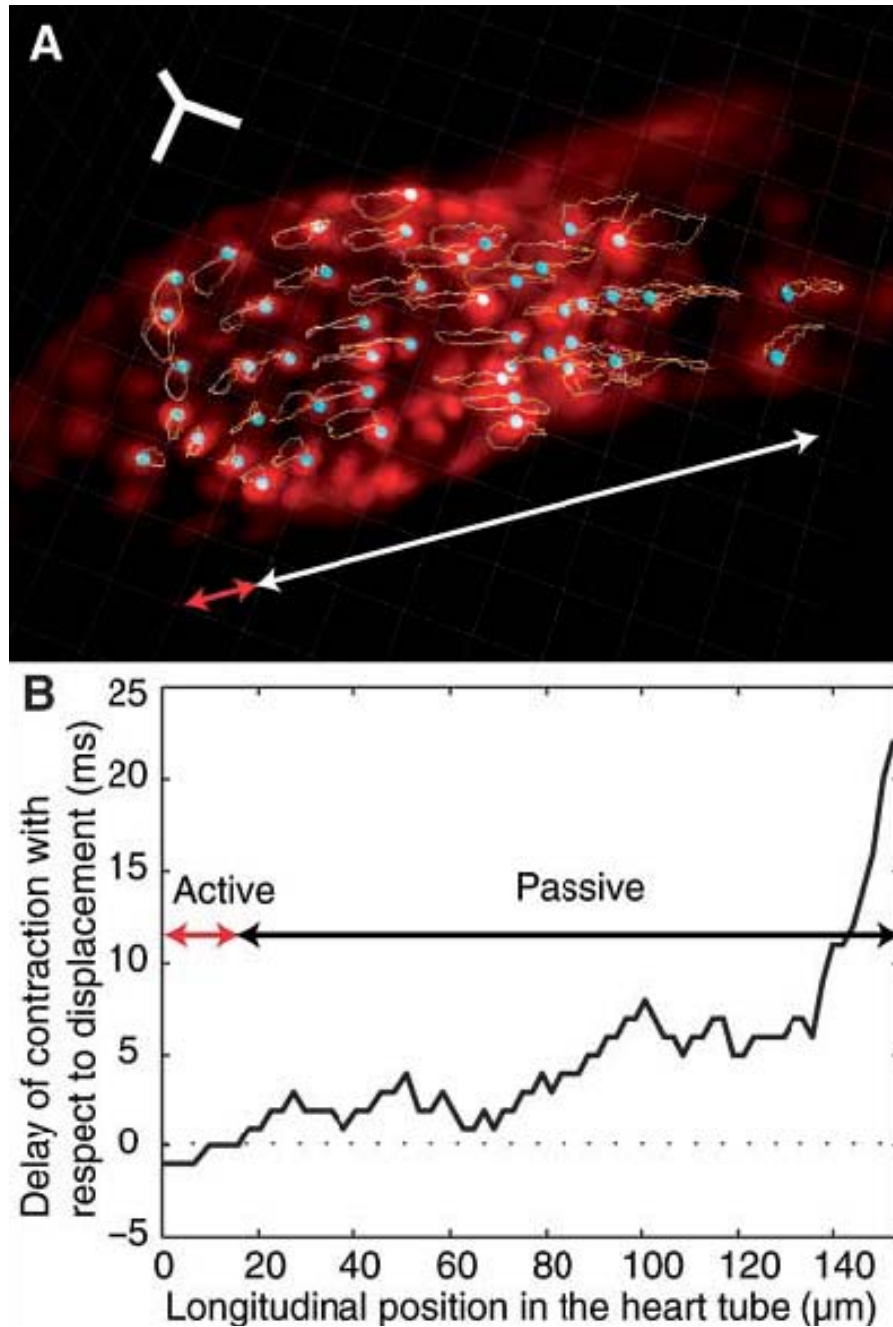
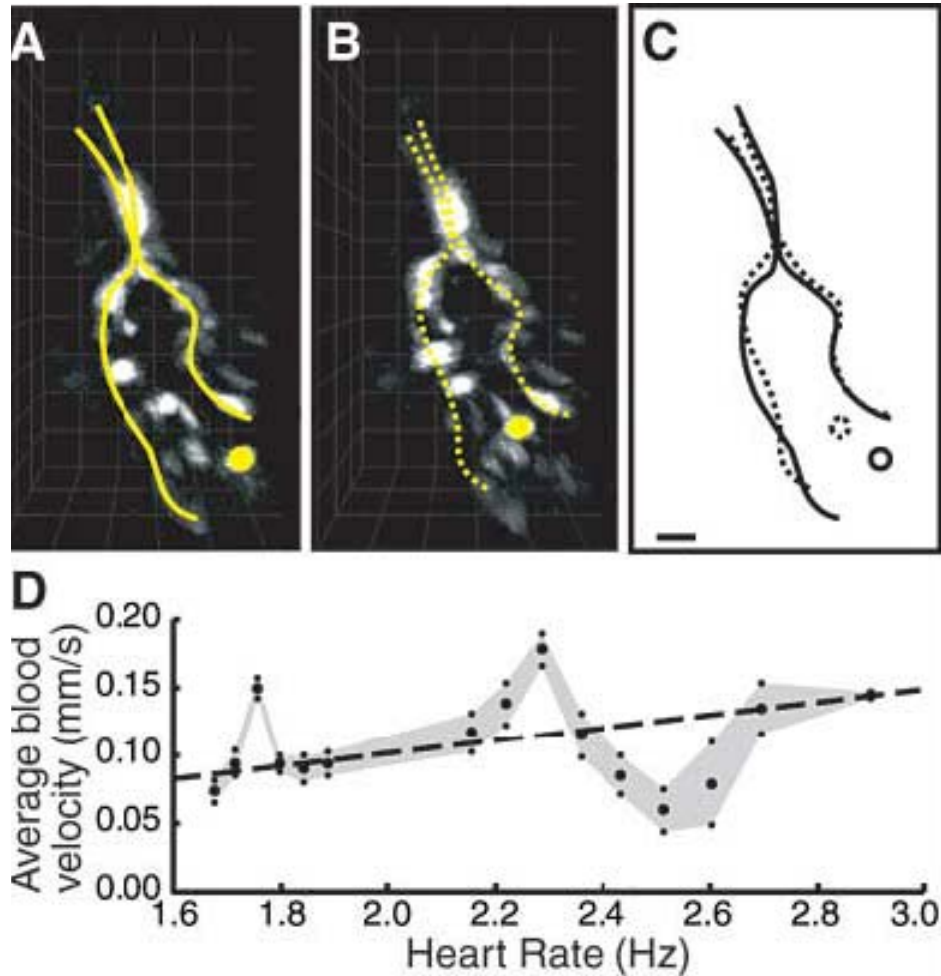


Figure 2. Heart tube contractions convey active and passive regions. (A) Three-dimensional reconstruction of a 26-hpf *Tg(cmlc2:GFP)* embryo. Myocytes are fluorescently labeled, and their three-dimensional trajectories during two complete cardiac cycles are shown. The red double-arrow line indicates the active pacemaker region and the double-arrow white line, the passive region. The orthogonal scale bar triplet indicates 20  $\mu\text{m}$  in each direction. (B) The active pacemaker region spans the first 20  $\mu\text{m}$  of the heart tube. It was identified by calculating the time difference between the moment myocardial cells at a given position along the tube experience a 10 to 13% strain rate with neighboring cells and the time at which they each reach 90% of their maximal displacement. When this time difference is nearly zero, the region experiences active contraction.



**Figure 3. Blood cell motions demonstrate nonperistaltic pumping mechanism in the embryonic heart tube. (A and B) Reconstruction of a 26-hpf *Tg(gata1::GFP)* embryo. The endocardial layer, along with a blood cell, have been marked in yellow in each image. (C) Superposition of schematics in (A) and (B). Blood cell displacement is much greater than traveling wave crest displacement, indicating that blood cells do not passively follow the traveling wave. Scale bar indicates 20  $\mu\text{m}$ . (D) Non-linear frequency flow relationship for 26 hpf zebrafish heart tube (see methods section). Resonance peaks in the observed average blood velocity at 1.75 and 2.3Hz exceed the expected estimate for peristaltic pumping (dashed line).**

These three observations indicate that the embryonic heart tube does not act as a peristaltic pump; instead, they seem consistent with a previously investigated hydro-impedance pump model (10). In this model of valveless pumping, the pumping action results from elastic wave propagation and reflection in the heart tube; resonance conditions arise at certain frequencies where the phase speed permits constructive

interference between the incident and reflected pressure waves. Mechanical properties of the system such as the diameter, length, elasticity, and pressure dictate the wave speed as well as the attenuation and reflection coefficients in the system. The impedance pump model exhibits a sensitivity of the generated flow to activation frequency that is similar in many ways to our *in vivo* observations (Fig. 3), including non-linear flow with frequency, domains of negative slope, and resonance frequencies that allow higher flow rates than peristalsis.

The impedance pump model requires mismatches in impedance to induce wave reflections at the boundaries of the pump element to build up suction and induce net flow (10). In zebrafish, many mechanical properties of the heart tube boundaries contribute to mismatched impedance. The most prominent feature at the inflow boundary of the heart tube is a drastic change in diameter (Fig. 4). The heart tube stems from the surface of the spherical yolk sac, acutely narrows to about 30  $\mu\text{m}$ , and becomes lined by an additional layer of cells (myocardium) and cardiac jelly that alters the elasticity of the heart tube at the inflow boundary (Fig. 4). Our four-dimensional data confirm that this region of mismatch impedance is indeed a site of wave reflections. Pacemaker cell contractions initiate axial waves that travel along the heart tube until they reach the heart tube boundaries. When these waves reach the inflow and outflow boundaries they reflect in the form of sudden expansions and begin to travel back through the heart tube (Movies 1,2).

The sudden expansions of the cardiac lumen at the reflection sites create low-pressure zones and suck blood through the heart tube (Movie 1). In order to describe this suction mechanism *in vivo*, we looked at the pressure-flow relationship through the heart tube

during the cardiac cycle. By measuring the radius of the cardiac lumen at two cross sections a short distance apart, we deduced the pressure gradient at a point (11) (Fig. 4C, Movie 4). In this region, blood cells first begin to accelerate when the pressure gradient is negative, analogous to drinking liquid through a straw. Blood cells continue to accelerate, reaching a maximum as the pressure gradient climbs from negative values towards zero.

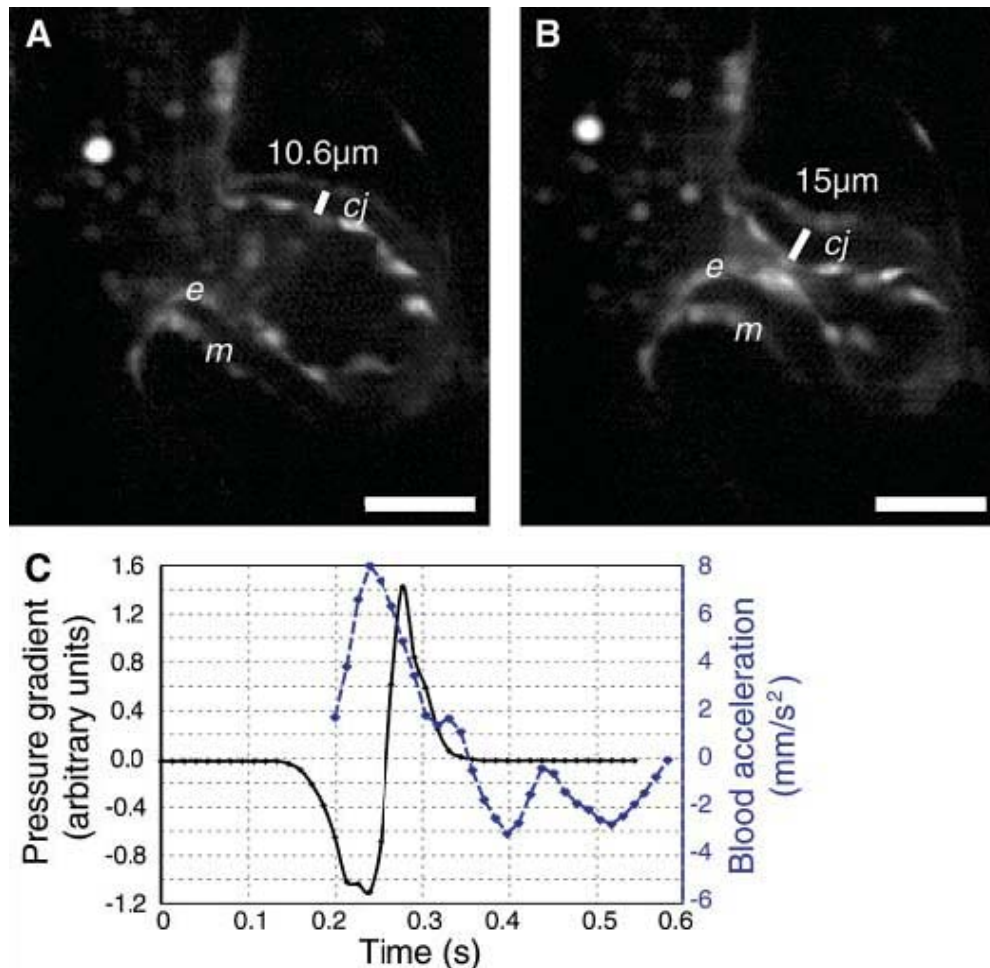


**Figure 4. Hydroelastic-based suction mechanism in the embryonic heart tube. (A)** Inflow region of a 26 hpf embryo. The distance between the myocardial (m) and endocardial (e) layers is marked. **(B)** Upon contraction, this distance increases. The expansion of the cardiac jelly (cj) at the site of contraction illustrates the elastic nature of the heart wall, a requirement of the impedance pump model. This observation contradicts the muscularly driven peristaltic mechanism because the concentric rings of endocardium and myocardium do not approach each other during contraction. Scale bars are 50 μm. **(C)** Blood cell accelerations and estimated pressure gradient as a function of time (Materials and Methods). The maximum acceleration occurs when the pressure gradient is negative, indicating that the embryonic heart tube acts as a suction pump.

As the pressure gradient continues to increase from zero to positive values, blood cells continue to move forward, but with decreasing accelerations. Finally, when the pressure gradient reaches a maximum and begins to decrease, blood cells decelerate until they finally reach a resting point. Importantly, a phase difference between the maximum acceleration and the maximum pressure gradient exists. Specifically, blood reaches a maximum acceleration a short time after there is a local minimum in the pressure gradient. This time lag between suction pressure and flow in the embryonic heart resembles the pressure-flow relationship of a fluid dynamic pump (3) rather than a peristaltic mechanism where such a time lag should not exist.

Using new *in vivo* imaging tools, we have taken a closer look at early cardiac structure and function and identify three biomechanical properties of embryonic heart tube contractions that contradict cardiac peristalsis; (i) a bidirectional, as opposed to unidirectional, wave traverses the endocardial layer; (ii) blood cell trajectories do not follow local endocardial wave trajectories and exhibit velocities significantly greater than those of the traveling wave; and (iii) the frequency-flow relationship is non-linear and exceeds the maximum flow rate possible for a peristaltic pump. Furthermore, we observed: (i) resonance peaks in the frequency-flow relationship; (ii) mismatched impedance at the inflow and outflow tracts, and visible wave reflections at the heart tube boundaries; and (iii) a pressure-flow relationship that exhibits a phase difference between the maximum acceleration of the blood and the maximum local pressure gradient. Thus, the valveless embryonic heart does not drive circulation through peristalsis. Instead, these observations suggest a hydroelastic impedance pump model based on elastic wave propagation and reflection (10). The simple mechanism we propose requires only a single

actuation site rather than complete synchrony throughout the heart tube. The frequency-dependent sensitivity of this pumping mechanism itself suggests that such valveless pumping may not be suitable for post-embryonic circulation in ectotherms. The presented characterization of early cardiac biomechanics should provide the foundation to revisit many aspects of embryonic cardiogenesis and provides the first evidence for an embryonic root to the observed suction action of the adult heart (12).

#### Acknowledgements:

We thank John Dabiri, Michele Milano, Julien Vermot, and Jim Pierce for comments on the paper. We thank Shuo Lin for providing the Tg(*gata1*::GFP) zebrafish line. We thank Sean Megason and Le Trinh for help with zebrafish and imaging techniques. This work was supported by the American Heart Association 03665071Y(J.R.H.), National Institute of Health 5R01HL078694(S.E.F, M.E.D, M.L.) and Swiss National Science Foundation, PBEL2-104418, PA002-111433(M.L.).

## Methods

### *Embryo Preparation*

Standard methods were used in spawning adult zebrafish and raising their embryos. Embryos were anesthetized in 0.0175% tricaine. 26 hpf Tg(*gata1*::GFP) embryos were placed ventral side up in wells etched into an agarose filled Petri dish. The orientation of the embryos was adjusted manually through the use of a small capillary tube.

### *Imaging*

Embryos were raised at 28.5°C and, unless otherwise noted, imaged at 24°C. Bi-directional confocal scans (256x256 pixels) were taken at 151 frames per second (fps).

Time series were triggered at a random time in the cardiac cycle and taken for 300-500 frames. Upon completion of a two-dimensional time series at one z-section, the optical plane was moved 3-5 microns and the acquisition was repeated. Four-dimensional datasets were collected from 15-25 z-sections and did not exceed 100 microns in total depth.

### *Quantitative Flow Analysis*

Blood cell velocities were computed from image sequences, 5-10 cardiac cycles in length, acquired in fish at temperatures between 24°C and 34°C. For every sequence, we selected the same portion of the heart near the center-line of the tube at the venous boundary as a region of interest. We manually marked the first frame of each cardiac cycle in which compression occurs defining cycles of variable length, or equivalently, frequency. For every cardiac cycle, individual blood cell trajectories were tracked manually and pixel positions recorded over time. Cells were chosen that maintained their intensity values (indicating that their motion was largely in the focal plane) while traversing the region of interest. The instantaneous velocity of a cell was computed using the distance traveled between two frames along the angular orientation of the heart tube. For each cycle length, the velocities from sequences of corresponding duration were merged to yield a minimum of one velocity and up to twelve velocity measurements for each time step. For all data corresponding to one cycle length ( $\pm 0.007$  seconds), a Monte Carlo sampling was performed. In this method, a velocity from each time step in a cycle is chosen at random. The average velocity for the given cycle length is then computed from these points. The random sampling is repeated 1000 times for each cycle length from which a mean and standard deviation of average velocities was computed.

We tested the sensitivity of our results to the number of velocity points at each phase by computing average velocities only from phases that had at least three data values. Even under these stringent conditions, the non-linear frequency-flow relationship is conserved. The anticipated peristaltic rate was determined by assuming the heart was cylindrical and estimating the length of the actively compressing component during each cardiac cycle. We determined the average flow velocity by dividing the flow rate, which is equal to the volume compressed multiplied by the compression frequency, by the cross-sectional area.

#### *Pressure Variation Estimates*

In order to estimate pressure variations over time at a given position  $z$  along the heart tube axis, we utilized two known relations, (i) the oscillating pressure gradient with respect to time,  $dP/dt$ , is proportional to the spatial derivative,  $\delta P/\delta z$ , when  $\delta z$  is small (11), and (ii) the pressure is proportional to the inverse of the radius of the tube ( $P = \alpha/R$ , Laplace Law). Combining these two equations, we get

$$dP/dt \propto (R_1 - R_2)/(R_1 R_2)$$

where  $R_1$  and  $R_2$  are the radii of the heart tube at neighboring cross sections. By measuring the latter radii over time (see Movie 4), and assuming a circular cross section, changes in pressure can be determined at the imaging time-resolution ( $\pm 0.007$  s).

#### *Image Processing*

Confocal images were collected and analyzed using the Zeiss 510 LSM software. Time series of two-dimensional sections were temporally registered in Matlab using a correlation process after conditioning data using a multiresolution wavelet transform (9). Four-dimensional data sets were analyzed using Imaris (Bitplane AG).

**References**

1. M. C. Fishman, K.R. Chien, *Development* **124**, 2099 (1997).
2. S. F. Gilbert, *Developmental Biology*. (Sinauer Associates, Massachusetts, 2000).
3. S. Vogel, *Life in Moving Fluids*. (Princeton Univ. Press, New Jersey, 1994), pp. 323-9.
4. M. Fishman, *Science*. **294**, 1290 (2001).
5. J.R. Hove *et al.*, *Nature*. **421**, 172 (2003).
6. D. Y. Stainier, *Nat. Rev. Genet.* **2**, 39 (2001).
7. D. Yelon, *Dev. Dyn.* **222**, 552, (2001).
8. <http://www.zeiss.com/4125681C00466C26/allBySubject/44792DEDFEC5FB9B85256CB10064411E>
9. M. Liebling, A.S. Forouhar, M. Gharib, S.E. Fraser, M.E. Dickinson, *J. Biomed. Optics* **10**, 054001 (2005).
10. A. I. Hickerson, D. Rinderknecht, M. Gharib, *Exp. in Fluids* **38**, 534 (2005).
11. W. W. Nichols, M.F. O'Rourke, *McDonald's Blood Flow in Arteries*. (Oxford Univ. Press, New York, 1988) pp. 98-102.
12. G. D. Buckberg, *et al. Semin. Thorac. Cardiovasc. Surg.* **13**, 342 (2001).

**APPENDIX B:****Timing and strength of activities in the embryonic heart**

The developed methods in this research for finding the active regions of the myocardium can be extended to discover the internal connections of the myocytes. While in chapter 2 we focused to find the location of the active points, the next step is to consider the timing as well as the strength of the activity. The indications for activity, described in Chapter 2, may be presented in a quantitative manner. Further the timing of these activities can be measured and compared to shed more light on the pumping process. Here we shortly address these next steps for each of the activity indications:

1. Regions that have large negative strains simultaneously with a major narrowing of the tube.

Quantitative parameter that shows the strength of this activity may be chosen as multiplication of negative strain and narrowing. An elaborated mathematical term can also determine this simultaneity.

2. Comparison between the time at which the *major* axial displacement and the *major* shortening occur.

The moment of 12% shortening can be considered as a threshold to determine the time of activity. Also the amount of delay (as discussed in Chapter 2) may quantify its strength

3. Significant torsion, which can be inferred from the relatively strong bipolar circumferential movement, constitutes another evidence of activity.

For this indication of the activity, its strength is quantified by the amount of torsion. The moment that torsion reaches its local maximum may be chosen to show the time of activity.

However, the combination of the three mentioned parameters that quantify the strength of activity is not so straightforward. The reason is that the focus of each one is different from the others. For example if the contraction is mainly in the longitudinal direction, no major narrowing or torsion will happen. In contrast, if the major principle strain of the contraction is directed in an oblique angle, it will result in a major torsion. It suggests that the direction of the contraction or the connectivity of the myocytes may be studied through the relative strengths defined above.

We also may measure the point to point strain between myocytes to learn more about their connectivity. Figure B.1 shows these strains between a selected myocyte and three

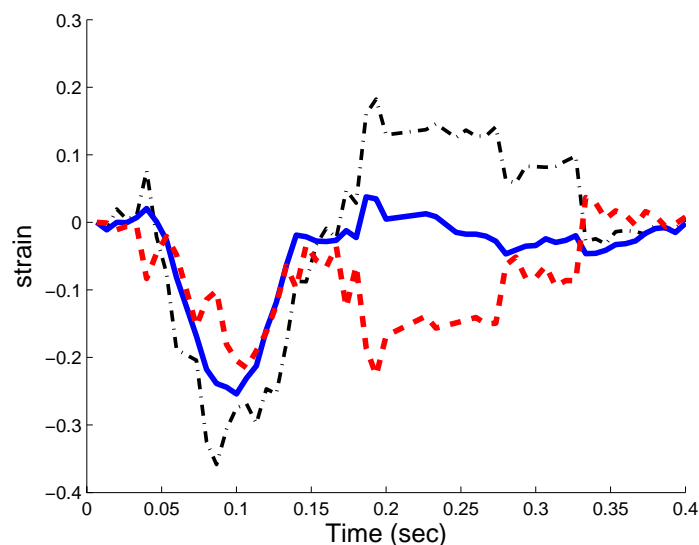


**Figure B.1** Point-to-point strain calculation of a selected myocyte near the in-flow with three of its neighboring myocytes. The myocyte corresponding to the solid-line plot should have a direct connection to the selected myocyte.

other myocytes in its neighborhood separately. Only one of these three strains, solid line, does not show any positive strain while two others show opposite deviations from this one after 150 ms. It shows that the connectivity between the corresponding myocyte and the selected myocyte is stronger and therefore these two can show kind of fiber orientation at the selected myocyte.

However, the point to point strains do not always give such a clear result. These strains are illustrated for some other points in Figure B.2. These show the best match to the expected pattern of

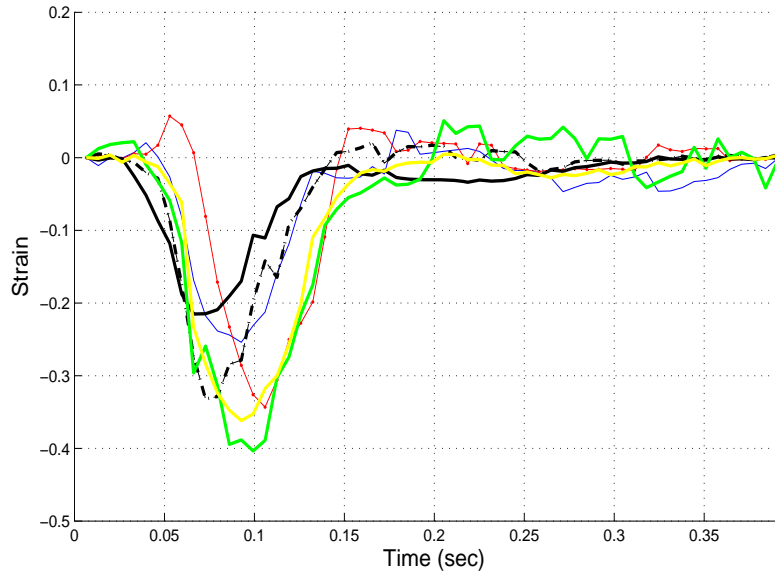


**Fig B.2 Point-to-point strains for some other points.**

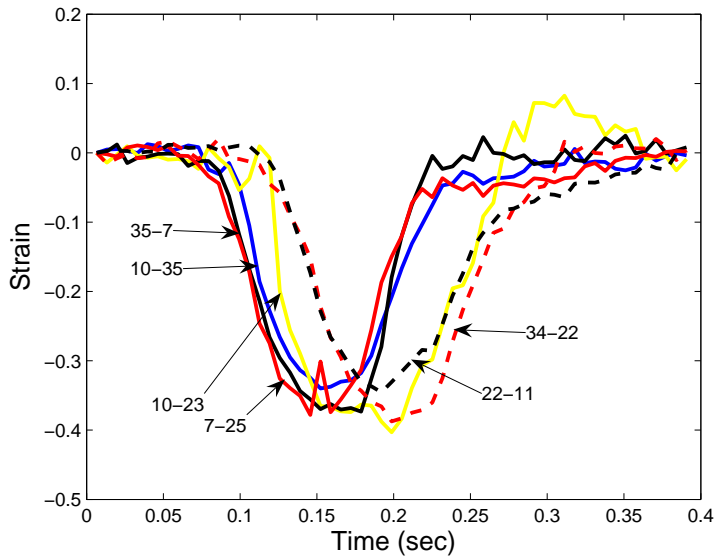


**Fig B,3 This approach may give some information about the timing too, as it clearly shows two contractions with 50 msec separation in two different region. Each myocyte is determined with a number.**

strain that we could find for point-to-point strains.

The patterns are different and in most of cases we cannot prefer one point among the neighboring myocytes that is most related to the selected myocyte. This approach may give some information about the timing too as it is clear in Figure B.3. The numbers just refer to the myocytes. The values of numbers do not show anything.

With some assumptions we may extract some information about the kinetic of the tube too. For example if we assume that the internal pressure of the tube is almost constant when it is at rest, then the normalized work which is performed by the myocardium in the onset of contraction can be calculated just by volume changes. This quantity is shown in the plot of Figure B.4 for all slices along the tube and shows the obvious activity of the beginning part of the tube:

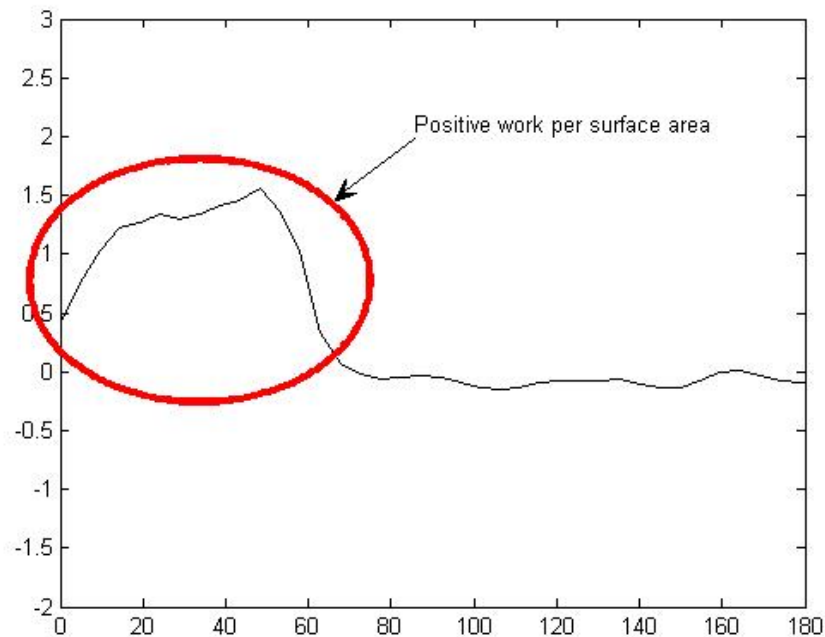
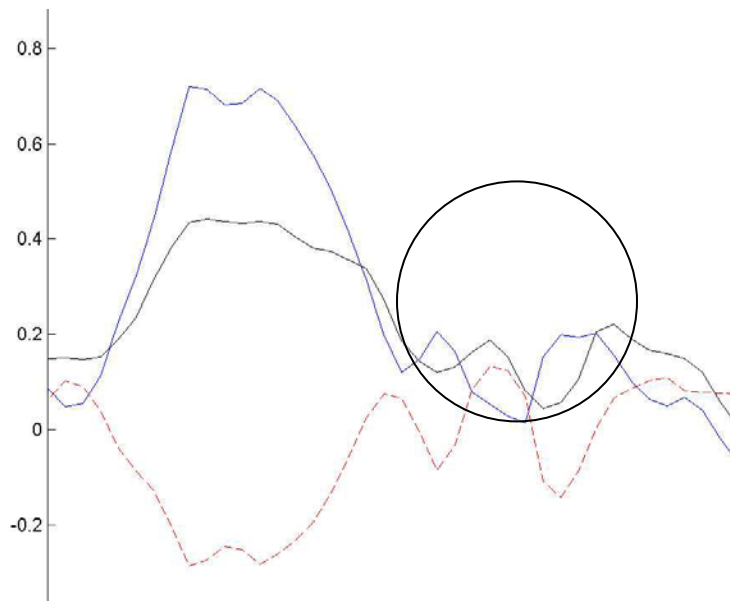


**Fig B.4 Positive work per surface area in the onset of contraction. The uniform internal**

In contrast the opposite phase of the strain and  $dA/A$  is a sign of passiveness at least for the parts with positive strain. Wall motion reflects the internal pressure changes.

Here red plot shows the strain and the black one shows the area changes. Blue shows the total VSF for that slice.



## APPENDIX C:

**3-D Measurement of Cardiac Deformation from DENSE MRI Data**

Presented at BMES 2005

Abbas Nasiraei Moghaddam, Nikoo R. Saber, Han Wen, Morteza Gharib

Short-axis images of a sheep heart, acquired via DENSE (displacement encoding with stimulated echoes) MRI during systolic contraction, have been used to measure mechanical deformations in the cardiac wall. The images had an in-plane resolution of 1.5 x 1.5 mm and temporal resolution of 20 msec over five slices distanced 12 mm apart on the main long axis. Insufficient spatial resolution in the long-axis direction was compensated by using quadratic surface formula to find the deformation gradient matrix as well as the right-hand stretch tensor. The method has been validated on an analytically simulated motion of a twisting cylinder. Spatial and temporal changes of torsion along the long axis, as well as thickening and shortening indices for representative points of the heart muscle, have been calculated and qualitatively compared to measurements made by other methods. Moreover, the principal strain and total deformation values have been analyzed globally in the left ventricle.

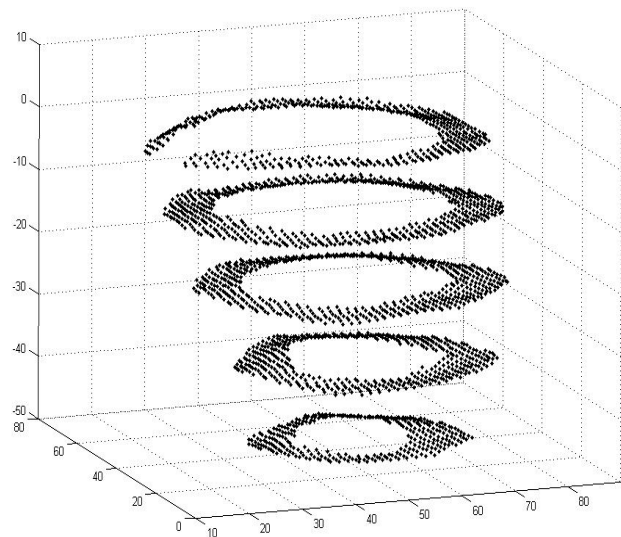


**Figure C.1 Resolution of 3D DENSE MR images are not generally good in the 3rd direction because of the high slice thickness required. Therefore we have used a 2nd degree quadratic form added to the linear part, so that the least square method approximation of the deformation takes the rotation into account.**

## Mechanical concepts

DENSE MRI provides an excellent in-plane resolution, however the separation of slices and slice thickness are relatively large. As a remedy to this problem we may increase the accuracy of the estimation of the deformation gradient matrix  $F$  (see chapter 3) by adding a second degree quadratic form to the linear part of the deformation. That is, to estimate the first row of the matrix  $F$  we use a second degree quadratic form for deformation:

$$dx \approx [F_{11} \ F_{12} \ F_{13}] \times \begin{bmatrix} dX \\ dY \\ dZ \end{bmatrix} + [dX \ dY \ dZ] \times \begin{bmatrix} a_x & d_x & e_x \\ d_x & b_x & f_x \\ e_x & f_x & c_x \end{bmatrix} \times \begin{bmatrix} dX \\ dY \\ dZ \end{bmatrix}. \quad (\text{C.1})$$

Therefore the Cauchy-Green tensor  $C$  is determined through multiplication of the  $F$  transposed by  $F$ . Decomposing the deformation  $F$  to the rotation ( $R$ ) and stretch ( $U$ ) tensors, it becomes evident that  $C$  is not affected by the rigid body motion (rotation).

$$C = F^T \cdot F = U^T \cdot R^T \cdot R \cdot U = U^2. \quad (\text{C.2})$$

Then the Lagrangian Strain Tensor  $E$  is calculated as follows:

$$E = \frac{1}{2}(C - I). \quad (\text{C.3})$$

Eigenvalues of strain tensor are called principle strains and its eigenvectors are principle directions.

$$E \cdot V = \lambda \cdot V. \quad (\text{C.4})$$

The effect of strain tensor in the principle directions is a pure scaling. As  $E$  is symmetric and definite positive, existence of 3 normal Eigen vectors for each single point, which make a new orthogonal coordinate system for that point, is guaranteed. By transferring to this coordinate system only tensile strains will remain with no shear strains.

Some results:

a) shortening index  $SI$ , as defined in Chapter 4, was calculated in this dataset as shown in the left. In the right the  $SI$  is shown for base in the human heart based on calculations of Moore et al. (2001)

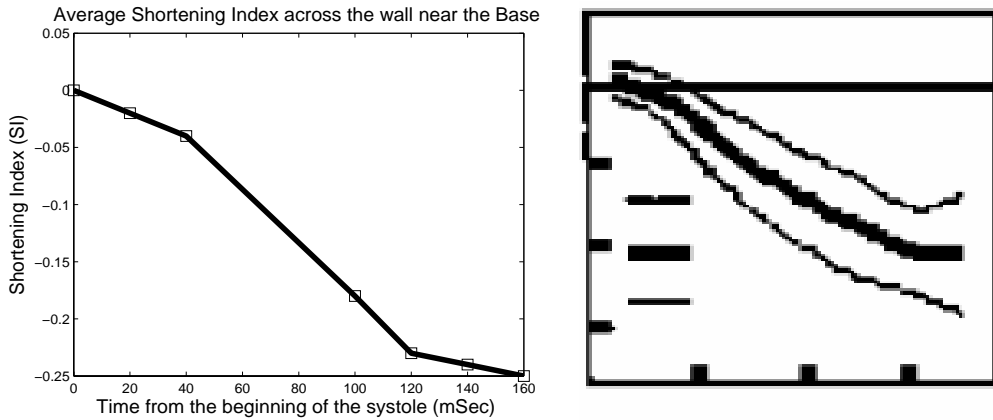


**Figure C.2 (left) Shortening Index (equation (4.1)) for one point on the epicardium of the sheep left ventricle as a function of time during the systole period. The point is near the base and results are in good agreement with Moore’s results (right).**

b) Torsion angle: (Left) torsion angle in the ship heart from apex to base, (Right) the torsion angle in different layers over the course of time.

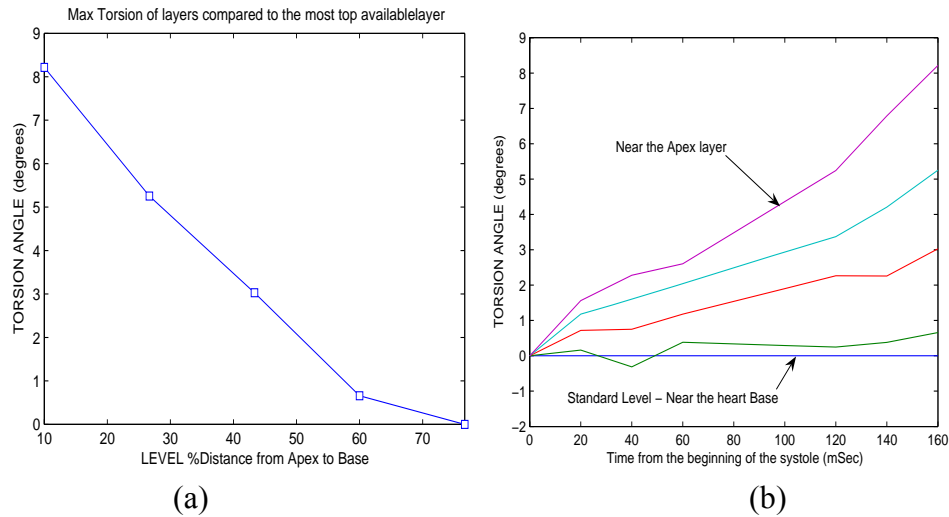


**Figure C.3. DENSE short axes images may easily be used to calculate different mechanical parameters for the heart. As an example this figure shows torsion angle along the long axis of the heart for the sheep left ventricle as a function of (a) distance from the apex (only maximum torsion) (b) time during the systole period.**

**APPENDIX D:****Combination of Short Axis and Long Axis Data**

Presented at ISMRM 2006

A. N. Moghaddam, H. Wen, M. Gharib

**Introduction:** Displacement ENcoding with Stimulated Echoes (DENSE) MRI is a phase contrast method that provides a three-dimensional Lagrangian frame work for particle tracking. This noninvasive method has some advantages over other methods in the area of quantitative analysis of myocardial deformation. In contrast with tagging which is affected by tag fading and provides only the in-plane Lagrangian displacement, DENSE has a higher spatial and temporal resolution and is able to image the entire cardiac cycle. However it is time consuming and therefore the full potential of this novel method has not been revealed. In this study we have shown the feasibility of the combination of short axis (SA) and long axis (LA) images that provides a more comprehensive data from DENSE MRI in 20% to 40% shorter time.

**Methods:** Experiments were performed in a Siemens Trio 3T MR whole body scanner at the Caltech brain imaging center with an eight-channel cardiac array coil. Ten SA as well as three LA images captured from the heart of a 36 year-old male volunteer. Important parameters are as follows: TR = 3.1 ms, TM = 250 ms, number of averages = 3, number of phases = 3, in-plane resolution =  $1.5 \times 1.5 \text{ mm}^2$ . Slice thickness of SA images is 5mm while it is 6 mm for LA images. SA slices were spaced every 7.5 mm and the distance of LA slices is 24 mm. Experiment was performed under free respiration condition. To synchronize the RF pulses with the motion of the heart and chest, respiratory and heart monitoring were achieved using a pneumatic bellow and ECG. Position and direction of images were determined by header information of DICOM files and used to put the slices

together. The displacement field was smoothed by a moving average filtering. Using displacement of the particles in separated SA slices and LA slices, we tried to estimate the motion of the points in the volume surrounded by these planes through a multi-linear interpolation. This estimated displacement field was compared to the original displacement acquired by DENSE MRI for particles over the interleaved SA layers.

**Results:** Estimating the magnitude of the displacement field for a region on one of the SA layers by its adjacent SA and LA neighbors resulted in 29% relative root-mean-squared (rms) error. It is almost equal to the 24% relative rms difference of the same parameter calculated by SA and LA acquisitions for the points on the intersection of those layers.

This method also provided the displacement information for other points out of the images and therefore has the potential of resulting in more accurate calculation for the mechanical strain of the myocardium.

**Conclusion:** This method is able to give more accurate calculation for the mechanical strain of the myocardium by increasing the resolution of data points. This advantage is along with a 20% to 40% reduction of the scan time based on the number and position of the selected layers for imaging.